

POLITECNICO DI MILANO



SCUOLA DI INGEGNERIA DEI SISTEMI

DIPARTIMENTO DI BIOINGEGNERIA

LAUREA SPECIALISTICA
INGEGNERIA BIOMEDICA

A SMART STRETCHABLE MULTI-ELECTRODE ARRAY: A FEASIBILITY STUDY

Supervisor for Politecnico di Milano:
Prof. Sergio CERUTTI

Co-examiner for Philips Research Eindhoven
and Delft University of Technology:
Prof. Ronald DEKKER

Co-examiner for Politecnico di Torino:
Prof. Filippo MOLINARI

Thesis by:
Giuliano BUTTI
750514

ACADEMIC YEAR 2010/2011

TABLE OF CONTENTS

INDEX OF FIGURES	4
INDEX OF TABLES	11
SOMMARIO	12
ABSTRACT	19
1.INTRODUCTION.....	25
1.1 STRETCHABLE ELECTRONICS, A LITERATURE REVIEW	26
1.1.1 STRETCHABLE ELECTRODES.....	29
1.1.2 STIFF ISLANDS ONTO AN ELASTOMERIC SUBSTRATE	30
1.1.3 STRETCHABLE INTERCONNECTS.....	31
2.MATERIALS AND METHODS	36
2.1 STRENGTH OF MATERIALS	37
2.2 SUBSTRATE MATERIAL.....	38
2.3 POLYDIMETHYLSILOXANE.....	39
2.3.1 PREPARATION.....	40
2.3.2 MECHANICAL PROPERTIES	41
2.3.3 METAL THIN FILMS ON POLYMER SUBSTRATES	44
2.3.4 STERILIZATION AND EXPOSURE TO CULTURE MEDIA	47
2.4 SILICON OXIDE.....	48
2.4.1 THERMAL OXIDE.....	48
2.4.2 PECVD OXIDE	48
2.5 STIFF ISLANDS.....	49
2.5.1 SILICON NITRIDE	50
2.5.2 POLY-SILICON.....	51
2.6 MICROFABRICATION FUNDAMENTALS.....	52
2.6.1 PHOTOLITHOGRAPHY	52
2.6.2 MASK DESIGN	52
2.6.3 SPIN-COATING.....	53
2.6.4 SOFT BAKING.....	54
2.6.5 EXPOSURE	54
2.6.6 DEVELOPING	55

2.6.7	POSTBAKING	55
2.6.8	RESIST STRIPPING.....	55
2.6.9	ETCHING.....	56
2.6.10	WET CHEMICAL ETCHING	57
2.6.11	REACTIVE ION ETCHING	57
2.6.12	DEEP REACTIVE ION ETCHING	59
3.	COMPLEMENTARY EXPERIMENTS	61
3.1	MASK DESIGN.....	62
3.2	FEM MECHANICAL SIMULATION.....	64
3.2.1	MEMBRANE INFLATION.....	64
3.2.2	EFFECTS OF ISLAND'S SHAPE AND DIMENSIONS.....	70
3.2.3	ANTI-DELAMINATION SHIELD	71
3.3	BULGE TEST	74
3.3.1	BULGE TEST DEVICE	78
4.	FABRICATION PROCESS	81
4.1	THERMAL OXIDE AS ETCH STOP LAYER	82
4.1.1	20 μ m PDMS LAYER.....	86
4.1.2	80 μ m PDMS LAYER.....	93
4.2	ZERO-STRESS PECVD OXIDE AS ETCH STOP LAYER	95
5.	RESULTS.....	101
5.1	EFFECTS OF PDMS THICKNESS	102
5.2	EFFECTS OF ISLANDS' SHAPE	105
5.2.2	EFFECTS OF ANTI-DELAMINATION STRUCTURES.....	108
6.	APPLICATIONS OF STRETCHABLE ELECTRONICS	110
6.1	STRETCHABLE MEA FOR CARDIO-TOXICITY DRUG SCREENING APPLICATIONS.....	111
6.1.1	PATTERNING CELLS ON THE MEMBRANE.....	120
6.1.2	ADVANTAGES OF STRETCHABILITY	122
6.2	IMPLANTABLE DEVICES	125
7.	CONCLUSIONS	130
	REFERENCES	134
APPENDIX A – DETAILED FABRICATION SEQUENCE		

INDEX OF FIGURES

FIGURE 1.1 - EXAMPLES OF STRETCHABLE ELECTRONICS. A) STRETCHABLE SILICON CIRCUIT IN A WAVY GEOMETRY, COMPRESSED IN ITS CENTER BY A GLASS CAPILLARY TUBE (MAIN) AND WAVY LOGIC GATE BUILT WITH TWO TRANSISTORS (TOP RIGHT INSET). B) STRETCHABLE SILICON CIRCUIT WITH A MESH DESIGN, WRAPPED ONTO A MODEL OF A FINGERTIP, SHOWN AT LOW (LEFT), MODERATE (CENTER) AND HIGH (RIGHT) MAGNIFICATION. THE RED (LEFT) AND BLUE (CENTER) BOXES INDICATE THE REGIONS OF MAGNIFIED VIEWS IN THE CENTER AND RIGHT, RESPECTIVELY. THE IMAGE ON THE RIGHT WAS COLLECTED WITH AN AUTOMATED CAMERA SYSTEM THAT COMBINES IMAGES AT DIFFERENT FOCAL DEPTHS TO ACHIEVE A LARGE DEPTH OF FIELD [2]	26
FIGURE 1.2 - CONCEPTS FOR STRETCHABLE ELECTRONIC MATERIALS. A) STRETCHABLE SILICON MEMBRANE (~100 NM THICKNESS) CONFIGURED IN A WAVY SHAPE AND BONDED TO A PIECE OF RUBBER, PRESENTED IN OPTICAL (TOP) AND ATOMIC FORCE (BOTTOM) MICROSCOPE IMAGES. B) EXTREMELY STRETCHABLE SILICON MEMBRANE (~100-NM THICKNESS) PATTERNED INTO A MESH GEOMETRY AND BONDED TO A RUBBER SUBSTRATE ONLY AT SQUARE PADS LOCATED BETWEEN ARC-SHAPED BRIDGE STRUCTURES, PRESENTED IN MODERATE (TOP) AND HIGH (BOTTOM) MAGNIFICATION SCANNING ELECTRON MICROSCOPE (SEM) IMAGES. THE PDMS IS COLORIZED BLUE [2]	27
FIGURE 1.3 - SCHEMATIC ILLUSTRATION OF THE PROCESS FOR BUILDING STRETCHABLE SINGLE-CRYSTAL SI DEVICES ON ELASTOMERIC SUBSTRATES [7].....	28
FIGURE 1.4 - SCANNING ELECTRON MICROGRAPHS OF A 100 NM THICK Au LAYER ON A PDMS SUBSTRATE. MICROSCOPIC CRACKS THAT FORM IN THE FILM CAN TAKE PLACE DURING FABRICATION [9].....	29
FIGURE 1.5 - TOP: SCHEMATIC CROSS-SECTION ILLUSTRATING A COMPLIANT ELECTRODE OBTAINED BY ION IMPLANTATION. THE CLUSTERS ARE TOUCHING EACH OTHER BUT CAN SLIDE RELATIVE TO EACH OTHER. THEY CAN SUSTAIN LARGE STRAIN WHILE REMAINING CONDUCTIVE. BOTTOM: NON-COMPLIANT ELECTRODE OBTAINED BY THIN-FILM DEPOSITION. THE STRONG BINDING FORCES WHICH LINK THE METALLIC ATOMS TOGETHER DRASTICALLY LIMIT THE ACHIEVABLE STRAIN BEFORE DAMAGE TO THE ELECTRODE [11]	30
FIGURE 1.6 - A COMPLIANT, ELASTOMERIC SUBSTRATE CARRIES STIFF SUBCIRCUIT ISLANDS INTERCONNECTED WITH STRETCHABLE METALLIZATION. UPON DEFORMATION, THE SUBSTRATE ALONG WITH THE STRETCHABLE INTERCONNECTS ACCOMMODATES THE RESULTING TENSILE, COMPRESSIVE, AND SHEAR STRAINS WHILE THE ISLANDS REMAIN INTACT [3].....	30
FIGURE 1.7 - ARCHITECTURE OF AN ELASTIC ELECTRONIC SURFACE MADE ON A POLYMER SUBSTRATE. ACTIVE DEVICE CELLS CAN BE FABRICATED ON RIGID SUBCIRCUIT ISLANDS DISTRIBUTED OVER THE POLYMER SURFACE. THE CELLS ARE INTERCONNECTED WITH STRETCHABLE METALLIZATION [12].....	31
FIGURE 1.8 - STRESS DISTRIBUTION IN COPPER CONDUCTOR LINE FOR THREE DIFFERENT CONDUCTOR SHAPES [14].....	32
FIGURE 1.9 - POISSON EFFECT OBSERVED DURING A UNIAXIAL TENSION TEST [15].....	33

FIGURE 1.10 - TENSILE STRAIN TEST OF HORSESHOE METAL INTERCONNECTS. A) BEFORE ELONGATION. B) AFTER 25% ELONGATION HIGHLIGHTING THE FAILURES IN THE CREST AND TROUGH	33
FIGURE 1.11 - SEM MICROGRAPH OF THE AS-PREPARED 25 NM THICK GOLD FILM ON PDMS. THE GOLD LIGAMENTS PERCOLATE BETWEEN THE MICRON-SIZE MICRO-CRACKS [10].....	35
FIGURE 2.1 – A) A MATERIAL BAR WITH LENGTH L_0 AND CROSS SECTION AREA A_0 . B) IF A LOAD F IS APPLIED TO BOTH ENDS OF THE BAR, IT IS STRETCHED TO A NEW LENGTH L AND ITS CROSS SECTION AREA SHRINKS TO A [18]	37
FIGURE 2.2 – A SCHEMATIC ILLUSTRATION OF THE STRESS-STRAIN CURVE OF A METAL AND A POLYMER [18].	38
FIGURE 2.3 : A) CHEMICAL STRUCTURE OF SILICONE MONOMER; B) SPACE FILLING MODE OF A PDMS CHAIN [19].....	39
FIGURE 2.4 - GRAPH OF THE YOUNG'S MODULUS WITH RESPECT TO CURING TEMPERATURE FOR PDMS WITH A 10:1 AND 11:1 WEIGHT RATIO OF PREPOLYMER TO HARDENER [34].....	41
FIGURE 2.5 - GRAPH OF THE YOUNG'S MODULUS A) WITH RESPECT TO THE WEIGHT RATIO OF PDMS PREPOLYMER TO HARDENER FOR SAMPLES CURED AT 85°C FOR 100 MINUTES B) WITH RESPECT TO TIME AGED AT 100°C IN AN AIR OVEN FOR PDMS WITH A 10:1 AND 11:1 WEIGHT RATIO OF PREPOLYMER TO HARDENER [34]	42
FIGURE 2.6 - ELASTIC MODULUS OF SYLGARD 184 A) AGAINST TEMPERATURE B) AS A FUNCTION OF THE STRAIN RATE [35].....	42
FIGURE 2.7 - YOUNG'S MODULUS VERSUS THE INVERSE OF PDMS THICKNESS, $T^{-1/2}$ ($\text{MM}^{-1/2}$). THE TRANSITION POINT FROM SIZE DEPENDENT TO BULK BEHAVIOR IS PREDICTED TO BE AROUND 200 MM IN THICKNESS OF PDMS MEMBRANE [32]	43
FIGURE 2.8 - A) SKETCH OF THE PDMS MIXTURE DISPENSED ONTO A WAFER SUBSTRATE AND TANGLED POLYMER CHAIN COILS. B) WHEN SPINNING IS APPLIED THE PDMS IS THINNED AND POLYMER CHAIN COILS ARE STRETCHED BY SHEAR STRESS WHICH IS A GRADIENT ALONG THE THICKNESS (z) DIRECTION. C) WHEN A GREATER SPIN SPEED IS APPLIED THE POLYMER CHAINS ARE EXTENSIVELY REORDERED IN THE RADIAL DIRECTION AND THE PDMS MEMBRANE IS THINNED FURTHER. D) THE PDMS MEMBRANE WITH A DESIRED THICKNESS AND REORDERED (ALIGNMENT) IS SEPARATED FROM THE WAFER SUBSTRATE [32]	43
FIGURE 2.9 - THE RAPTURE OF A METAL FILM CAUSED BY STRAIN LOCALIZATION. A NECKING OF A FREE STANDING METAL FILM, B LOCAL ELONGATION IS SUPPRESSED BY THE SUBSTRATE [40]	44
FIGURE 2.10 - FOCUSED ION BEAM (FIB) IMAGES OF (A) AS-DEPOSITED FILM AND, AND (B) FILM ANNEALED AT 200 °C FOR 30 MIN. ANNEALING HAS CAUSED SIGNIFICANT GRAIN GROWTH. WHEREAS GRAINS HAVE A RELATIVELY UNIFORM DISTRIBUTION IN THE ANNEALED FILM, ISOLATED LARGE GRAINS CAN BE IDENTIFIED IN THE AS-DEPOSITED FILM [39].....	45
FIGURE 2.11 - THE RESISTANCE CHANGE VERSUS ELONGATION NORMALIZED WITH THEIR INITIAL VALUES. THE CURVE $R/R_0=(L/L_0)^2$ SHOWS THE THEORETICAL PREDICTION OF RESISTANCE CHANGE ASSUMING THAT NO CRACKS HAPPEN IN THE FILM. THE RESISTANCE OF THE AS-DEPOSITED FILM STARTS TO DEVIATE SIGNIFICANTLY FROM THE THEORETICAL PREDICTION DUE TO EMERGING CRACKS AT ELONGATION OF APPROXIMATELY 12%, WHEREAS THE ANNEALED FILM IS MUCH MORE ROBUST [39]	46
FIGURE 2.12 - A SCHEMATIC ILLUSTRATION OF CONCURRENT FAILURE PROCESSES: DEFORMATION-ASSOCIATED GRAIN GROWTH, STRAIN LOCALIZATION PROMOTED BY LARGE GRAINS, AND FILM/SUBSTRATE INTERFACE	

DEBONDING. THE THREE PROCESSES COEVOLVE TO FORM A NECK. FIB IMAGES OF UNANNEALED FILM: B NOT STRETCHED, C 15% , AND D 20% OF STRETCH [39].....	46
FIGURE 2.13 - THE EFFECT OF PEAK THERMAL CYCLING TEMPERATURE ON THE ROOM TEMPERATURE STRESS OF SILANE-BASED PECVD OXIDE FILMS [43].....	49
FIGURE 2.14 - SCHEMATIC DIAGRAM FOR MEASURING DETACHMENT LENGTH AND ADHESION ENERGY OF PDMS MICROSTRUCTURES. THE SURFACE UNDER TESTING (S.O.T.) INCLUDE SINGLE CRYSTAL SILICON, THERMALLY GROWN OXIDE, LPCDV NITRIDE, GLASS AND PDMS [46].....	50
FIGURE 2.15 – DEPOSITION RATE AS A FUNCTION OF GAS-FLOW RATIO FOR A TEMPERATURE OF 850° C AND A PRESSURE FOR A GAS-FLOW RATIO NH ₃ /SiH ₂ CL ₂ OF 30/170 [44].....	50
FIGURE 2.16 -ETCH RATE OF SILICON NITRIDE IN A PARALLEL-PLATE PLASMA ETCHER AS A FUNCTION OF PROCESS GAS-flow RATIO FOR A DEPOSITION TEMPERATURE OF 850°C AND A PRESSURE OF 20 PA. THE PLASMA ETCHING WAS PERFORMED USING A GAS COMPOSITION OF CHF 3 7.5 SCCM AND N 2 42.5 SCCM, R.F. POWER (FREQUENCY 13.56 MHZ) AND GAS PRESSURE OF 60 W (52 MW/CM ³) AND 5 PA, RESPECTIVELY [44]	51
FIGURE 2.17 – A TYPICAL STRESS BIAxIAL-STRAIN PLOT [47].....	51
FIGURE 2.18 - ANGULAR VIEW OF ALIGNMENT MARKS ETCHED IN Si (SEM MICROGRAPH).....	53
FIGURE 2.19 -PERSISTS OF POSITIVE AND NEGATIVE PHOTORESISTS AFTER DEVELOPMENT	55
FIGURE 2.20-ETCH PROFILES (A) ISOTROPIC ETCH PROFILE (B) ABSOLUTE AN-ISOTROPIC ETCH PROFILE	56
FIGURE 2.21 - ETCH (BLACK) AND PASSIVATION (PINK) STEPS OF DRIE.....	59
FIGURE 2.22 - TYPICAL PROFILE OF DEEP REACTIVE ION ETCHING (SEM MICROGRAPH). EACH RIPPLE SHOWS ONE COMPLETE CYCLE (ETCHING AND PASSIVATION)	59
FIGURE 3.1 : THREE DIFFERENT ISLAND SHAPES HAVE BEEN TESTED, VARYING THEIR DIMENSIONS AND THE DISTANCE BETWEEN THEM	62
FIGURE 3.2 - SNAPSHOT FROM CADENCE. A) A VIEW OF SOME CHIPS. THE GREY LINE AROUND THEM FIX THE BORDERS OF EACH CHIP (1 CM X 1 CM) FOR THE BACKSIDE MASK, LIGHT GREEN SHAPE IN THE CENTER OF EACH CHIP REPRESENT THE HOLE AND DARK GREEN STRUCTURES INSIDE THE HOLE ARE THE ISLANDS OF THE FIRST TOPSIDE MASK. ALSO A CODE ALLOWS US TO DISTINGUISH THE CHIP DURING THE MICROSCOPE INSPECTION. THE FIRST PART INDICATES THE DIMENSION OF THE ISLAND (S FOR 50 μM, M FOR 100 μM, L FOR 200 μM AND XL FOR 300 μM ISLANDS). THE SECOND PART INDICATES THE SHAPE OF THE ISLAND (C FOR CIRCLE, Q FOR SQUARE AND CQ FOR ROUNDED SQUARE). THE LAST NUMBER INDICATES THE INTERISLAND SPACE (IN μM). B) A DETAILED VIEW OF SOME ISLANDS (BLUE) SURROUNDED BY THE ANTI-DELAMINATION SHIELD (RED).....	63
FIGURE 3.3 - THE ONE-ISLAND MEMBRANE THAT HAS BEEN INFLATED IN THE FIRST SIMULATION.....	65
FIGURE 3.4 - USER DEFINED MESH. A) THE OVERALL MESH IS PRESENTED IN THE 3D STRUCTURE. AS EXPLAINED BEFORE, WE DEFINED THE MESH ON THE TOP SURFACE AND SWEEPED IT THROUGH THE WHOLE THICKNESS OF THE MEMBRANE. B) TOP VIEW OF THE MESH. IN THE CORNERS OF THE ISLAND THE ELEMENTS BECOME SMALLER AND THE ACCURACY HIGHER. C) A DETAIL OF THE CORNER, THE ISLAND IS HIGHLIGHTED IN RED	66
FIGURE 3.5 - FIRST PRINCIPAL STRAIN IN THE MEMBRANE INFLATED FROM THE BACKSIDE WITH A 70 KPA PRESSURE. A) A THREE-DIMENSIONAL VIEW OF THE DEVICE. AS EXPECTED THE HIGHER STRAIN ARE IN THE	

REGION SURROUNDING THE STIFF ISLAND ALONG THE Y AXIS. B) THE FRONTAL VIEW OF THE MEMBRANE. WE CAN SEE THE SHAPE OF THE SUBSTRATE ONCE THE PRESSURE IS APPLIED. HIGHER STRAIN IS ALSO AT THE BOTTOM SIDES OF THE MEMBRANE, POSSIBLE CAUSE OF DELAMINATION OF THE SUBSTRATE FROM THE SURROUNDING.....	68
FIGURE 3.6 - A VIEW ON THE SECOND (A) AND THIRD (B) PRINCIPAL STRAIN. STRAIN IS A VECTOR THAT CAN BE COMPLETELY DESCRIBED WITH THREE ORTHOGONAL COMPONENTS. HOWEVER, AS WE CAN SEE IN THESE PICTURES, THE VALUES OF THESE TWO COMPONENTS ARE REALLY LOWER COMPARED TO THE FIRST ONE. IN A FIRST APPROXIMATION WE CAN CONSIDER JUST THE FIRST PRINCIPAL STRAIN SHOWED IN	69
FIGURE 3.7 - FIRST PRINCIPAL STAIN IN THE PROXIMITY OF THE ROUND ISLAND. PHYSICAL DEFORMATION IS INCLUDED IN THESE PLOTS [19].....	70
FIGURE 3.8 - FIRST PRINCIPAL STAIN IN THE PROXIMITY OF THE ROUND ISLAND FOR DIFFERENT ISLAND SHAPES (RFILLET) VARYING THE ISLAND SIZE L. PHYSICAL DEFORMATION IS INCLUDED IN THESE PLOTS [19]	71
FIGURE 3.9 - SCANNING ELECTRON MICROSCOPE (SEM) PICTURES OF THE INFLATED MEMBRANE. A) DELAMINATION AROUND ISLANDS IS DUE TO THE HIGH STRAIN IN THE ELASTOMERIC MEMBRANE THAT IS SURROUNDING THE STIFF MATERIAL B) A DETAIL OF THE SAME DELAMINATION. A SMALL VALLEY IN THE PDMS TAKES PLACE AT THE EDGES OF THE ISLAND	72
FIGURE 3.10 – TWO-DIMENSIONAL VIEWS OF THE MEMBRANE CROSS SECTION ONCE A 70 KPA PRESSURE IS APPLIED FROM THE BACKSIDE. SYMMETRY CONDITION IS IMPOSED ALONG THE VERTICAL AXIS, ALLOWING A MORE ACCURATE SIMULATION OF THE FIRST PRINCIPAL STRAIN. SECOND AND THIRD PRINCIPAL STRAINS ARE NOT REPORTED IN THIS STUDY, THEIR VALUES ARE EXTREMELY LOWER COMPARED TO THE FIRST PRINCIPAL ONE. THREE DIFFERENT CONFIGURATIONS HAVE BEEN ANALYZED, WITHOUT ANY INDENTATION (A), 4 μM INDENTATION (B) AND 8 μM INDENTATION (C). THE SHAPE OF THE MEMBRANE WHEN NO PRESSURE IS APPLIED IS SHOWED WITH A BLACK LINE BENEATH THE INFLATED MEMBRANE.	73
FIGURE 3.11 – A DETAIL OF THE INFLATED MEMBRANE SURROUNDING THE ISLAND. WITH AN 8 μM INDENTATION (B) THE MAXIMUM STRAIN IS REDUCED BY 54% COMPARED TO THE BASE CONDITION WITHOUT ANY INDENTATION (A).....	74
FIGURE 3.12 - BULGE TEST PRINCIPLE: A) A FREE-STANDING MEMBRANE (IN GREY) ON A RIGID SUBSTRATE (IN BROWN) WITH AN INITIAL LENGTH L. B) SIDE VIEW OF THE STACK, STIFF ISLANDS ARE REPRESENTED WITH BLUE RECTANGLES. C) AS PRESSURE IS APPLIED, THE PLANAR MEMBRANE TRANSFORM INTO A CYLINDRICAL CUP WITH HEIGHT h_0 AND THE ELASTOMERIC SUBSTRATE ELONGATES TO A NEW LENGTH L_1	75
FIGURE 3.13 - CROSS SECTION OF TWO DIFFERENT MEMBRANES WITH DIFFERENT ISLANDS SIZE, BEFORE AND AFTER STRETCHING. THE ELASTOMERIC MEMBRANE IS REPRESENTED IN DARK BLUE AND THE ISLANDS ARE DEPICTED IN LIGHT BLUE. NOTWITHSTANDING THE INITIAL AND THE FINAL LENGTH OF THE TWO MEMBRANES ARE THE SAME, THE HYPOTHESIS THAT STIFF ISLANDS DO NOT DEFORM REQUIRES, IN CASE OF BIG ISLANDS, A HIGHER PERCENTAGE STRAIN OF THE ELASTOMERIC SUBSTRATE.....	76
FIGURE 3.14- CYLINDRICAL MODELING OF THE MEMBRANE INFLATION. A CROSS-SECTIONAL VIEW	77
FIGURE 3.15 - THE BULGE TEST DEVICE MOUNTED ON A MICROSCOPE PLATE. TWO CABLES CONNECTED ON THE SIDES PROVIDE THE VACUUM CLAMPING AND THE INFLECTION RESPECTIVELY. THE WHITE BLOCKS ON THE TWO SIDES OF THE CHIP ALLOW A CORRECT POSITIONING OF THE CHIP ITSELF.....	79

FIGURE 3.16 - A CROSS SECTIONAL VIEW OF THE TESTING DEVICE. THE GREEN LAYER ON TOP OF SILICON SUBSTRATE (IN GREY) REPRESENTS THE INFLATED MEMBRANE.	79
FIGURE 3.17 - AN OVERALL VIEW OF THE EXPERIMENTAL SET USED TO APPLY PRESSURE ON THE CHIPS AND COLLECT INFORMATION OF THEIR BEHAVIOR UNDER STRESS.....	80
FIGURE 4.1- COMPLETE FABRICATION PROCESS SEQUENCE	83
FIGURE 4.2 - SPIN CURVE FOR HPR 504 RESIST [56].....	84
FIGURE 4.3- 50 μm CIRCLED SQUARED ISLANDS WITH 100 μm INTERISLAND SPACE	85
FIGURE 4.4- A DETAIL OF ONE 50 μm CIRCLED SQUARED ISLAND AFTER RESIST DEVELOPMENT	85
FIGURE 4.5- 10 μm GROOVES ON THE BACKSIDE DESIGNED TO FACILITATE THE SPLITTING OF THE CHIPS AT THE END OF THE FABRICATION PROCESS	86
FIGURE 4.6-ALUMINUM WRINKLES ON PDMS SEEN FROM INCREASING MAGNITUDES.....	87
FIGURE 4.7- WRINKLES ON ALUMINUM AND SILICON OXIDE LAYERS AFTER SILICON IS DRY ETCHED FROM THE BACKSIDE. ACCORDING TO THE DIRECTION OF THE STRESS IN THE MEMBRANE, THESE WRINKLES PROPAGATES HORIZONTALLY, VERTICALLY OR SINUSOIDALLY	88
FIGURE 4.8 - A SCHEMATIC OF THE MEMBRANE. IN THIS EXAMPLE STRESS IS SUPPOSED TO BE RELEASED HORIZONTALLY. THEREFORE ALUMINUM FORMS ITS WRINKLES VERTICALLY ON THE TOP OF THE MEMBRANE.....	89
FIGURE 4.9- CRACKS ON THE MEMBRANE. THESE CRACKS ARE OFTEN PERPENDICULAR TO THE WRINKLES OF THE MEMBRANE. AS EXPLAINED BEFORE IN THIS CASE THE MEMBRANE WAS ABLE TO RELEASE ITS COMPRESSIVE STRESS JUST IN ONE DIRECTION, CAUSING BENDING OF THE MEMBRANE (DESCRIBED BY WRINKLES ON THE TWO EXTREMITY SURFACES) AND CRACKS IN THE OTHER DIRECTION.....	90
FIGURE 4.10- MOLECULAR STRUCTURE OF TRITON X-100 [57].....	90
FIGURE 4.11 - ELASTOMERIC SUBSTRATE AFTER BOE ETCHING PREVIOUSLY TREATED WITH TRITON X-100. WRINKLES ARE ALL OVER THE SURFACE [100X MAGNIFICATION].....	91
FIGURE 4.12- MEMBRANE INSPECTION AFTER REMOVAL OF SILICON OXIDE. NO MORE WRINKLES ARE PRESENT; THE OXIDE LAYER HAS BEEN COMPLETELY REMOVED.....	91
FIGURE 4.13 - AFTER BOE ETCHING THE SILICON OXIDE HAS BEEN COMPLETELY REMOVED FROM THE CENTER OF THE HOLE BUT NOT AROUND THE EDGES. DIFFERENT COLORS OF THE ISLANDS REFER TO DIFFERENT THICKNESS OF THE OXIDE LAYER STILL PRESENT ABOVE.....	92
FIGURE 4.14 - INSPECTION OF THE MEMBRANE AFTER SILICON PLASMA EXPOSURE AND BOE ETCHING. NO MORE WRINKLES AFFECT THE MEMBRANE; THE ENTIRE SILICON OXIDE LAYER HAS BEEN REMOVED	92
FIGURE 4.15 - DIRTY SPOTS IN THE CORNER OF THE EDGES. IN ORDER TO INSPECT THE ROLE OF THE SURFACTANT IN THE FORMATION OF THESE SPOTS WE REPEATED THE EXPERIMENT USING WATER IN PLACE OF IT.....	93
FIGURE 4.16 – A) NO MORE WRINKLES AFFECT THE MEMBRANE B) NO DIRTY SPOTS ARE NOW IN PROXIMITY OF THE CORNERS, SHOWING THAT THEIR FORMATION IN THE PREVIOUS EXPERIMENT WAS MOSTLY DUE TO THE REACTIONS THAT TAKE PLACE WITH THE SURFACTANT	93
FIGURE 4.17 - SPIN CURVE OF RTV615 AND SYLGARD 184, MEAN ACROSS THE WHOLE WAFER AREA [31]....	94
FIGURE 4.18 – COMPARISON BETWEEN ALUMINUM WRINKLES ABOVE 80 μm (A) AND 20 μm (B) PDMS LAYER	94

FIGURE 4.19 - AN OVERALL VIEW OF THE 80 μM THICK PDMS MEMBRANE AFTER ALUMINUM AND OXIDE REMOVAL. IN THIS CASE NOR WRINKLES NEITHER CRACKS TOOK PLACE ON THE MEMBRANE	95
FIGURE 4.20 - COMPLETE FABRICATION PROCESS SEQUENCE FOR NITRIDE ISLANDS. VARIATIONS FOR POLY-SILICON WILL BE DESCRIBED IN THE CHAPTER	96
FIGURE 4.21 - CIRCLE ISLANDS SURROUNDED BY A THIN LAYER OF RESIST. AT THE END OF THE FABRICATION PROCESS, ONCE THIS RESIST WILL BE REMOVED, THE INDENTATION WILL REMAIN IN THE MEMBRANE, REDUCING THE STRAIN IN THE PDMS AROUND THE ISLANDS AS SHOWED IN THE FEM PARAGRAPH	98
FIGURE 4.22 - ELASTOMERIC SUBSTRATES AFTER SILICON REMOVAL. A) AN OVERALL IMAGE OF THE MEMBRANE SHOWS NEITHER WRINKLES NOR CRACKS TOOK PLACE IN OXIDE, PDMS AND ALUMINUM LAYERS. PICTURES B) AND C) SHOW DETAILS ABOUT ISLANDS AND THE ANTI-DELAMINATION SHIELD SURROUNDING THEM.....	99
FIGURE 4.23 - SEM PICTURES OF THE ANTI-DELAMINATION SHIELD SURROUNDING THE ISLANDS. A) AN OVERALL VIEW OF THE ISLANDS SURROUNDED BY THESE CHANNELS. B) A DETAIL OF ONE CORNER; THE ISLAND IS SURROUNDED BY A SMALL PDMS LAYER (5 μM LENGTH) BEFORE THE INDENTATION. THE SIZE OF THE INDENTATION IS 10 μM AND ITS DEPTH IS 7.87 μM (THE SAME THICKNESS OF THE RESIST SPIN COATED IN THE INDENTATIONS AND THEN REMOVED WITH ACETONE).....	100
FIGURE 5.1 : LOCATIONS OF EDGE BEAD FORMED DURING THE SPIN-COATING OF PDMS ON TOP OF THE WAFER	102
FIGURE 5.2 – STRAIN-TREND IN PDMS FOR TWO DIFFERENT MEMBRANE THICKNESSES WHEN THE SAME PRESSURE IS APPLIED TO THE SAME ISLANDS CONFIGURATION. VERTICAL BARS INDICATE THE STANDARD DEVIATION OUT OF 15 MEASURES	103
FIGURE 5.3 - SEM PICTURES OF PDMS SCRATCHING IN THE REGIONS BETWEEN THE ISLANDS.....	104
FIGURE 5.4 - TRUE STRESS VERSUS TRUE STRAIN OF PDMS MEMBRANE WITH DIFFERENT THICKNESSES [32]	105
FIGURE 5.5 - DISTRIBUTION OF THE FIRST PRINCIPAL STRAIN IN THE PDMS MEMBRANE SURROUNDING THE ISLAND ACCORDING TO THE ISLAND SHAPE [19]	106
FIGURE 5.6 - 300 μM NITRIDE CIRCLE ISLAND INFLATED BY 65 KPA (A) AND 80 KPA (B). HUGE DELAMINATION FROM THE SURROUNDING MEMBRANE TOOK PLACE	107
FIGURE 5.7 - 300 μM NITRIDE SQUARE ISLAND INFLATED BY 65KPA (A) AND 80 KPA (B). DELAMINATION IS QUITE CONFINED.....	107
FIGURE 5.8 - CIRCLE ISLAND (300 μM) WITH (B) AND WITHOUT (A) ANTI-DELAMINATION STRUCTURE. SAME PRESSURE IS APPLIED (80 KPA). THE ANTI-DELAMINATION SHIELD PROVED TO REDUCE SIGNIFICANTLY THIS PHENOMENON	108
FIGURE 6.1 - ELECTROPHYSIOLOGICAL DIFFERENCES BETWEEN ADULT HUMAN AND MOUSE CMs. HUMAN AND MOUSE HEARTS DISPLAY UNIQUE ECG PROFILES, WITH THE QT INTERVAL IN HUMANS APPROXIMATELY FIVE TIMES LONGER THAN IN MICE. THIS IS ALSO REFLECTED IN THE DIFFERENT AP DURATIONS AND SHAPES OF THE VENTRICULAR Cms FROM THESE TWO SPECIES AND IS DUE TO THEIR INSTINCTIVE IONIC CURRENTS. ALTHOUGH THE INWARD Na^+ AND Ca^{2+} CURRENTS (I_{Na} AND I_{CaL} , RESPECTIVELY) ARE COMPARABLE BETWEEN MOUSE AND HUMAN Cms, MAJOR DIFFERENCES ARE OBSERVED IN THE VARIOUS OUTWARD K^+ CURRENTS (IN BLUE), WHICH PLAY DISTINCT ROLES IN HUMAN AND MOUSE AP	

REPOLARIZATION. THE I_{K_S} AND I_{K_R} ARE THE MAJOR REPOLARIZING CURRENTS IN HUMAN CMS, WHEREAS IN MICE I_{TO} IS THE PREDOMINANT CURRENT. ADDITIONALLY $I_{K_{SLOW1}}$, $I_{K_{SLOW2}}$ AND I_{SS} CONTRIBUTE TO REPOLARIZATION IN MOUSE CMS, BUT ARE ABSENT FROM HUMAN VENTRICULAR CMS. THE APs AND THEIR UNDERLYING IONIC CURRENTS ARE ALIGNED WITH THEIR APPROXIMATE TIME OF ACTION DURING THE QT INTERVAL SHOWN IN THE ECG EXAMPLES. (MS, MILLISECOND) [61]	112
FIGURE 6.2 - QT-INTERVAL PROLONGATION SHOWN ON THE CARDIAC ACTION POTENTIAL [64].....	113
FIGURE 6.3 – TYPICAL PAUSE DEPENDENT TORSADE DE POINTES (TDP). THE TACHYARRHYTHMIA IS PRECEDED BY VENTRICULAR BIGEMINY, CREATING A SERIES OF “LONG” AND “SHORT” CYCLES (MARKED L AND S). THE LONG QT INTERVAL IS DIFFICULT TO APPRECIATE BECAUSE THE EXTRA-SYSTOLES CONCEAL THE TERMINAL PART OF THE QT SEGMENT. [65]	114
FIGURE 6.4 - FIELD POTENTIAL RECORDINGS FROM A CARDIOMYOCYTE CLUSTER WITHIN AN EMBRYOID BODY PLATED ONTO A MEA. A) ELONGATED BEATING CELL CLUSTER AT DAY 6 AFTER PLATING THE EB. DIRECTION OF CONTRACTION SPREAD (MICROSCOPIC OBSERVATION) IS SHOWN BY ARROWS; RECORDING ELECTRODES ARE MARKED AS CIRCLES. B) SYNCHRONOUS RECORDINGS FROM ELECTRODES LABELED IN A. THE SEQUENTIAL INCREASE OF DELAY BETWEEN SPIKES REGISTERED AT ELECTRODES 45, 56, AND 87 VERSUS ELECTRODE 34 CONFIRMS THE DIRECTION OF THE EXCITATION WAVE INDICATED BY ARROWS IN A. DATA RETRIEVED FROM THE RESEARCH OF [68]	117
FIGURE 6.5 - FRESHLY PLACED EMBRYOID BODIES ON A 60 ELECTRODES MEA [68]	118
FIGURE 6.6 - A CONFIGURATION FOR THE OVERALL SET-UP FOR DRUG SCREENING PROPOSED BY [1].....	120
FIGURE 6.7 - MICRO-CONTACT PRINTING FOR CELL ALIGNMENT PROCEDURE [76].....	121
FIGURE 6.8 - CARDIAC MYOCYTES CULTURED ON TEXTURED MICROCHANNELS AND UNTEXTURED SILICONE [71]	122
FIGURE 6.9 -FLUORESCENCE IMAGE OF hESC-DERIVED CARDIOMYOCYTES GROWN ON PDMS SUBSTRATE. COURTESY OF LEIDEN UNIVERSITY MEDICAL CENTRE.....	124
FIGURE 6.10 - FLUORESCENCE IMAGE OF hESC-DERIVED CARDIOMYOCYTES GROWN ON PETRI-DISH (GLASS SUBSTRATE). COURTESY OF LEIDEN UNIVERSITY MEDICAL CENTRE	124
FIGURE 6.11 - COMPONENTS OF A COCHLEAR IMPLANT SYSTEM. COURTESY OF MED-EL MEDICAL ELECTRONICS GMBH, INNSBRUCK, AUSTRIA [78].....	126
FIGURE 6.12 - PLACEMENTS AND COMPONENTS OF ENVISIONED NEXT-GENERATION INTRAOCULAR RETINAL PROSTHESIS [80].....	127
FIGURE 6.13 - PARYLENE MEAs TACKED TO THE RIGHT CANINE RETINA SHOWING NORMAL VESSEL PERFUSION UNDER THE ARRAYS. ARROWS POINT TO THE RETINAL TACK [80]	127
FIGURE 6.14 - HEAT MOLDED AND ANNEALED RETINAL ELECTRODE ARRAY WITH RETAINED SPHERICAL CURVATURE (ARROW DENOTES RETINAL TACK HOLE) [80]	128
FIGURE 6.15 - SIMPLIFIED SCHEMATIC OF SUBCORTICAL MOTOR SYSTEM CIRCUITRY. BLUE ARROWS REPRESENT EXCITATORY SYNAPSES, AND OPEN RED CIRCLES REPRESENT INHIBITORY SYNAPSES. DOTTED LINE ACROSS THE THALAMUS INDICATES THE SEGREGATION BETWEEN STRIATAL AND CEREBELLAR CONNECTIONS. CBL CTX, CEREBELLAR CORTEX; CBL NUC, CEREBELLAR NUCLEI; GPE, GLOBUS PALLIDUS EXTERNAL SEGMENT; GPI, GLOBUS PALLIDUS INTERNAL SEGMENT; PN, PONTINE NUCLEI; SNL, SUBSTANTIA NIGRA PARERETICULATE; STN, SUBTHALAMIC NUCLEUS; STR, STRIATUM; THAL, THALAMUS [81].....	129

INDEX OF TABLES

TABLE 1.1 - PROPERTIES OF THE MATERIALS INVOLVED IN THE STUDY FROM [16].....	34
TABLE 2.1 - SCORING CARD FOR THREE CANDIDATE SUBSTRATE MATERIALS.....	38
TABLE 2.2 -SCORING CARD FOR TWO CANDIDATE ISLAND MATERIALS.....	49
TABLE 3.1 - MECHANICAL PROPERTIES OF THE ELEMENT INVOLVED IN THE SIMULATIONS. THE SUBSTRATE IS MADE BY PDMS AND THE ISLAND IS MADE BY SILICON NITRIDE	65
TABLE 5.1 - RESULTS OF THE INFLATION TESTS TO COMPARE THE INFLATION HIGH AND THE STRAIN OCCURRED IN PDMS FOR THE SAME ISLAND CONFIGURATION, WITH TWO DIFFERENT MEMBRANE THICKNESSES. WHEN THE INFLATION HIGH IS HIGHER THAN THE MEMBRANE RADIUS (600 MM), THE STRAIN IN PDMS CANNOT BE APPROXIMATED ANYMORE WITH THE FORMULA FROM [11].....	103
TABLE 6.1 : LIST OF DRUGS ADMINISTRATED TO CARDIOMYOCYTES CULTURES AVAILABLE IN LITERATURE. RESULTS ACHIEVED FROM DIFFERENT RESEARCH GROUPS ARE DESCRIBED	119

SOMMARIO

Il progetto affronta la realizzazione di una matrice estensibile di elettrodi (MEA) attraverso uno studio di fattibilità. I tradizionali componenti dell'elettronica sono rigidi, senza possibilità di estendersi e piegarsi, a meno di compromettere le loro funzionalità. Nel momento in cui occorre interagire con il corpo umano, attraverso dispositivi impiantabili, così come con cellule, per la realizzazione di tessuti biologici, diventa evidente il bisogno di una tecnologia in grado di integrare i tradizionali componenti fondamentali dell'elettronica, come transistor, amplificatori ed elettrodi, con strutture biocompatibili, oltre che in grado di piegarsi ed estendersi. Il fine di questo progetto è quello di integrare elementi rigidi e sottili, denominati isole rigide, all'interno di substrato elastomerico. Quest'obiettivo viene realizzato attraverso due passaggi fondamentali: il primo riguarda la definizione di un processo di fabbricazione in grado di produrre il dispositivo desiderato; il secondo è rappresentato dall'insieme di prove sperimentali, con lo scopo di descrivere il comportamento sotto sforzo dei dispositivi realizzati, valutandone diverse configurazioni.

Le isole rigide hanno il compito di rappresentare i futuri componenti elettronici, che al loro posto possono venire posizionati nel momento in cui un dispositivo funzionante voglia essere realizzato. Avendo queste isole proprietà meccaniche e dimensioni tipiche dei tradizionali componenti elettronici, il loro comportamento sotto sforzo è in grado di fornire preziose indicazioni: se queste isole resistono ai carichi applicati senza né rompersi né abbandonare il substrato, questo diventa una preziosa indicazione che, sottoposti alle stesse sollecitazioni, anche futuri componenti elettronici possano continuare a svolgere la propria funzione senza comprometersi. Le isole sono disposte lungo il substrato in modo da formare una matrice ordinata di componenti; le diverse configurazioni testate sono state ottenute variando dimensione, forma e distanza fra le isole. Due sono i materiali testati per la produzione di questo componente: il nitruro di silicio e il silicio policristallino (polisilicio). I motivi relativi alla scelta di questi materiali sono essenzialmente due: sono entrambi materiali tradizionalmente impiegati nelle tecnologie MEMS, ampiamente disponibili in ambiente *clean room*, oltre a condividere proprietà meccaniche decisamente simili ai tradizionali componenti elettronici. In un dispositivo *intelligente*, molteplici componenti possono essere inseriti all'interno di una stessa isola, ad esempio integrando elettrodi per la registrazione del segnale, amplificatori e filtri analogici, seguiti da un convertitore analogico digitale. Il risultato di

questo tipo di approccio è una drastica riduzione del numero di connessioni necessarie. Essendo queste connessioni uno degli aspetti più delicati della struttura, la loro riduzione va nella direzione di una maggiore robustezza del dispositivo stesso. L'estensibilità di questo dispositivo viene garantita dal materiale nel quale le isole vengono integrate; al posto del tradizionale substrato di silicio, intrinsecamente rigido, si è ricorsi al silicone (polidimetilsilossano o PDMS). Materiale dalla provata biocompatibilità, il PDMS ha proprietà meccaniche che gli consentono di estendersi e piegarsi, riuscendo ad adattare elasticamente un'ampia gamma di sforzi applicati. Non è questo l'unico materiale candidato alla realizzazione del substrato, anche parylene e poliammide, infatti, rappresentano valide alternative. Diversamente da questi due materiali, il PDMS costituisce una tecnologia relativamente nuova nell'ambito della micro fabbricazione, avendo alle spalle un volume letterario decisamente inferiore. Ciononostante, grazie alle sue proprietà meccaniche, come verrà illustrato nei prossimi capitoli, questo materiale ha contribuito in maniera significativa ai progressi di tale disciplina, permettendo il passaggio dall'elettronica flessibile, dove i dispositivi erano esclusivamente in grado di piegarsi, all'elettronica estensibile, aumentando drasticamente il numero di soluzioni implementabili. Le isole rigide rappresentano quindi una soluzione semplice ed economica per testare se dei componenti rigidi siano o meno in grado di rimanere integrati nel substrato estensibile sotto sforzo, senza né rompersi né rimuoversi. Se ciò si verifica, i componenti elettronici veri e propri possono finalmente essere realizzati, consentendo al dispositivo di svolgere la propria funzione.

Due diversi approcci offrono la possibilità di integrare isole rigide in un substrato elastomerico. Il primo è quello di lavorarle direttamente sul substrato stesso, evitando però di raggiungere alte temperature, sopra i 150°C circa, tipicamente non tollerate dai polimeri. Ricorrendo la quasi totalità dei processi tradizionali di micro fabbricazione a temperature nettamente superiori a tale soglia, lo sviluppo di nuovi approcci a bassa temperatura si è reso necessario. Il limite di questi approcci è quello di fornire una mobilità elettronica inferiore ai processi tradizionali, compromettendo le proprietà del dispositivo. Il progetto qui presentato si concentra pertanto su di un secondo approccio, dove tutte le tradizionali pratiche della *clean room* vengono esercitate prima di introdurre il polimero, passaggio che avviene al termine del processo di fabbricazione. Il processo sfruttato è una rielaborazione di quello impiegato da [1] al fine di integrare collegamenti metallici nel silicone; il processo è stato debitamente rimodellato e aggiornato al fine di integrare le isole rigide nell'elastomero. E' possibile vedere il processo di fabbricazione come un sistema che riceve in ingresso wafer rigidi in silicio e

fornisce in uscita isole rigide integrate in uno strato di silicone. A seguito dei risultati ottenuti dalla prima sequenza di fabbricazione, il processo è stato aggiornato sostituendo l'ossido termico con l'ossido PECVD come materiale di interruzione dell'etching, ovvero lo strato interposto fra silicio ed isole rigide, tale da proteggere queste ultime durante il processo di rimozione del silicio. L'ossido termico è infatti caratterizzato da un elevato sforzo compressivo; la possibilità di liberarlo gli è però preclusa fino a quando è in contatto con il silicio. Nell'istante in cui il silicio viene rimosso, l'ossido termico rilascia il suo sforzo, generando pieghe e rotture in grado di estendersi fino alle isole rigide, compromettendole. Questo problema è stato risolto sostituendo l'ossido termico con l'ossido PECVD che, grazie al particolare processo di produzione, ha uno sforzo compressivo insito praticamente nullo. I risultati raccolti hanno confermato questa intuizione: sostituendo l'ossido, infatti, i fenomeni di piegamento e rottura nella membrana sono praticamente scomparsi.

Alla fabbricazione del dispositivo segue la fase di prove meccaniche; per questo tipo di apparecchi sono essenzialmente due le strade percorribili. La prima è quella delle prove di trazione, dove il campione a geometria nota è caricato, ad entrambe le estremità, da una forza crescente, misurando le variazioni di lunghezza. In questo progetto, le ridotte dimensioni e spessore della membrana non hanno consentito di sfilare il substrato dalla regione circostante e si è pertanto optato per un test di rigonfiamento. Una pressione viene applicata alla base del substrato, vincolato lateralmente, misurando l'altezza raggiunta dal rigonfiamento della superficie anteriore. Posizionando il dispositivo al di sotto di un microscopio è possibile osservare il comportamento della membrana e delle isole sotto sforzo e misurare l'altezza raggiunta dal rigonfiamento, in funzione della pressione applicata. La strumentazione progettata agisce ancorando i bordi del dispositivo attraverso una depressione, mentre la membrana non vincolata, posta al centro, si rigonfia a causa della pressione positiva, regolabile manualmente. Tramite apposite equazioni è possibile dedurre la deformazione della membrana in funzione dell'altezza raggiunta dal rigonfiamento; l'equazione va a considerare la membrana rigonfiata come un arco di circonferenza, ed è pertanto applicabile fino a quando l'altezza del rigonfiamento non supera il raggio della membrana, ovvero la metà della sua larghezza. Al di sopra di questo valore di deformazione, la membrana assume una forma ovale, e le equazioni in nostro possesso non consentono più di associare all'altezza misurata un valore di deformazione della membrana. L'equazione richiede opportuni accorgimenti a seconda che vi siano o meno isole rigide nella sezione interessata. Il modulo di Young delle isole è di 5 ordini di grandezza superiore a quello

del substrato, sotto sforzo la deformazione delle isole è praticamente nulla, il substrato va ad accomodare quasi interamente la deformazione. L'equazione è stata così aggiornata con un termine che tiene conto della quantità di materiale rigido lungo la sezione, così da calcolare la deformazione del PDMS in funzione della pressione applicata. I principali risultati si riferiscono allo spessore della membrana ed alla forma delle isole.

Lo spessore della membrana viene regolato durante la deposizione del PDMS sulla superficie dei wafer, regolando la velocità di rotazione di questi ultimi per tutta la durata del processo. Substrati più spessi richiedono pressioni più elevate per poter raggiungere gli stessi livelli di deformazione di substrati più sottili. Se la membrana è pensata per dover resistere ad alte pressioni alle quali verrà esposta, la scelta dovrà ricadere su membrane spesse (sopra gli 80 μm). La deformazione nella membrana sarà infatti più contenuta, proteggendo l'elastomero da lacerazioni. D'altra parte, quando la membrana deve per sua natura deformarsi costantemente, permettendo al dispositivo di svolgere la sua funzione, strati più sottili sono consigliabili. Richiederanno infatti pressioni inferiori, riducendo anche il consumo dell'apparecchiatura.

Lo studio della forma delle isole rigide ha mostrato risultati interessanti. Tre sono le forme testate: circolari, quadrate e quadrate dai bordi arrotondati. Il vantaggio delle isole quadrate è quello di offrire una superficie maggiore a parità di dimensioni, consentendo di accomodare un maggior numero di componenti elettronici. D'altra parte le isole circolari mostrano picchi di deformazione più bassi sotto sforzo; in un bilanciamento tra questi due parametri, le isole quadrate dai bordi smussati sembrano offrire un buon compromesso. Dall'esecuzione dei test sperimentali è emerso che, ancor più del picco di deformazione, è la distribuzione della deformazione stessa nell'intorno delle isole a giocare un ruolo fondamentale nel comportamento del dispositivo. Nelle isole quadrate la deformazione è confinata in regioni poste in prossimità degli spigoli dell'isola, mentre, per le altre due forme considerate, la deformazione si distribuisce su di una regione molto più ampia, in grado di abbracciare l'intero lato dell'isola, causandone la delaminazione dal substrato circostante. Quello della delaminazione è un problema da contrastare in tutti i modi: l'isola rischia infatti di staccarsi, compromettendo il funzionamento del dispositivo, mentre le interconnessioni, sovraesposte, possono facilmente andare incontro a rottura. Per affrontare questo problema, il processo di fabbricazione è stato ulteriormente ottimizzato, al fine di introdurre dei canali attorno alle isole, in modo da accomodare la pressione applicata.

Questa soluzione si è rivelata adeguata nel contrastare la delaminazione e nel ridurre l'intensità della deformazione.

Le prime evidenze a supporto dell'introduzione dei canali anti delaminazione sono giunte dalle analisi agli elementi finiti, eseguite in ambiente COMSOL Multiphysics. Questa tecnica numerica consente di simulare il livello di deformazione nella membrana sotto sforzo. Confrontando le sezioni della membrana con e senza i canali anti delaminazione, è stato osservato come queste strutture siano in grado di ridurre fino al 50% il picco di deformazione in prossimità dell'isola.

Fra le principali applicazioni biomedicali dell'elettronica estensibile vi sono i dispositivi impiantabili. Protesi retiniche in grado di adattarsi alla concavità dell'occhio, impianti cocleari capaci di seguire la crescita del bambino senza dover richiedere di intervenire chirurgicamente dopo il primo impianto e sonde per la stimolazione celebrale profonda, rispettose della natura soffice e delicata del tessuto celebrale, sono applicazioni verso le quali ricercatori e compagnie private stanno investendo le proprie risorse, andando ad ottenere risultati sempre più affidabili.

Il campo delle neuroprotesi non è il solo a poter beneficiare dei vantaggi offerti dall'elettronica estensibile. In questa tesi viene infatti dettagliata la realizzazione di un MEA per test farmacologici di cardio tossicità. La capacità di studiare cardiomiociti coltivati su un MEA estensibile prima, durante e dopo deformazione meccanica, porta con sé importanti aspettative nel fornire nuove intuizioni riguardo ai test farmacologici di cardio tossicità. Nel corso degli ultimi anni, si è purtroppo reso necessario arrestare lo sviluppo di numerosi farmaci nelle ultime fasi di test preclinico, o addirittura successivamente alla loro commercializzazione, a causa degli effetti indesiderati del farmaco sulla durata dell'intervallo QT nel ciclo cardiaco, potenziale causa di aritmie mortali. Al fine di studiare gli effetti farmacologici sull'intervallo QT, sono stati sviluppati diversi modelli focalizzati sulla misurazione del potenziale d'azione extra cellulare di cardiomiociti derivati da cellule staminali umane (hESC), coltivate su tradizionali MEA rigidi. Questi modelli non dispongono della possibilità di allineare le cellule, fondamentale al fine di ottenere strati anisotropi di cardiomiociti, così come si presentano nel tessuto cardiaco in vivo. Non è inoltre possibile, data la rigidità della piattaforma, applicare stimoli meccanici alle cellule, aspetto non trascurabile dal momento che gli effetti cardio tossici di alcuni farmaci possono presentarsi soltanto con estensioni e contrazioni tipiche del muscolo cardiaco. Un MEA estensibile permetterebbe di superare gli attuali limiti dei modelli già esistenti: la sua

biocompatibilità e le sue proprietà meccaniche, decisamente più vicine a quelle dei cardiomiociti, rispetto a rigidi strati vetrosi dei MEA tradizionali, permettono una maturazione nettamente migliore dei cardiomiociti derivati dalle staminali. Un vantaggio di grande importanza, se si considera che molte patologie possono essere studiate soltanto oltre un certo livello di maturazione del cardiomiocita. In aggiunta, una membrana estensibile può essere rigonfiata pneumaticamente, simulando sia condizioni fisiologiche sia condizioni patologiche (come l'eccessivo stiramento del tessuto cardiaco). Infine, il silicone può essere lavorato in maniera tale da permettere alle cellule di raggiungere un allineamento desiderato, creando uno strato anisotropo nettamente simile alla condizione in vivo.

L'organizzazione della tesi è la seguente:

- L'introduzione presenta la sfera dell'elettronica estensibile, considerando diversi approcci discussi in letteratura e analizzando diverse soluzioni per l'integrazione di isole rigide in substrati elastomerici, oltre che la realizzazione di elettrodi ed interconnessioni estensibili.
- Materiali e Metodi offre al lettore la possibilità di comprendere appieno le proprietà dei materiali utilizzati nel progetto e le procedure alle quali si è ricorsi durante la lavorazione del dispositivo. Il comportamento meccanico del PDMS è ampiamente trattato, assieme a quello dei materiali candidati al ruolo di isole rigide e degli ossidi. Le procedure alle quali si è ricorso in ambiente *clean room* sono infine dettagliate.
- Gli esperimenti complementari abbracciano tutte le procedure svolte a monte e a conclusione del processo di fabbricazione. La progettazione della maschera è essenziale al fine di svolgere le operazioni di fotolitografia durante il processo di fabbricazione; le simulazioni agli elementi finiti offrono invece una conoscenza a priori circa il comportamento della membrana sotto sforzo. La teoria del test di rigonfiamento, sfruttato per calcolare la deformazione del PDMS, è dettagliata, assieme alla descrizione delle apparecchiature strumentali sviluppate al fine di raccogliere i risultati.
- I risultati mostrano il comportamento dei dispositivi al variare dello spessore del substrato e della forma delle isole, oltre che i benefici apportati dall'introduzione delle strutture anti delaminazione.
- Applicazioni dell'elettronica estensibile introduce il lettore nei due principali campi di applicazione: il primo è quello del MEA estensibile per test farmacologici di cardio tossicità. Vengono affrontate le sfide tecnologiche di questa procedura, assieme agli

aspetti biologici riguardanti la manipolazione delle cellule staminali. Infine, anche il settore dei dispositivi impiantabili viene descritto.

- Le conclusioni offrono la possibilità di riassumere i risultati tecnologici ottenuti, proponendo ulteriori sviluppi del progetto al fine di ottenere un dispositivo completamente funzionante.

Questo progetto di tesi, i passaggi sperimentali e le prove tecniche di questo lavoro, hanno avuto luogo al PHILIPS Innovation Center, nei laboratori delle tecnologie MiPlaza. Queste infrastrutture sono collocate all'interno dell'High Tech Campus di Eindhoven, nei Paesi Bassi.

ABSTRACT

This project approaches the realization of a smart and stretchable multi-electrode array (MEA) through a feasibility study. Traditional electronics components are stiff, they have no possibility to stretch or bend without compromising their functionality. Interactions with the human body for implantable devices, as well as with living cells in tissue-making applications, require an approach able to integrate traditional electronics components, such as transistors, amplifiers and electrodes, with biocompatible structures able to bend or even stretch. Our project goal lied in embedding stiff, thin and small structures, called stiff islands, in a thicker elastomeric substrate; this task requires two main steps to be accomplished; the first one refers to the development of a micro-fabrication process able to produce and optimize the desired device. The second step asks for testing the chips under several stress conditions, in order to understand the device's properties evaluating different configurations.

Stiff islands represent future circuitry in terms of mechanical properties and dimensions; if they are able to remain embedded inside the elastomeric substrate without breaking or detaching when the membrane is bended or stretched, they provide important evidences that future electronics, under the same stress conditions, can work without fail. These islands are designed to create an ordered matrix of components; several configuration have been designed, fabricated and tested, changing the dimensions of the islands, their shape and the distance between them. These islands have been realized in two different materials: Poly-silicon and Silicon Nitride. There are mainly two reasons why these materials have been used for this purpose: first of all they are traditional materials used for MEMS application and totally compatible with clean room processing. Secondly, they share a stiffness similar to one of traditional electronics components. The smart concept means that on the same island several electronics can be implemented, i.e. integrating electrodes able to record signals, analog amplifiers and filters followed by analog to digital converters. This smart approach dramatically reduces the amount of interconnections required, increasing the performance of the overall structure. The stretchability is provided by the material in which these islands are going to be embedded. In place of a stiff silicon substrate, typical of traditional approaches, silicone (PolyDiMethylSiloxane also called PDMS) is used. PDMS has a proven biocompatibility and due to its mechanical properties it can extend and stretch, elastically adapting a wide range of applied forces. PDMS is not the only material

involved in substrates production. Also Polyamide and Parylene are valued options for these applications. Differently from these last two materials, PDMS is relatively new and with less literature background; however its mechanical properties, as explained in the following chapter, make it able to give significant contribution to these applications, moving from flexible electronics, a field in which components can just bend, to stretchable electronics, where devices can be stretched and twisted, increasing the number of solutions that can be implemented. Hence, stiff islands represent a cheap and easy-to-make solution to test whether stiff components can remain embedded in a stretchable substrate under stress condition, without break or detach. If none of these events takes place, circuitry can finally be implemented, letting the device operate properly.

Two opposite approaches can be pursued to get stiff islands on a stretchable substrate. The first one is to build the device structure directly on polymer films supported by rigid substrate. A major problem is that the maximum temperature tolerated by polymers is typically 150°C or less, much lower than what is needed in many standard silicon-based fabrication procedures. Studies in this area focused on developing low-temperature process and materials. The consequent low charge carrier mobility usually compromises device performances. To avoid this problem we focused on a second approach, introducing the polymer (PDMS in our case) after all the high-temperature fabrication steps have been completed. Therefore, we developed a fabrication process based on traditional clean room activities, and then we introduced the elastomer, fulfilling our need of stretchability. We started from a fabrication sequence used by [1] to integrate metallic interconnects in PDMS; we updated and shaped this process to get our stiff islands embedded in the silicone layer. The fabrication process can be seen as a system that takes stiff Silicon wafers with Thermal Oxide grown on both sides as input and gives stiff islands embedded in stretchable Silicone as output. After the results of the first fabrication sequence, we improved the fabrication process replacing Thermal Oxide with PECVD Oxide as etch stop layer. The etch stop layer is the material placed in between Silicon and stiff islands; when Silicon is removed with an etching process this layer prevents stiff islands to be affected, interrupting the etching at its surface. Thermal Oxide is characterized by a high compressive stress inside its volume; however this force is prevented to be released until this material is in contact with Silicon. Once Silicon is removed, compressive stress can finally be released. Wrinkles and cracks start to take place and they can even reach and compromise the islands. This problem has been overcome by replacing Thermal Oxide with PECVD Oxide, a material with an

almost null compressive stress. Results supported this explanation; neither wrinkles nor cracks took place with the new fabrication process we adopted.

After the fabrication, devices need to be tested. Conventionally, for this purpose two different tests can be performed. The first approach is the tensile test, whereby a sample with known geometry is loaded at its both ends by an increasing force, while the change in its length is recorded. However, in this project, the fabrication process performed and the small size of the elastomeric membrane do not allow us to peel off the flexible part of the device from the surrounding. As alternative to the tensile stress test, the bulge test technique was implemented in this project. In this technique a pressure is applied to the elastomeric substrate containing stiff islands, which resulted in change of the inflection height of the membrane. Positioning the inflated chip under a microscope, as we did, allowed us to study the behavior of the substrate under stress condition, and to measure the inflation high as function of the applied pressure. The set-up we projected acts clamping the device applying a vacuum at its borders; meanwhile, at its center, the free-standing membrane is inflated by a positive pressure that can be manually adjusted. The bulge test equation allowed us to deduct the strain of the membrane according to the inflation high we measured. This equation considers the inflated membrane as a circumference arc, therefore it works until the inflation high is lower than the ray of the free-standing membrane (half of its length). When this value becomes bigger, the inflated membrane assumes an oval shape and the strain cannot be deduced anymore using the bulge test equation. In case of islands integrated in the substrate, the strain is not homogeneous through the membrane cross section. Islands are stiffer than the substrate, thus their deformation is almost null. The substrate has to accommodate this deformation with higher strain; therefore we updated the bulge test equation considering the amount of stiff material in the membrane cross section and deducing the strain of PDMS. The main results we observed performing these analysis were related to the membrane's thickness and the effects of islands' shape.

Membrane thickness can be adjusted during the deposition of PDMS on top of the wafer; this target is achieved regulating the speed of the spin-coating process. Thicker layers require higher pressure in order to reach the same inflation high, as well as the same strain, than thinner layers, during inflation procedures. If its membrane is conceived to be exposed to high pressure levels without compromising its functionality, thick membrane (above 80 μm) can represent the correct option. In fact the strain in this membrane will be lower, preserving the PDMS from scratching. On the other hand, if the membrane has to reach high values of deformation, for example in case it has to be

constantly inflated, thinner substrates are preferable. Lower pressure will be required, also reducing the energy consumption.

The island's shape revealed interesting outcomes. Three different shapes have been tested: circle, square and rounded square. We already know the advantage of square islands is to offer higher surface area able to accommodate more circuitry. On the other hand circle islands show a lower peak strain when a pressure is applied to the membrane. Starting from these premises, rounded square islands seem a good trade-off between these two parameters. However, performing the bulge test, we observed the strain distribution needs to be considered even more than the peak strain. In square islands the strain is confined in sharp regions close the corners; conversely the strain distribution in circle and rounded square islands involve bigger regions, causing the islands to delaminate from its substrate. Delamination is a risk we should avoid: the island can detach compromising the performance of the device and interconnects can easily break. In order to tackle this problem, we further adjusted the fabrication process, introducing a membrane indentation all around the islands. We observed these indentations able to reduce the peak strain, positively affecting the level of delamination.

First evidences supporting the idea of the aforementioned *anti-delamination* structures came from Finite Element Method analysis we performed with COMSOL Multiphysics. This numeric technique allowed us to simulate the strain level of the membrane under stress condition. Comparing the cross sectional strain of the membrane with and without these indentations, we observed these structures can reduce up to 50% the peak strain around the islands.

Potential biomedical applications of stretchable electronics lie in the field of implantable devices. Retinal prosthesis able to adapt to the concave shape of the eye, cochlear implants capable to follow the growth of the child requiring no other surgery after the first implantation and probes for deep brain stimulations, respectful of the soft and delicate nature of the brain, are all purposes researchers and private companies are investing on, getting increasingly reliable outcomes.

However, the field of neuroprosthesis is not the only one that can benefit from the advantages of stretchable electronics. In these report we detail the realization of a stretchable MEA for cardio-toxicity drug screening applications. The ability to study cardiomyocytes cultured on a stretchable multi-electrode array prior to, during and after mechanical deformation, holds great promise for providing new insights in cardio-toxicity drug screening. During the past years, the development of several drugs has

been aborted in late phases of preclinical testing or clinical trials, and even post-marketing due to undesirable effects on QT interval in the cardiac cycle which may incur life threatening arrhythmias. To study the effects of drugs on QT interval, model systems based on measuring the extra-cellular field potential of the human embryonic stem cell (hESC) derived cardiomyocytes cultured on standard rigid MEAs are available. However, these systems firstly lack the capability of alignment of the cells which is important to obtain functional sheets of cardiomyocytes mimicking the heart tissue. Secondly, they cannot apply mechanical stimulation on the cells, which is of importance since cardiotoxic effects of drugs may only become apparent during actual cardiac muscle stretching and contraction as occurs in vivo in the beating heart. A stretchable MEA allows to overcome many of these limits: its biocompatibility and its mechanical properties, closer to the cardiomyocytes' ones than the traditional stiff glass plates, allow the cardiomyocytes to mature better. This is an important advantage, as some diseases can be seen only when these cells reach a certain degree of maturation. Moreover a stretchable membrane can be pneumatically inflated, simulating either physiological or pathological situations (e.g. excessive stretch etc.). PDMS can be patterned to allow the alignment of these cells, creating an anisotropic layer closer to in-vivo conditions.

The organization of the thesis is the following:

- Introduction presents the field of stretchable electronics, considering different approaches in literature in terms of stiff islands integrated in a substrate, stretchable interconnections and electrodes.
- Material and Methods offer the reader the possibility to understand the properties of the materials involved in the project and the procedures that allowed us to achieve our results. PDMS behavior is deeply analyzed, together with candidate materials for etch stop layer and stiff islands. Clean room techniques, exploited during the fabrication process, are described.
- Complementary Experiments considers all the procedures we performed before and after the fabrication process. Mask design was essential in order to run all the lithography steps while fabricating our devices; meanwhile FEM simulation offered a-priori knowledge about the membrane behavior under stress conditions. The theory of bulge test we used to calculate the strain in PDMS is explained, together with the instrumentation set-up we developed to collect the results.
- Results show what we inspected changing the substrate thickness and the islands shape, as well as the benefit from the anti-delamination structure.

- Application of stretchable electronics introduces the reader in two main field of application. The first one is a stretchable MEA for cardio-toxicity drug screening application. We discuss the technological challenges inside this task, together with the biological issues referring to stem cells manipulation. Finally, implantable devices, such as neuroprosthesis, are depicted.
- Conclusions offer the reader the possibility to summarize the technological results we collected, proposing further development of the project in order to achieve a complete working device.

The thesis project, its experimental steps and the technical experiments of this work, have been performed at the PHILIPS Innovation Center, MiPlaza Technology Laboratories. These facilities are located at High Tech Campus – Eindhoven, the Netherlands.

1. INTRODUCTION

The purpose of this chapter is to introduce the reader in the technological background of the project. State of art of stretchable electronic allows to understand the potential of this field and the question still need to be addressed. Comparison among different approaches available in literature helps the reader to focus on the technology behind this thesis; integration of stiff islands in a stretchable substrate, stretchable electrodes and realization of stretchable interconnects are the three main challenges taken into account.

1.1 STRETCHABLE ELECTRONICS, A LITERATURE REVIEW

Biology is soft, elastic, and curved; silicon wafers are not. An electronics technology that overcomes this fundamental mismatch in mechanics and form will enable applications that are impossible to achieve with hard, planar integrated circuits that exist today [2]. Establishing the foundations for this future in electronics represents an emerging direction for research, much different from the one dictated by the ongoing push toward smaller and faster devices that are still confined to the planar surfaces of the silicon wafers. A main challenge to implement stretchable electronics is how to integrate stiff and fragile device materials such as silicon with compliant elastomeric substrates such as silicones [3]. To appreciate how this aspect relates to engineering challenges, consider that the modulus of silicon is $\sim 100,000$ times as high as a typical elastomer; the thermal conductivity is ~ 1000 times as great, and the thermal expansion coefficient is ~ 100 times as small. Such extremes mismatches in properties lead to interesting, and similarly extreme, behavior in systems that intimately integrate these similar materials [2].

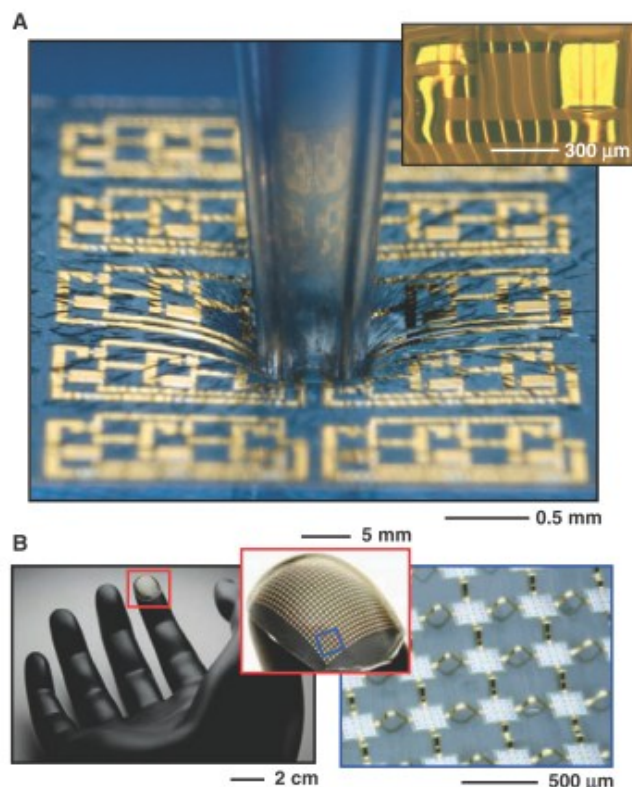


Figure 1.1 - Examples of stretchable electronics. A) Stretchable silicon circuit in a wavy geometry, compressed in its center by a glass capillary tube (main) and wavy logic gate built with two transistors (top right inset). B) Stretchable silicon circuit with a mesh design, wrapped onto a model of a fingertip, shown at low (left), moderate (center) and high (right) magnification. The red (left) and blue (center) boxes indicate the regions of magnified views in the center and right, respectively. The image on the right was collected with an automated camera system that combines images at different focal depths to achieve a large depth of field [2]

Furthermore, today's electronic industry, whether on semiconductor substrates or large-area glass plates, is based on a planar technology, and has been optimized for stiff and flat formats. Extreme mechanical properties can be achieved in fully formed, high-performance integrated circuits by the use of optimized structural configurations and

multilayer layouts (Figure 1.1), even with intrinsically brittle but high-performance inorganic electronic materials from the traditional electronic industry [4].

Stretchable electronics can be achieved in two conceptually different, but complementary, ways. One relies on the use of new structural layouts in conventional materials [5], the other on new material in conventional layouts [6].

Structures that stretch

A simple idea underlies the strategy based on structure and it is an elementary result in mechanics: any material in sufficiently thin form is flexible, by virtue of bending strains that decrease linearly with thickness [2]. A silicon wafer is brittle and rigid, but nanoscale ribbons, wires, or membrane of silicon are stretchable. Configuring such structures into "wavy" shapes and bonding them to elastomeric substrates yields systems that can not only flex but also stretch and compress, with a mechanics similar to that of an accordion bellows (Figure 1.2 A).

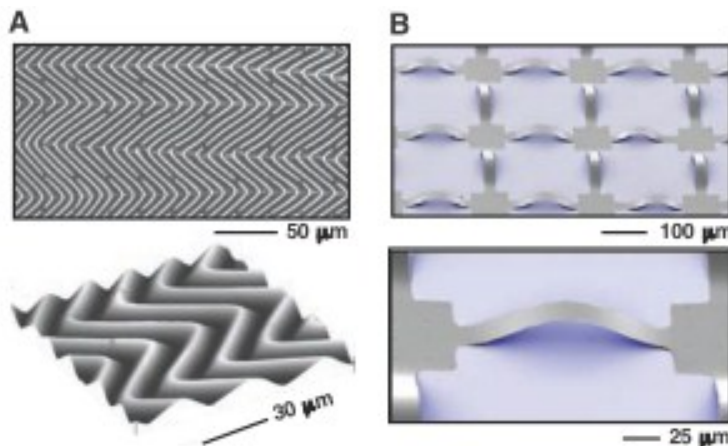


Figure 1.2 - Concepts for stretchable electronic materials. A) stretchable silicon membrane (~100 nm thickness) configured in a wavy shape and bonded to a piece of rubber, presented in optical (top) and atomic force microscope (bottom) images. B) Extremely stretchable silicon membrane (~100-nm thickness) patterned into a mesh geometry and bonded to a rubber substrate only at square pads located between arcshaped bridge structures, presented in moderate (top) and high (bottom) magnification scanning electron microscope (SEM) images. The PDMS is colorized blue [2]

The resulting Si/PDMS construct can be stretched and compressed reversibly, with a linear elastic response to applied force. The amplitudes and wavelengths of the waves change in response to induced deformations in a way that involves considerable strains in the PDMS, but not in the silicon. In particular, mechanics modeling reveals that the peak strains in the silicon can be 10 to 20 times as small as the applied strains. In this approach stretchability is achieved directly in these films of single-crystal Silicon. A schematic fabrication process for such a kind of devices is described by [7] and reported in Figure 1.3. The first step (top figure) involves fabrication of thin (thicknesses between

20 and 320 nm) elements of single-crystal Si or complete integrated devices (transistors, diodes, etc.) by conventional lithographic processing, followed by the removal of the top Si and SiO₂ layers of a Silicon-on-insulator (SOI) wafer.

After these procedures, the ribbon structures are supported by, but not bonded to, the underlying wafer. Contacting a pre-strained elastomeric substrate (PDMS) to the ribbons leads to bonding between these materials (middle picture). Peeling back the PDMS, with the ribbons bonded on its surface, and then releasing the pre-strain, causes the PDMS to relax back to its unstrained state. This relaxation leads to the spontaneous formation of well-controlled, highly periodic, stretchable wavy structures in the ribbons (bottom picture).

A related strategy structures the sheet into a mesh and bonding it to the PDMS only at the nodes. The buckled, arc-shaped interconnecting structures (Figure 1.2 B) can move freely out of the plane to accommodate applied strains of 100% or more, even to values that approach the fracture limits of the PDMS [4].

Materials that stretch

New materials provide an alternative route to stretchable electronics. The most successful approaches use elastic conductors as electrical interconnections between active devices that are rigid or only bendable [2]. Although conductive rubbers based on elastomers loaded with carbon black have been known for decades, the resistances and their dependence on strain are both too large to be useful. In a much more promising and recent approach, long, single-walled carbon nanotubes (SWNTs) serve as conductive dopants in a rubber matrix [8]. Here, WNTs processed by grinding in an ionic liquid and then mixing with a fluorinated copolymer yield a lack, paste-like conductive substance, referred to as a bucky gel [8]. Individual SWNTs form tangled mats in these

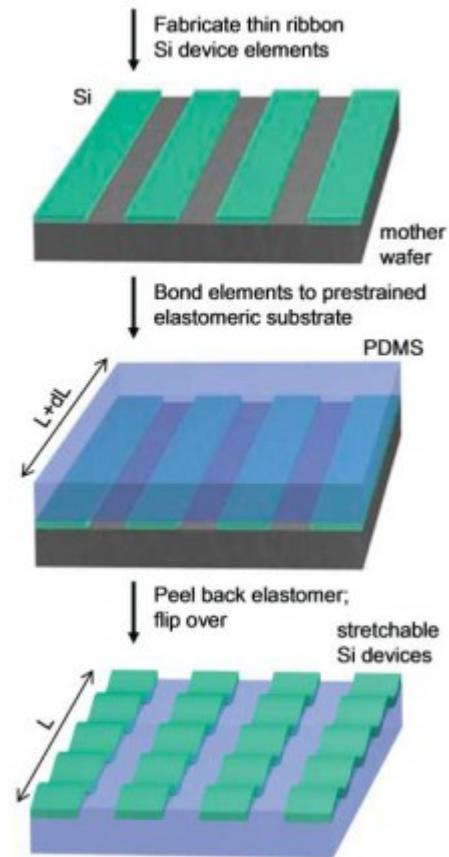
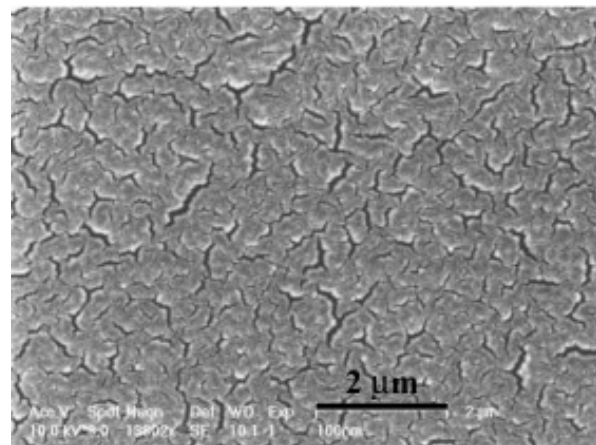


Figure 1.3 - Schematic illustration of the process for building stretchable single-crystal Si devices on elastomeric substrates [7]

gels, with the capacity to reconfigure in response to applied strain in a manner that preserves highly conductive pathways for charge transport. This material can be printed onto sheets of PDMS to yield elastic conducting traces with stretchability in the range of 100%. Alternative, related approaches use SWNTs in thin film networks formed by solution casting or other means.

1.1.1 STRETCHABLE ELECTRODES

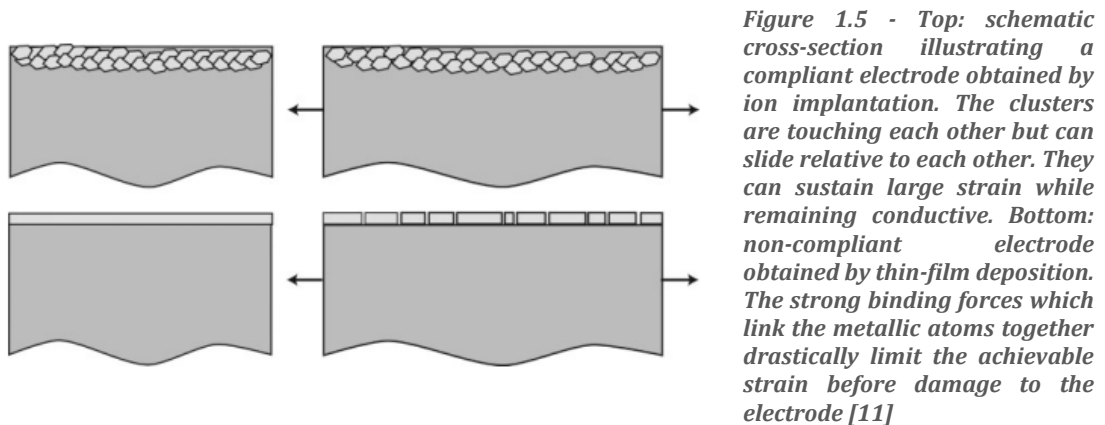
Work in stretchable electrodes, as opposed to electronics, has a comparatively long history and broad range of materials and design options [2]. In fact, the field of stretchable electronics owes its origins to observations that thin films of gold formed by physical vapor deposition directly onto PDMS spontaneously adopt microstructured or nanostructured forms and these structures provide electrodes that can accommodate large applied strains without fracture [9]. Stretchability in this case derives from a physics similar to that of the silicon structures of Figure 1.1 A but



with additional contributions from the motion of microscopic cracks (Figure 1.4) that form in the films during fabrication and subsequent deformation [10]. Recent studies in this field focused on techniques that involve ion implantation to create compliant electrodes [11]. They present a low surface resistant ($< 1 \text{ k}\Omega$ per square) that does not drift in time, they can be stretched up to 175% strain and survive more than 100,000 cyclic deformations to 30% strain and they have a low-to-moderate impact on the Young's modulus of the elastomer on which they are created. The key point of non-implanted electrodes resides in the fact that implantation does not form a continuous polycrystalline film in which grains are attached to each other at the grain boundaries, thus forming a rigid film capable of only a few percent strain before breaking. Instead, ion implantation leads to the formation of small size (2–20 nm) clusters in the polymer matrix. These clusters can touch each other (thus providing a conducting path) without forming a strong mechanical bond. The absence of a strong bond between clusters allows them to slide relative to each other (Figure 1.5). This leads to a reduced impact on the stiffening (increase of Young's modulus) of the PDMS due to the inclusion of the

Figure 1.4 - Scanning electron micrographs of a 100 nm thick Au layer on a PDMS substrate. Microscopic cracks that form in the film can take place during fabrication [9]

metallic particles, and an ability to withstand high strains before losing electrical conduction.



1.1.2 STIFF ISLANDS ONTO AN ELASTOMERIC SUBSTRATE

One way to integrate stiff and fragile material such as Silicon with compliant substrate such as silicones is to distribute rigid subcircuit islands over the polymer surface, and then fabricate active devices on the islands [12]. One of the common fabrication processes is to build the device structure directly on polymer films supported by rigid substrates. A major problem is that the maximum temperature tolerated by polymers is typically 150°C or less, much lower than what is needed in many standard Silicon-based fabrication steps. Therefore studies in this area have focused on the one hand on developing low-temperature processes and materials [13]. On the other hand, in a totally different approach, polymers are introduced after all the high-temperature fabrication steps have been completed. Our project is based on this last strategy; the aim is to gain mechanical flexibility without compromising high device performance.

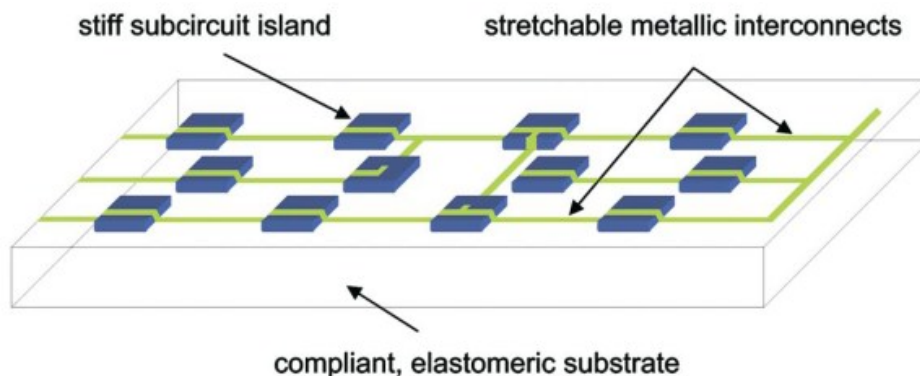


Figure 1.6 - A compliant, elastomeric substrate carries stiff subcircuit islands interconnected with stretchable metallization. Upon deformation, the substrate along with the stretchable interconnects accommodates the resulting tensile, compressive, and shear strains while the islands remain intact [3]

Figure 1.6 sketches the architecture of this stretchable electronics' approach. The substrate is typically a PolyDiMethylSiloxane (PDMS) membrane of thickness $h_{\text{sub}} \sim 1$ mm

and Young's modulus $E_{\text{sub}} \sim 1$ MPa. Embedded in the membrane are subcircuit islands of a stiff material, on which devices are fabricated; the combined thickness of the island and the devices may be as small as $1 \mu\text{m}$. Stretchable metallization electrically connects neighboring subcircuits. When the structure is deformed by a large strain, the islands deform by small strains and remain intact, while elongation and compression are distributed in the substrate and interconnections.

Separate Silicon islands can be fabricated containing conventional integrated circuits [14]. These islands are typically $200\text{-}300 \mu\text{m}$ thick. The island material should preferably be an electrical insulator that can be deposited with thin-film techniques at low substrate temperature, to be compatible with the organic substrate. According to [3], the stiffness S of a layer of a material with thickness h and Young's modulus E is characterized by the product $S= Eh$. Assuming the thickness of the substrate about 1 mm and a 250 nm thick film; for the film to be stiffer than the substrate, the film should have a Young's modulus at least 4.000 times that of PDMS; i.e. $E_{\text{film}} > 4 \text{ GPa}$. Candidates for the island material include Silicon Oxide ($E_{\text{SiO}_2} \sim 70 \text{ GPa}$), Silicon Nitride ($E_{\text{Si}_3\text{N}_4} \sim 200 \text{ GPa}$) and diamond like Carbon ($E_{\text{DLC}} \sim 200 \text{ GPa}$) [3]. Finally, island size and density should be optimized to accommodate built-in transistor circuits and prevent crack propagation upon stretching. Typically islands larger than the substrate thickness crack because of shear stress pulling on the island during stretching. Also high island density reduces the yield of intact island during deformation.

1.1.3 STRETCHABLE INTERCONNECTS

Notwithstanding the aim of this project was focused on a membrane able to integrate stiff islands inside an elastomeric substrate, interconnection between these islands represent the natural extension of this device, transferring signals among the islands and outside the device as well.

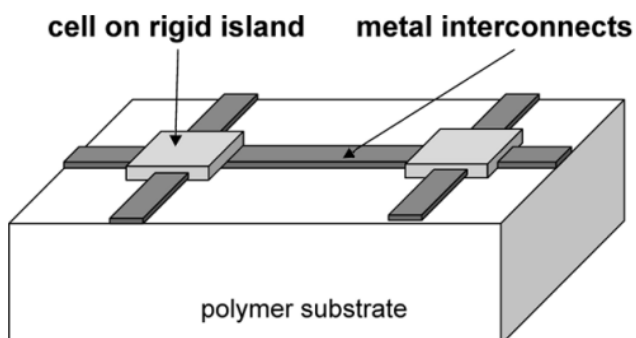


Figure 1.7 - Architecture of an elastic electronic surface made on a polymer substrate. Active device cells can be fabricated on rigid subcircuit islands distributed over the polymer surface. The cells are interconnected with stretchable metallization [12]

A complete stretchable device, in fact, reproduces the base structure depicted in Figure 1.7, using interconnections among the islands for the aforementioned purposes. Metals

revealed as the best option to realize interconnections because of their high electrical performance and relatively low cost [15]. The main challenge is maintaining the integrity of the circuit during and after flexing or stretching the substrate. Several approaches in this field have been studied; we are now introducing the most promising ones in order to have an overview of these researches.

Horse-shoe shaped metallic wires in a stretchable substrate material

Even if simple conductor shapes like triangular or sinusoidal allow higher deformation compared to a straight line, they present a high concentration of stresses in the crest and trough, giving rise to early failures at fairly small deformations; therefore a design of an appropriate shape is crucial to allow stretchability of the conductors [15]. In the work of [15] three different conductor shapes have been considered: elliptical, U-shape and horse-shoe. 3D FEM simulations have been performed in order to address the most promising structures that have been mechanically tested and optimized later on.

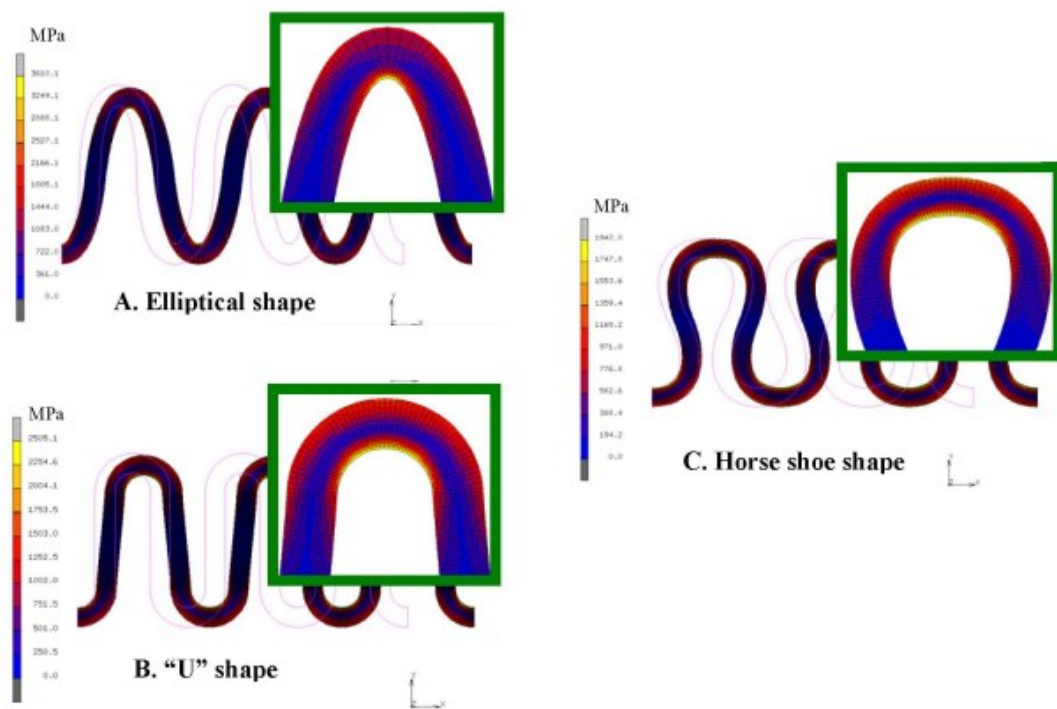


Figure 1.8 - Stress distribution in copper conductor line for three different conductor shapes [14]

In this approach the substrate material (PDMS) is introduced at the end of the fabrication process, when the interconnections have already been patterned, in an approach quite close to the one we pursued integrating our islands in PDMS. A total deformation of 20% was applied in the axial direction of the meander for all the three shapes, getting the results showed in Figure 1.8. These results revealed the horse-shoe

shape has the optimal distribution of the stress along the conductor, reducing the risk of failure of the interconnection under stress.

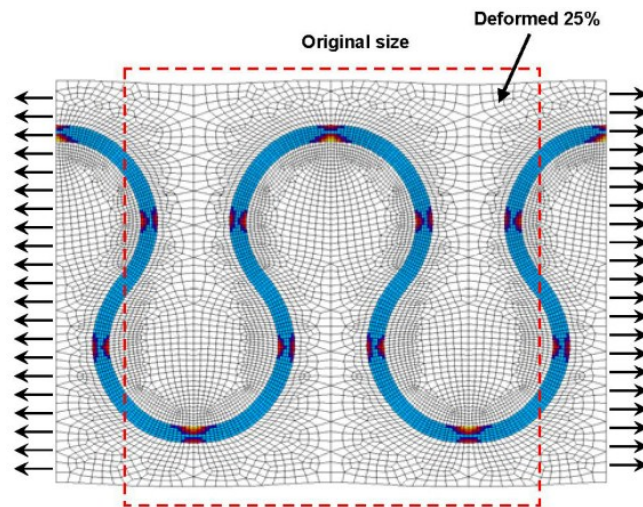


Figure 1.9 - Poisson effect observed during a uniaxial tension test [15]

In order to quantify the strains also the substrate has to be included. During a uniaxial stretching, metal conductor revealed in tension in the crest and trough and in compression in the center of the design. Yellow and red colors in Figure 1.9 represent a concentration of plastic strains when the structure is stretched 25%. The red dashed line indicates the original dimension of the structure.

A qSSA qualitative comparison between modeling and experiments shows that calculated region with high concentration of plastic strain (higher than 10%) correspond to the observed failures (Figure 1.10).

Stress shielding for metal interconnections

The idea to introduce, during the fabrication process, an additional layer of Parylene to deflect the stress away from the interconnections was the approach used by [16]. Since the Parylene can absorb much higher stresses, it can be used to deflect stress away from the fragile interconnections.

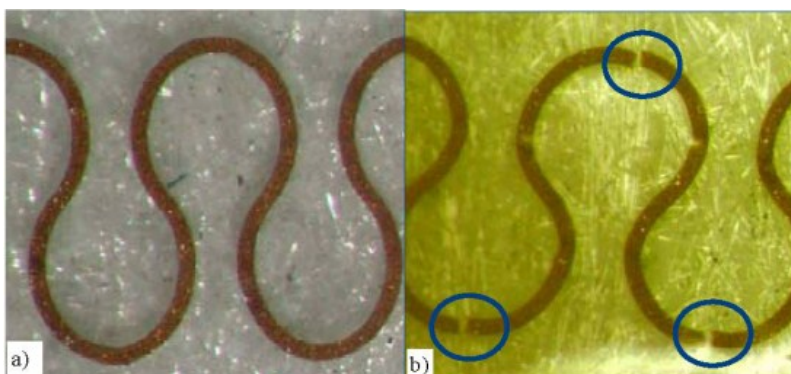


Figure 1.10 - Tensile strain test of horseshoe metal interconnects. A) Before elongation. B) After 25% elongation highlighting the failures in the crest and trough

Parylene, in fact, has mechanical properties in between the flexible substrate and the metal connections, especially in terms of Young's modulus, as reported in Table 1.1. Since Parylene can absorb much higher stresses, it can be used to deflect stress away from the fragile interconnects. This additional degree of freedom can be used to create interconnect structures which as a whole can withstand much higher strains.

YOUNG'S MODULUS	
PDMS	1.2 MPa
ALUMINUM	70 GPa
PARYLENE	3.2 GPa

Table 1.1 - Properties of the materials involved in the study from [16]

Several configuration of Parylene have been analyzed, comparing the strain inside the interconnection with the situation in which the membrane is made just by Aluminum and PDMS. Embedding the wire in a $3 \times 3 \mu\text{m}$ Parylene structure revealed as the best solution, allowing a 78.8% reduction in stress once a 30% strain is applied, proving Parylene can be used to positively influence the stress-level of a metal interconnect in a stretchable PDMS substrate [16].

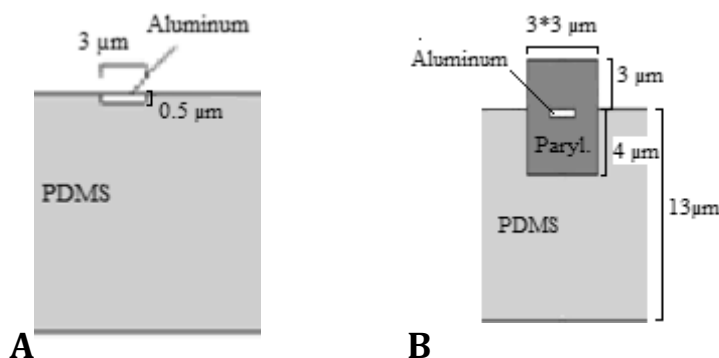


Figure 1-12 - schematic cross-section from the middle of the reference structure. A) Without any stress-shielding B) Embedding the interconnect in Parylene

Metal interconnection directly patterned on elastomeric substrate

Several strategies for elastic interconnects have been developed and patterned directly onto the elastomeric substrates [17]. S. P. Lacour et al. studied the stretchability of thin gold films (thickness $< 100 \text{ nm}$) on elastomeric substrates, particularly PDMS [3, 9]. A 1-mm-thick PDMS membrane was prepared and no surface treatment was performed before metal deposition. Thin gold films (typically 25-500 nm) are deposited in one run by successive electron beam evaporation on the PDMS hold at room temperature. Once the metal is deposited, a network of randomly arranged micro-cracks (Figure 1.11) starts to cover the surface of the gold stripe [12]. The micro-crack pattern in the metal film allows the film to elongate by deflecting and twisting out of plane, such that a large

applied elongation only induces small and elastic strain in the film[9]. This out of plane twisting and bending is only possible on an elastomeric substrate with very high compliance. Lacour performed thin metal deposition both on relaxed and pre-stretched (10% - 25% uniaxial pre-stretch) substrates.

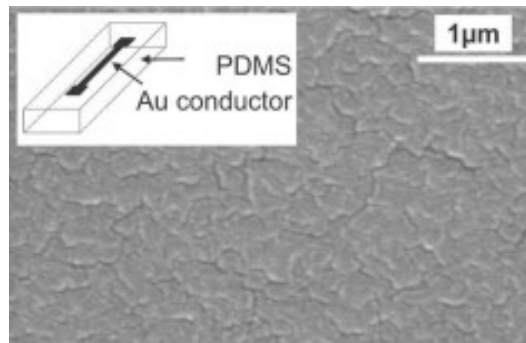


Figure 1.11 - SEM micrograph of the as-prepared 25 nm thick gold film on PDMS. The gold ligaments percolate between the micron-size micro-cracks [10]

When the substrate relaxes from pre-stretch, the gold stripes form surface waves. Experiments illustrated the astonishing stretchability of thin gold conductors on PDMS membrane [12]; however both techniques produced highly stretchable interconnects, without possibility to address which one of them performed better.

2. MATERIALS AND METHODS

This chapter discusses the technological background from which this project arises. The production of the device implies a choice among different materials and methods in order to get a result that is able to answer the demand of improvements in terms of reliability and mass production. In light of this all the materials used and their valued alternatives are going to be showed, analyzing the state of art of their properties' knowledge. Initially, an introduction about strength of materials is provided. This part allows the reader to have a better understanding of some of the terms involved in the materials' description. A relevant space is dedicated to PolyDiMethylSiloxane (PDMS). This material represents a core technology of this project; its biocompatibility and its ability to stretch are fundamental aspects that allowed us to achieve such results. Also the characteristic of the fabrication processes involved to get the device are described, referring to Microfabrication fundamentals and clean room procedures.

2.1 STRENGTH OF MATERIALS

The ability of a material bar with original cross section area A_0 and length L_0 to stretch can be tested by applying a load F to its both ends. As a result the bar elongates to a new length L and its cross section area shrinks to A , as illustrated in Figure 2.1. The load required for a given elongation, in the elastic regime, is proportional to the original cross section area A_0 of the bar. Under a constant load, the elongation is proportional to its original length L_0 . For convenience the material's response can be expressed independently of the bar's cross section and length. Thus, stress and strain are introduced. Stress σ is defined as:

$$\sigma = \frac{F}{A_0}$$

Its unit of measure is Pa. The strain ϵ is expressed as:

$$\epsilon = \frac{L - L_0}{L_0} = \frac{\Delta L}{L_0}$$

Strain is dimensionless, often expressed in percent % [18].

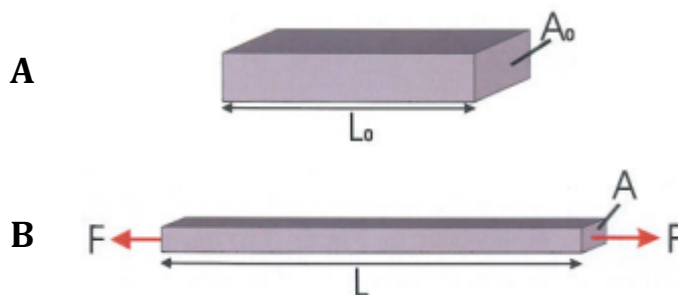


Figure 2.1 - A) A material bar with length L_0 and cross section area A_0 . B) If a load F is applied to both ends of the bar, it is stretched to a new length L and its cross section area shrinks to A [18]

At low value, stress can be related to strain by Hooke's law; elastic deformation takes place.

$$\sigma = E\epsilon$$

E is the elastic modulus, also known as the Young's modulus. At a given strain, for example in the z -direction ϵ_z , the bar's cross section area shrinks in the other two directions. This change is defined as:

$$\epsilon_x = \epsilon_y = -\nu\epsilon_z$$

Where ν is the Poisson's ratio [18]. The applied stress to a material bar can be plotted as a function of the measured strain. This relation is known as strain-stress curve. In Figure 2.2 the stress-strain curve of a metal and a polymer are schematically illustrated [18].

For metals, the elastic deformation is represented by the steep straight line which begins at zero stress and ends at the stress value σ_y , called yield stress. The Young's modulus corresponds to its slope according to Hooke's law. Deformation is in this range reversible upon removal of the applied stress. If a metal is further stretched than its yield stress value, the deformation stays permanent, defined as plastic deformation. The metal sample breaks eventually at elongation at fracture. Polymers exhibit s-shaped stress-strain curves. Metals rupture too early, compared to polymers, especially silicones (e.g. PDMS), which are capable of large strains before break.

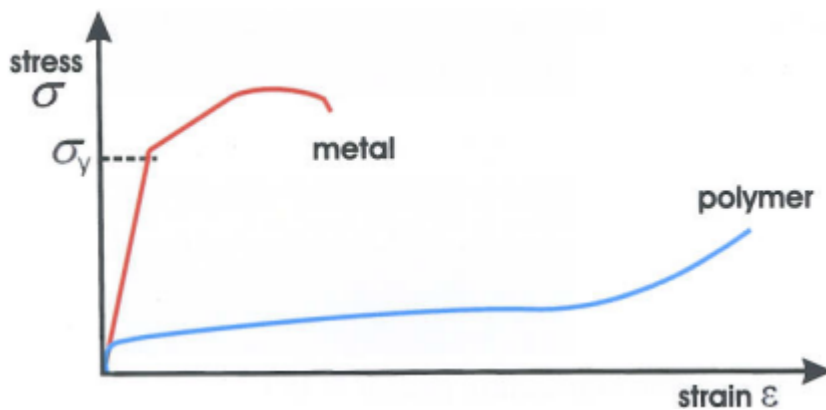


Figure 2.2 - A schematic illustration of the stress-strain curve of a metal and a polymer [18]

2.2 SUBSTRATE MATERIAL

The substrate represents the layer in which stiff islands are embedded; its main purpose is to provide flexibility and stretchability of the overall membrane. However, this material is required not only to be stretchable but also compatible with the clean room processing. Furthermore, considering the biomedical applications of this device, it should not be neither cytotoxic nor a cause of extensive immune response. According to [19] three materials are the main candidates for the role of substrate layer. Their properties are reported in the table below.

MATERIAL	YOUNG'S MODULUS	BIOCOMPATIBILITY	PATTERNABILITY
PARYLENE	3.2 GPa [20]	ISO 10993 [21]	Good
POLYIMIDE	1.3 - 4 GPa [20]	ISO 10993 [22]	Very Good
PDMS	0.75 - 3 MPa [20]	ISO 10993 [23]	Fair [24]

Table 2.1 - Scoring card for three candidate substrate materials

All these materials have been previously studied in literature; i.e. PDMS has been used in the studies from Lacour [3, 9, 10, 12] and Parylene has been chosen by Wang for her stretchable approach [13]. Biocompatibility can represent an ambiguous term, therefore the criteria used to compare these material was their capability to successfully

overcome ISO 10993 tests. All of the materials involved satisfied the biocompatibility requirements, as showed in Table 2.1.

The reason that made PDMS our best choice, as substrate material, is the huge difference in terms of Young's modulus. For this parameter PDMS shows a value three orders of magnitude lower than the ones of Parylene and Polyimide. However, compared to Parylene and Polyimide, PDMS is harder to be patterned during clean room procedures. To overcome this problem the fabrication process has been shaped in a way that introduces PDMS at the end, without any need to pattern the substrate.

2.3 POLYDIMETHYLSILOXANE

PDMS, abbreviated from PolyDiMethylSiloxane is a type of silicone rubber. It belongs to the family of high polymers, which are enormous molecules composed of small atomic groups (called monomer units), joined by covalent bonds. The chemical structure of a silicone is illustrated in Figure 2.3 A. The monomer unit is presented in brackets and the number of its repetition is n . The silicones contain silicon Si and oxygen O atoms, as well as hydrogen, methyl or phenyl groups. The atoms are bended to one another by covalent bonds, indicated symbolically by the lines.

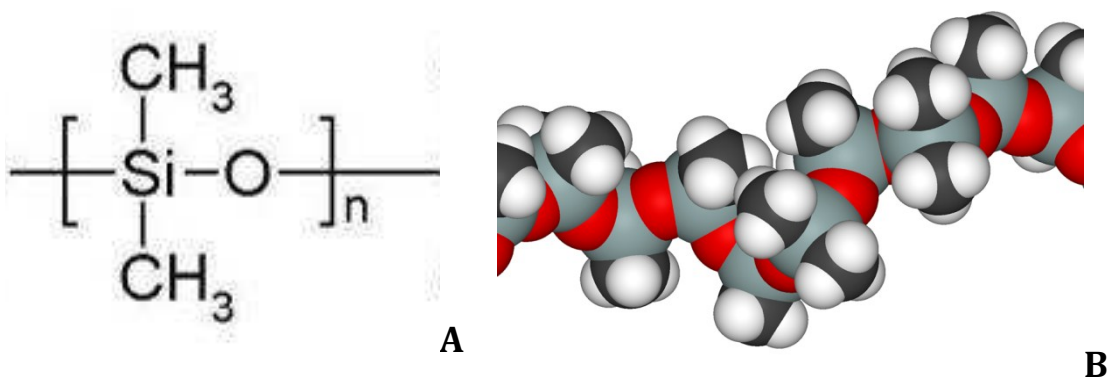


Figure 2.3 : A) Chemical structure of Silicone monomer; B) Space filling mode of a PDMS chain [19]

In the case of PDMS, the number of monomer units is in the range of 5-10.000 (Figure 2.3 B). This silicone can be cross linked, if a suitable initiator is added. During cross linking the two methyl groups react under elimination of H₂. PDMS is stable for a very large temperature range, namely from -180°C to +250°C [25]. The main feature of silicones is their large strain and low elastic modulus. Compared to crystalline materials and most polymers (strain limit of 0.1% and 1% respectively), the silicones can be stretched up to 100% [25]. Therefore, belonging to the family of the silicones, PDMS is very suitable to be used as a stretchable material. PDMS is a silicone elastomer with desirable properties that make it attractive for the development of MEMS and

microfluidics components for biomedical applications [26, 27]. It is chemically inert, thermally stable, permeable to gases, simple to handle and manipulate, exhibits isotropic and homogeneous properties as well as lower cost than silicon, and can conform to submicron features to develop microstructures [27, 28]. In addition, PDMS is transparent, non-fluorescent, biocompatible and nontoxic, and has been traditionally used as a biomaterial in catheters, drainage tubing, insulation for pacemakers, membrane oxygenators, and ear and nose implants [29]. The extensive biomaterial foundation of PDMS in conjunction with the increasing interest in low cost, mass-produced, microfabrication compatible, polymeric MEMS make it formidable and promising material for current and future BioMEMS applications. Consequently, there is significant interest in examining the compatibility of PDMS with both MEMS technology and biomedical applications [30].

2.3.1 PREPARATION

For our project we used Sylgard 184 ® (Dow Corning Corporation, Midland, MI) that is a widely used commercially available brand of PDMS. PDMS Sylgard 184 ® is a heat curable PDMS supplied as a two-part kit consisting of pre-polymers (base) and cross-linker (curing agent) components. The manufacturer recommends that the pre-polymer and cross-linker be mixed at 10:1 weight ratio respectively. The study from [30] showed how mechanical properties of PDMS can be altered by changing the polymer to cross-linker ratio without variations in surface chemistry. Among the entire gamma of cross-linker ratio tested, 14.3:1 revealed as the one that exhibited the highest tensile strength and storage modulus.

The mixture is then spin coated on a Silicon wafer to create a uniform layer of elastomer on the wafer surface. The rotational frequency during the spin-coating phase is the principal parameter that regulates the thickness of the elastomer layer. Typical spin curves show a hyperbolic correlation between the rotational frequency and the thickness of the layer (see Figure 4.17). This corresponds to a thicker layer through fewer rotations and a thinner layer through a higher rotational frequency [31]. Also the viscosity plays a large role in the process of spin-coating layers; it is especially important for the determination of the thickness and homogeneity of a spun layer [31]. To achieve thinner layers at the same spin speed the viscosity could be further reduced by lowering the mixing ratio or diluting the mixture with a low viscosity additive [19].

After spin-coating, PDMS membrane should be cured by an organometallic cross linking reaction, process promoted by heating [32]. This step can be done at different

temperatures; higher temperatures require shorter times. Details are available on the product data sheet [33].

2.3.2 MECHANICAL PROPERTIES

Several studies focused on mechanical properties of PDMS have been performed in recent years [31, 32, 34-36]. These researches focused on the way several factors affect crucial parameters as Young's modulus, viscosity and shear modulus of the elastomer. In order to have a better understanding of the behavior of PDMS, the most interesting results are reported and discussed in this paragraph.

Young's modulus

When utilizing PDMS as an engineering material in microfluidic devices, it is vital to understand how several factors, as cure time, temperature and weight ratio of prepolymer to hardener, affect material stiffness. E.g. the study from [34] revealed that increasing the weight ratio of prepolymer will reduce the stiffness of PDMS.

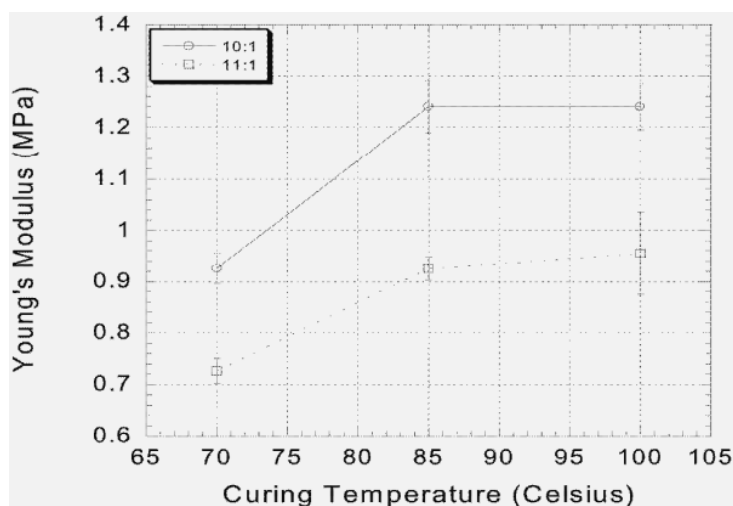


Figure 2.4 - Graph of the Young's Modulus with respect to curing temperature for PDMS with a 10:1 and 11:1 weight ratio of prepolymer to hardener [34]

Although two weight ratios produce different stiffness values, both follow the same trend with respect to curing temperature (Figure 2.4). When cured at 70°C for 200 minutes, however, the Young's modulus is 30% lower than the higher temperature process. Figure 2.5 A shows a trend of decreased stiffness with increasing the prepolymer weight ratio. Also the shelf life of the device was investigated: it is important to understand how the properties of PDMS devices will change with time as a result of physical aging. Samples were held at 100°C for 2, 5, 7 and 14 days and the stiffness data is reported in Figure 2.5 B.

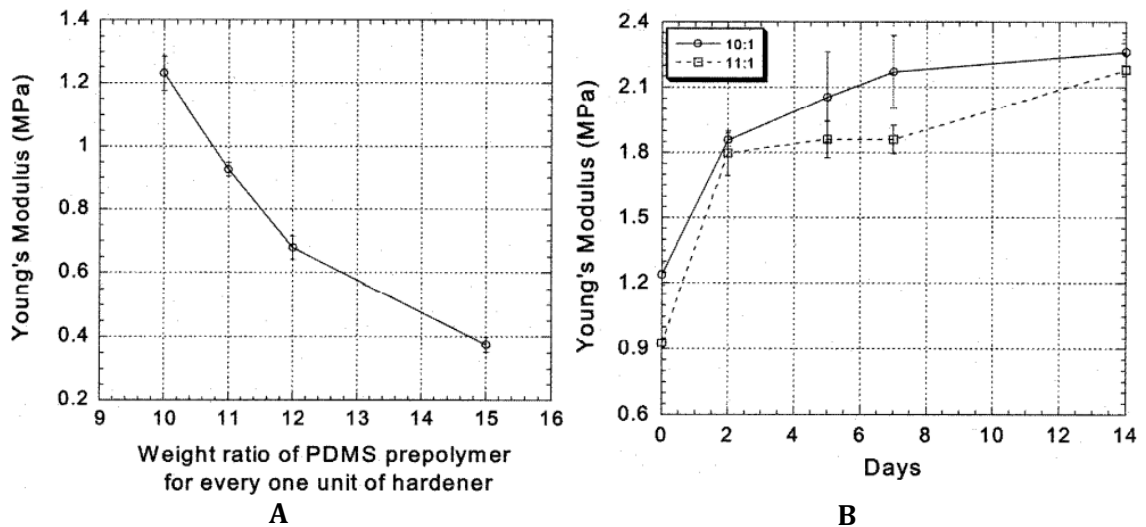


Figure 2.5 - Graph of the Young's Modulus A) with respect to the weight ratio of PDMS prepolymer to hardener for samples cured at 85°C for 100 minutes B) with respect to time aged at 100°C in an air oven for PDMS with a 10:1 and 11:1 weight ratio of prepolymer to hardener [34]

Next, the influence of the temperature on the elastic modulus of Sylgard 184 has been analyzed [35]. The linear dependence of the elastic modulus on the temperature is predicted by the thermodynamic theory laid out in [37]. Therein, the elasticity of rubber is considered solely as an entropic effect. As a result, the elastic modulus for silicones is

$$E = \frac{3}{2}kT\rho_K$$

Where k stands for the Boltzmann constant, T for the temperature and ρ_K for the degree of cross-linking.

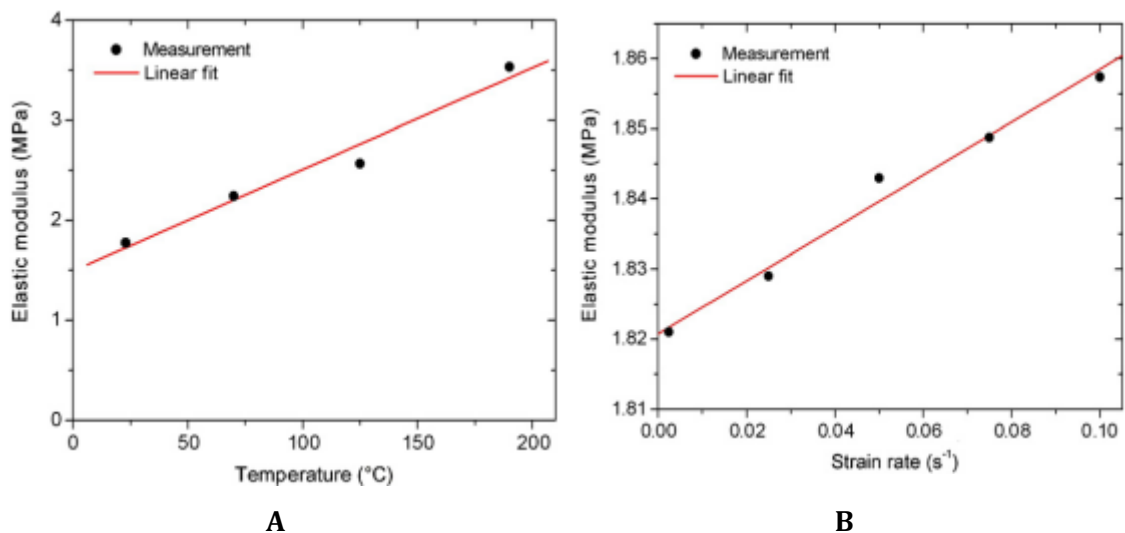


Figure 2.6 - Elastic modulus of Sylgard 184 A) against temperature B) as a function of the strain rate [35]

Tensile test were carried out in a thermo-chamber at different temperature levels; the corrected elastic modulus of Sylgard 184 is plotted as a function of temperature in

Figure 2.6 A. As we can notice from this experiment, silicones display very strong dependence on the temperature, which is typical of visco-elastic materials [35]. In order to study the mechanical visco-elastic properties, also the influence of the strain rate on the elastic modulus has been examined. Figure 2.6 B plots the elastic modulus as a function of the strain rate. This graph shows an increase of the elastic modulus of the 2% with a change in the strain rate in the range of $0.0025\text{-}0.1\text{ s}^{-1}$.

Elastomer's thickness

In the design and actuation of PDMS membranes, the common view is to consider them as bulk material; however this assumption remains unjustified. As the thickness of PDMS membrane becomes thinner and thinner, there is an urgent need to understand whether or not PDMS membranes are dimensional dependent. A research from [32] examined the resistance to deformation of PDMS membranes as a function of thickness, achieving the results showed in Figure 2.7. This picture shows two regimes of the size-dependent strengthening effect that are proportional to the inverse of the square root of thickness.

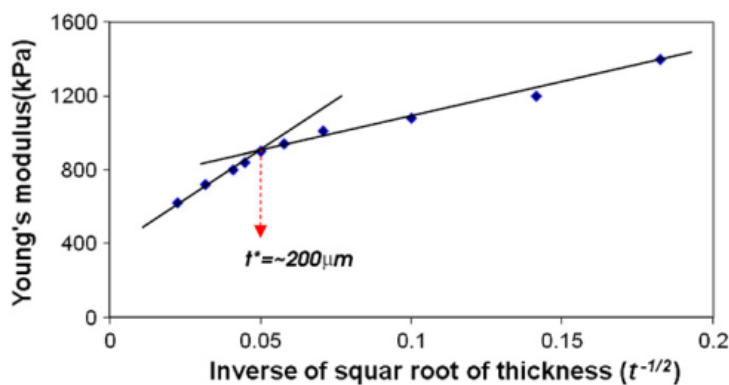


Figure 2.7 - Young's modulus versus the inverse of PDMS thickness, $t^{-1/2}$ ($\mu\text{m}^{-1/2}$). The transition point from size dependent to bulk behavior is predicted to be around $200\text{ }\mu\text{m}$ in thickness of PDMS membrane [32]

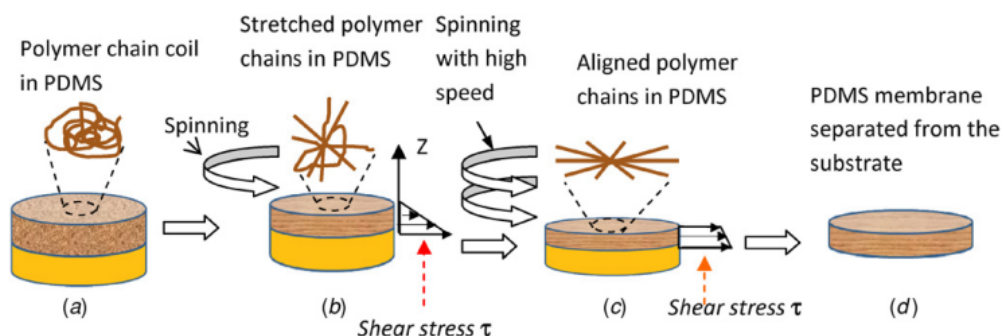


Figure 2.8 - A) Sketch of the PDMS mixture dispensed onto a wafer substrate and tangled polymer chain coils. B) when spinning is applied the PDMS is thinned and polymer chain coils are stretched by shear stress which is a gradient along the thickness (z) direction. C) when a greater spin speed is applied the polymer chains are extensively reordered in the radial direction and the PDMS membrane is thinned further. D) the PDMS membrane with a desired thickness and reordered (alignment) is separated from the wafer substrate [32]

Thicker PDMS membranes produce a negligible strengthening effect. The transition point from size dependent to bulk behavior is predicted to be around 200 μm in thickness.

The explanation of this phenomenon suggested that the effect on the elasticity is caused by the spin speed rather than by the thickness itself, which is controlled by a combination of spin speed and PDMS viscosity. It can be explained as follows: during spin-coating, the random coiled polymer chains present in the PDMS solution are subjected to shear forces due to the relative motion between the spinning wafer substrate and the viscous PDMS mixture. The shear stress of a PDMS membrane during spinning is proportional to the square of the angular velocity[32]. Thinner membranes require greater angular velocity and thus produce greater shear stress. This stretching and realignment of the polymer chains forms stronger cross-linked networks and thus greater mechanical strength translated to higher values of Young's modulus shown during tensile tests. The process behind this phenomenon is explained in Figure 2.8.

2.3.3 METAL THIN FILMS ON POLYMER SUBSTRATES

Free standing metal thin films tend to break at very low strains, due to strain localization which causes the film to thin down at a local spot by forming a neck which eventually leads to rupture of the film [38, 39] (Figure 2.9 A). Due to volume conservation, this local thinning results in local elongation in the order of the film thickness before rupture. Due to extremely small thickness-to-length ratios the overall rupture strain would be just slightly beyond its elastic limit [40]. However, thin metal films bonded to polymer substrates can sustain much higher plastic deformation ranging from a few percent to a few tens of percent [38, 39, 41]. This variation in stretchability of the metal film is due to differences in adhesion of metal/polymer interface.

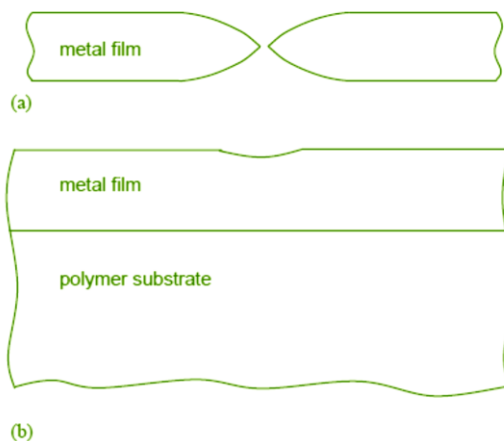


Figure 2.9 - The rapture of a metal film caused by strain localization. A Necking of a free standing metal film, B local elongation is suppressed by the substrate [40]

When a metal film is bonded to a substrate, it cannot have large local elongations, and may therefore deform uniformly far beyond its free standing elastic limit [40] (Figure 2.9 B). For example [41] achieved over 40% of strain without cracking of a 1 μm thick Cu film sputter deposited on a 12.7 μm thick polyimide foil (Kapton 50HN® by DuPont). In their experiments they used a 10 nm thick Cr interlayer sputter deposited prior to Cu deposition to improve adhesion, and also annealed the deposited Cu film at 200 °C after deposition.

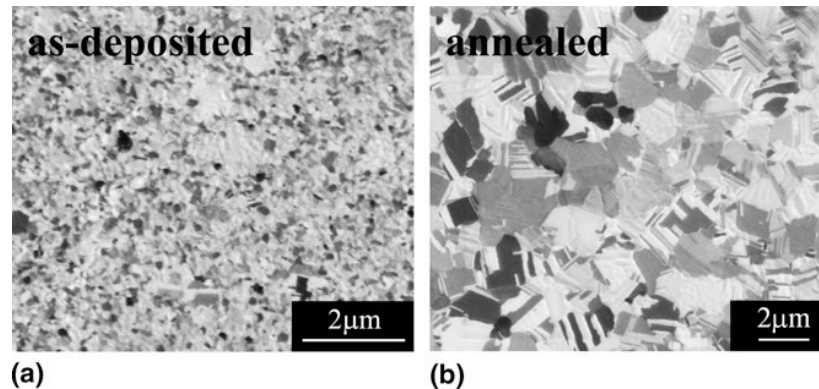


Figure 2.10 - Focused ion beam (FIB) images of (a) as-deposited film and, and (b) film annealed at 200 °C for 30 min. Annealing has caused significant grain growth. Whereas grains have a relatively uniform distribution in the annealed film, isolated large grains can be identified in the as-deposited film [39]

Nanshu Lu et al. [39] studied the mechanisms of rupture of thin metal films bonded to the polymer substrate. According to their study, three accompanying mechanisms are responsible for failure of thin films on a polymer substrate, strain localization at large grains in the microstructure of the film, deformation-induced grain growth, and film debonding from the substrate. They used two types of samples for their experiments, one with Cu film annealed after deposition and one with Cu as-deposited without annealing, both of them without the Cr layer for adhesion improvement. As shown in Figure 2.10, the as-deposited Cu film has a nano-crystalline structure which is unstable and the grains tend to grow under mechanical loading; but, after annealing the grains grow and become stable under mechanical loading [39].

The as-deposited film tends to fail at elongation of around 12%; whereas in the annealed film the cracks start to appear at around 25%. Figure 2.11 shows the change in electrical resistance of the two types of films versus elongation.

The reason of earlier failure of as-deposited film is its unstable nano-crystalline structure compared to the annealed film.

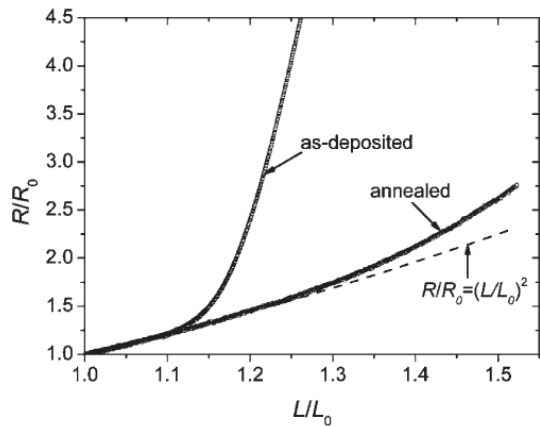


Figure 2.11 - The resistance change versus elongation normalized with their initial values. The curve $R/R_0=(L/L_0)^2$ shows the theoretical prediction of resistance change assuming that no cracks happen in the film. The resistance of the as-deposited film starts to deviate significantly from the theoretical prediction due to emerging cracks at elongation of approximately 12%, whereas the annealed film is much more robust [39]

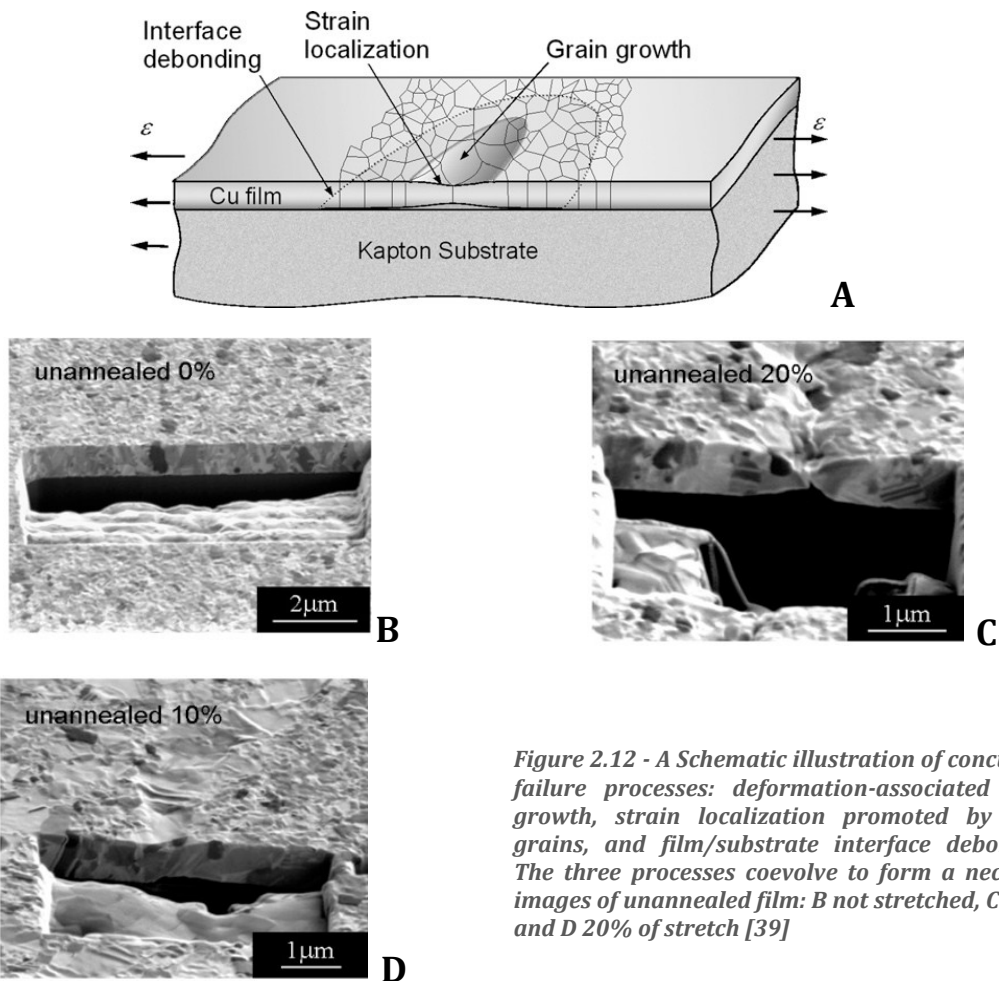


Figure 2.12 - A Schematic illustration of concurrent failure processes: deformation-associated grain growth, strain localization promoted by large grains, and film/substrate interface debonding. The three processes coevolve to form a neck. FIB images of unannealed film: B not stretched, C 15%, and D 20% of stretch [39]

According to Hall-Petch effect, there is an inverse relation between the yield strength and grain size of a polycrystalline material as long as the grain size is above a few tens of nanometer [39]. As a result, the nano-crystalline regions of the as-deposited film have much higher yield strength than the random larger grains in the structure. Under tensile loading the strain tends to initially localize at regions with large grains; then as the localization spreads, large grains start appear in adjacent regions, and gradually necking

happens which causes debonding of the film from the substrate and further local elongation resulting in failure of the film; this is illustrated in Figure 2.12.

2.3.4 STERILIZATION AND EXPOSURE TO CULTURE MEDIA

The research from [30] studied various chemical and physical effects of sterilization on smooth and micro-textured PDMS substrates. The commonly used sterilization methods investigated include: (a) 30 minutes immersion in 70% ethanol at room temperature; (b) irradiation with UV light (254 nm, 100 $\mu\text{W}/\text{cm}^2$) for 30 minutes; and (c) steam auto-clave at 121 degrees centigrade for 20 minutes. The effects of sterilization were analyzed by using SEM (Scanning electron microscopy) to assess micro-texture degradation; goniometry (24 hours after sterilization) and XPS (X-ray photoelectron spectroscopy) to evaluate surface effects; and nano-indentation; tensile testing, and FTIR (Fourier transform infrared spectroscopy) to assess changes in mechanical properties.

The results obtained are summarized as follows: SEM did not reveal any noticeable changes in the micro-texture and surface distortion after applying the three sterilization methods; goniometry showed no significant change of long-term hydrophilicity after any of the sterilization procedures either. But, the results of nano-indentation, tensile testing and FTIR showed that for steam auto-clave the substrates undergo further cross linking which caused an increase in ultimate tensile strength and storage modulus of PDMS. XPS showed that the three major chemical elements on the PDMS surface prior and subsequent to sterilization were Carbon (C), Oxygen (O), and Silicon (Si), and no significant change was observed. So it can be inferred that ethanol and UV do not have any discernible chemical and physical effect on PDMS substrates, but steam auto-clave due to high enrapture causes some further cross linking which can change the mechanical properties of the substrates. [30] has also investigated the effect of culture media on the PDMS substrates chemical composition. Culture media consists of a number of nutrients that are used to provide an appropriate biochemical environment for cells in culture. The PDMS substrate were immersed for 4 days in alpha-MEM Minimum Essential Medium containing amino acids, vitamins, inorganic salts, ribonucleosides, deoxyribonucleoside, and 1% Fetal Bovine Serum. After the immersion period the substrates were washed in deionized water and air dried before XPS analysis. The results of the analysis show that Culture Media immersion does not have major effects on the surface element concentration; except for the presence of nitrogen and an increase in surface concentration of oxygen relative to silicon. The increased presence of N and O can be due to the amino (NH_2) and carboxyl (CO) groups rich in nitrogen and

oxygen, which deposit on the surface of the PDMS from the culture media amino acids and proteins [30].

2.4 SILICON OXIDE

The Silicon Oxide layer played an important role inside the fabrication of our stretchable MEA. In light of the different etch rate of this material compared to the other ones involved in the fabrication of our device, Oxide served as etch stop layer, allowing to isolate the elastomeric membrane, getting stretchability in the device. Two different kinds of Oxide have been used; the first one, Thermal Oxide, is a traditional MEMS material. The second one, called PECVD Oxide, is becoming more and more important inside microfabrication because of its interesting properties.

2.4.1 THERMAL OXIDE

Thermal Oxide, or SiO_2 , is one of the “building block” film used in making both simple and complex semiconductor devices. This Oxide is grown directly on the wafer surface; this process normally takes place in a diffusion furnace, requiring a temperature between 800°C and 1200°C using either wet or dry growth method. Thermal Oxide growth occurs at the Silicon/Oxide interface where it actually grows from the bottom-up and each new layer is pushed-up instead being deposited or piled-on, like PECVD Oxides. As the reader can notice in Chapter 4, after the first fabrication sequence, this layer has been replaced with PECVD Oxide, with the aim to reduce the compressive stress that this oxide layer releases once Silicon is removed from the backside. Large compressive stresses take place during the growth of thermal SiO_2 and they are large enough to cause plastic deformation of Si at growth temperatures [42]. As we will describe in Figure 4.8, when the Oxide is able to release this stress wrinkles and cracks can take place in the membrane, affecting the performance of the device. Due to this reason we decided to move to a different kind of Oxide.

2.4.2 PECVD OXIDE

Plasma-enhanced chemical vapor deposition (PECVD) silane-based oxide is being widely applied in the constructions of micro electromechanical system (MEMS) components where oxide films are used to for electrical or mechanical elements [43]. There are many mechanisms that may be responsible for the generation of intrinsic stress in the oxide films. Typical models include recrystallization, chemical reactions, incorporation of atoms, dislocation rearrangements, lattice mismatch, excess vacancy annihilation, grain-boundary relaxation and phase transformation. Even though also PECVD Oxide has a residual stress that strongly depends on the process parameters, its values, according to

the research from [42, 43] is one order of magnitude lower than the one of Thermal Oxide.

In fact, [42] evaluated a stress of 700 GPa for Thermal Oxide, a value definitely bigger compared to 150 MPa compressive stress obtained by [43] for the same range of temperature (about 950°C). Residual stress in PECVD Oxide is also thickness dependent; this relation is highlighted in Figure 2.13. Increasing the thickness of the oxide layer deposited on Silicon, also the compressive residual strain becomes higher. Adjusting the temperature at which this process takes place the stress can be further adjusted.

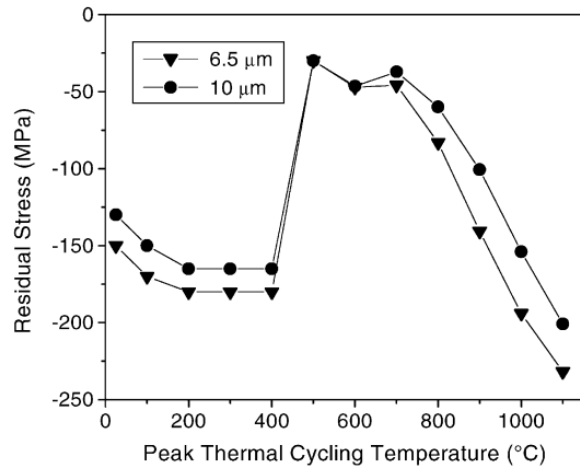


Figure 2.13 -The effect of peak thermal cycling temperature on the room temperature stress of silane-based PECVD oxide films [43]

2.5 STIFF ISLANDS

Functional stiff islands manufactured using traditional Silicon processing technologies played an important role in the realization of the stretchable MEA. Islands material, size, shape and thickness are important parameters deeply studied in the due course of this project. The geometrical parameters are going to be taken into account in the FEM paragraph and in the analysis of the results. In this chapter we will mostly focus on the materials that can contribute to islands' realization. These materials need to be compatible with clean room processing showing mechanical properties close to the ones of future components that are going to replace them in a ultimate working device.

MATERIAL	YOUNG'S MODULUS [GPa]	POISSON RATIO	DENSITY [Kg/m ³]	DETACHMENT LENGTH [mm]
SILICON NITRIDE	310 [44]	0.24 [45]	3270 [45]	5.06 [46]
POLY-SILICON	170 [47]	0.22 [47]	2330 [48]	5.04 [46]

Table 2.2 -Scoring card for two candidate island materials

Electrodes, analog-digital converters, amplifiers and multiplexer that can be implemented on a smart island are realized with traditional CMOS procedures, showing stiff properties. Furthermore these islands should remain attached on the elastomeric substrate even under stress condition, showing a good adhesion to PDMS. In the study of

[3] three different materials have been tested for making stiff islands embedded in PDMS: Silicon Nitride, Poly-Silicon and diamond-like carbon. This last material is not available in the clean room equipment; therefore we focused on the first ones. Main properties of these two materials are listed in Table 2.2. The higher stiffness of Silicon Nitride makes it more favorable candidate for stiff islands realization. In fact its Young's Modulus is twice the value of the Poly-Silicon's one; this last material is not stiff enough and cannot prevent cracking of additional device materials upon large deformation. Both these materials, according to the research from [46], show good and almost equal adhesion to PDMS substrate. The adhesion has been evaluated measuring the detachment length of a fixed-end cantilever beam showed in Figure 2.14.

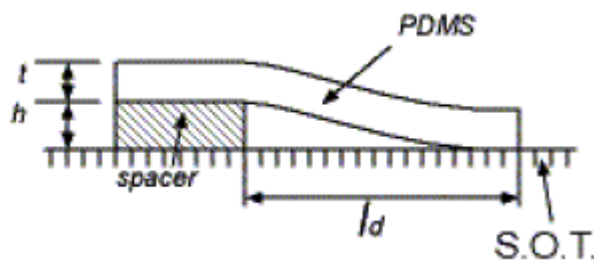


Figure 2.14 - Schematic diagram for measuring detachment length and adhesion energy of PDMS microstructures. The Surface Under Testing (S.O.T.) include single crystal silicon, thermally grown oxide, LPCDV Nitride, glass and PDMS [46]

As the PDMS material is transparent, it is simple to determine the detachment length by observing the interface directly under an optical microscope. Those two materials present the advantage of requiring similar fabrication processes. This point allowed us to test both of them during the development of our stretchable MEA.

2.5.1 SILICON NITRIDE

Silicon Nitride has a wide range of applications in microelectronics technology. It can be deposited on Silicon wafer by atmospheric-pressure chemical-vapor deposition (APCVD), low-pressure chemical-vapor deposition (LPCVD) and plasma-enhanced chemical-vapor deposition (PECVD), although the first of these is now rarely used [44]. The work we are here presenting concentrates on a LPCVD system. The gases used in LPCVD processes are usually dichlorosilane (SiH_2Cl_2 , DCS) or silane (SiH_4) as a source of silicon and ammonia (NH_3) as a source of nitrogen.

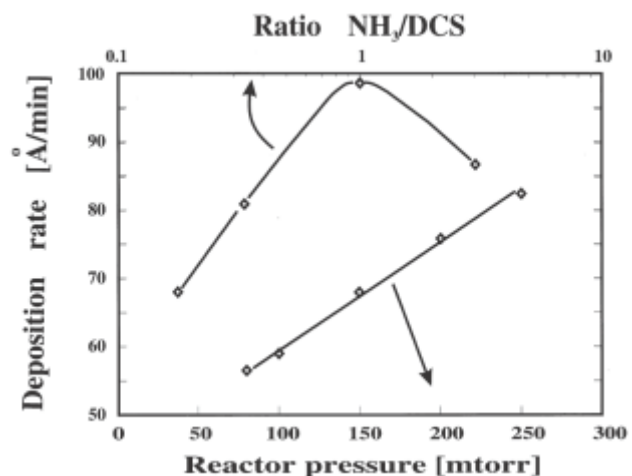


Figure 2.15 - Deposition rate as a function of gas-flow ratio for a temperature of 850°C and a pressure for a gas-flow ratio $\text{NH}_3/\text{SiH}_2\text{Cl}_2$ of 30/170 [44]

In some cases, for PECVD, N_2 is used instead of NH_3 to reduce the hydrogen content of deposited films [38]. In LPCVD and PECVD systems there are several factors that affect

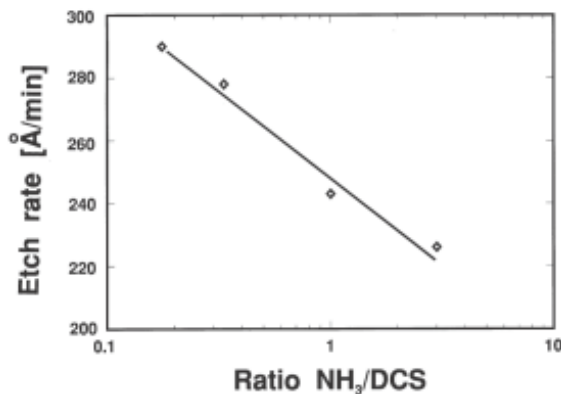


Figure 2.16 -Etch rate of silicon nitride in a parallel-plate plasma etcher as a function of process gas-flow ratio for a deposition temperature of 850°C and a pressure of 20 Pa. The plasma etching was performed using a gas composition of CHF 3 7.5 sccm and N_2 42.5 sccm, r.f. power (frequency 13.56 MHz) and gas pressure of 60 W ($52 \text{ mW}/\text{cm}^3$) and 5 Pa, respectively [44]

the film properties. For LPCVD these being the deposition temperature, the deposition pressure and gas flow (total and ratio). In the study from [44] the deposition rate of Silicon Nitride was found to be highly dependent upon both gas-flow ratio and reactor pressure and this is shown in Figure 2.15. The deposition pressure used for the gas-flow experiment was 20 Pa. As the NH_3/DCS ratio was increased the deposition rate also increased, reaching a peak at a ratio of one. This point represents the maximum

efficiency of gas use and a further increase in NH_3 resulted in a fall in deposition rate.

For many applications, as is for our project, the patterning of Silicon Nitride is performed using plasma etching techniques. A study of the etch rate according to the gas ratio has been performed by [44] and reported in Figure 2.16.

2.5.2 POLY-SILICON

Poly-Silicon is the most widely used structural material in current micro devices that are manufactured by surface micromachining [47]. The Poly-Silicon films in our work have been deposited by low pressure chemical vapor deposition (LPCVD). Furthermore it can be deposited plasma-enhanced chemical vapor deposition (PECVD), or solid-phase crystallization (SPC) of amorphous silicon in certain processing regimes. However these processes still require relatively high temperatures of at least 300°C .

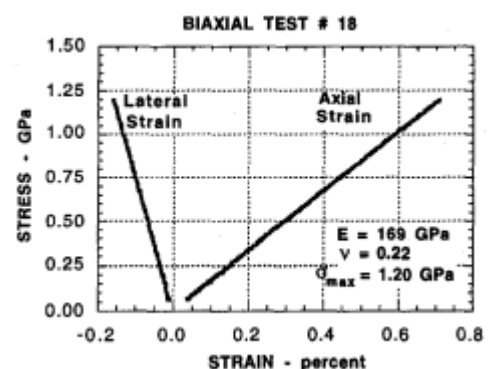


Figure 2.17 - A typical stress biaxial-strain plot [47]

Poly-Silicon deposition, or the process of depositing a layer of polycrystalline silicon on a semiconductor wafer, is achieved by pyrolyzing silane (SiH_4) at 580 °C to 650 °C; this pyrolysis process releases hydrogen. A research from [47] highlights the nature of Poly-Silicon as a brittle material with a linear stress-strain curve (Figure 2.17). As Silicon Nitride, also this material has been patterned with dry etching techniques during this work.

2.6 MICROFABRICATION FUNDAMENTALS

Microfabrication or micromachining in general refers to the design of a system with at least one dimension in micrometer range. Microsystem technology benefits from enormous technological and theoretical knowledge of microelectronics [49], as they share the same basic fabrication methodologies. Techniques such as photolithography are inspired from microelectronics, but other relatively new processes such as DRIE or LIGA processes are only dedicated to microsystems.

This paragraph, out of a wide variety of microfabrication techniques, concludes only a few principles that have been used during the due course of this project.

2.6.1 PHOTOLITHOGRAPHY

Photolithography is one of the most critical steps in microelectronics and microsystems fabrication as it determines the accuracy of forthcoming processes. Using lithography, structures with critical dimensions in sub-micron range can be transferred onto the substrate using a mask [49]. One of the main advantages of photolithography is its parallel production, i.e. many systems with similar or different parameters can be processed simultaneously on a single wafer. Another advantage is its ability of mass production, where replicas of a pre-designed structure can be transferred on many wafers without any loss of fidelity. Photolithography is a sequence of individual small steps which are summarized as follows.

2.6.2 MASK DESIGN

A photolithographic mask is a glass slab with chromium patterns providing opaque areas. Glass can be a soda lime glass or quartz [50], but they are generally very expensive. A cost effective solution can be a foil mask (transparency). Foil masks on the other hand have problems with cleaning and temperature dependent behavior. This problem can be overcome by transferring the mask pattern from foil to a glass slab coated with chromium and photoresist (as in our case). After developing and etching a new mask is formed; cleaning and handling of which is just like any glass mask.

The mask is mostly designed with the software as Cadence, CleWin and CAD; we will discuss this point in the Mask design paragraph. Alignment can be achieved by alignment marks. Alignment marks are patterns in a mask specifically designed to align masks to each other. Alignment marks must

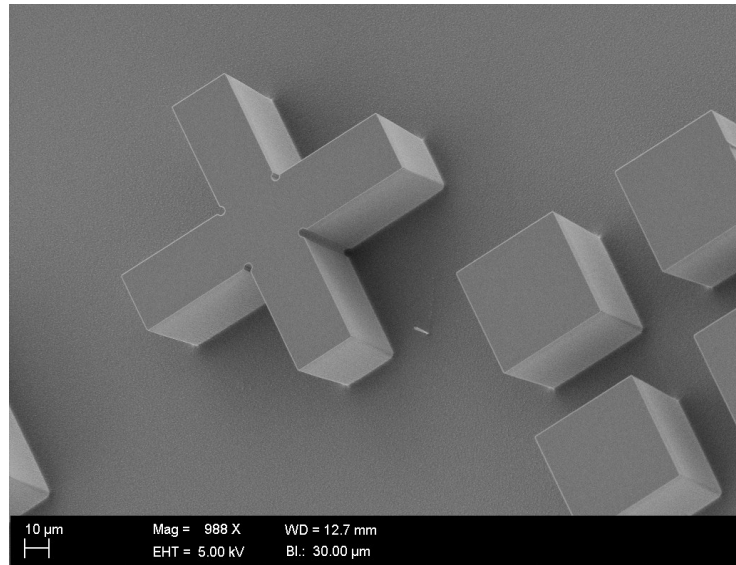


Figure 2.18 - Angular view of alignment marks etched in Si (SEM micrograph)

confirm to the properties such as they must be easy to use, easy to find, hard to misinterpret and most importantly they should not be destroyed by processing prior to alignment [50]. The smallest dimension of an alignment mark should be smaller than the smallest dimension of actual design to confirm to the accuracy of alignment. An effective example of an alignment has been demonstrated in Figure 2.18.

2.6.3 SPIN-COATING

In order to transfer the desired pattern on a wafer surface it is first covered with a thin layer of an organic photosensitive polymer, also known as photoresist (photosensitive means that the chemical properties of the polymer are changed on interaction with light). This process is known as spin-coating. Wafer is first placed on a rotatable chuck and vacuum is used to hold the wafer in place during the spinning process [49]. With the help of the pipette a small amount of resist is dropped onto the center of the circular wafer and is then brought into rotation with a high circular velocity. Nominal spinning speed varies between 1500-8000 rpm depending upon viscosity and desired thickness of the resist [51]. An even coating of resist across the whole wafer surface is ensured as a result of centrifugal force. In MEMS design the thickness of the resist can vary from a few microns to as high as 100 μm [49].

Thickness, T , of resist depends on the intrinsic viscosity, η , of fluid and rotation speed, ω , of the chuck and is given by [51].

$$T \propto \frac{KC\eta}{\omega}$$

Where K is overall calibration constant and C is polymer concentration in g/ml solution.

In some cases the adhesion of resist to the substrate surface is poor so that it is not sufficient for the further steps which may involve heating or immersion in a fluid. A possible solution is to spin first a material that can enhance the adhesion. An example to this is Ti-primer which can be used to enhance adhesion between photoresists and silicon substrate.

2.6.4 SOFT BAKING

The process that immediately follows resist spinning is baking, also called soft baking, where the wafer is heated to a temperature as high as 100°C for a few minutes to improve the adhesion of resist to the wafer, remove solvents and to remove the built-in stresses [51].

2.6.5 EXPOSURE

Once the substrate is coated with photosensitive film, next step is to transfer the desired geometry on the resist layer. This can be done by selectively exposing areas to the UV light with the help of a mask. Lithography can be categorized into three types namely contact printing, proximity printing and projection printing. Contact printing allows the mask to even touch the photoresist layer [52]. The resolution, R , is determined by the wavelength, λ , of the UV light and the thickness, z , of the resist. Mathematically it can be given as [51]:

$$R = b_{min} = \frac{3}{2} \sqrt{\frac{\lambda z}{2}}$$

Positive & Negative Photoresist

A positive or negative photoresist can be differentiated depending upon whether the exposed or un-exposed region is dissolved. For a positive resist exposed regions are dissolved but they remain insoluble for a negative resist. Solubility of the positive resist is attributed to the fact that there is a chain scission on interaction with UV light [51]. On the other hand, negative resists become insoluble as a result of photo-induced polymerization or cross linkage on exposure [49]. A typical profile as a result of development for both positive and negative photoresists is shown in Figure 2.19.

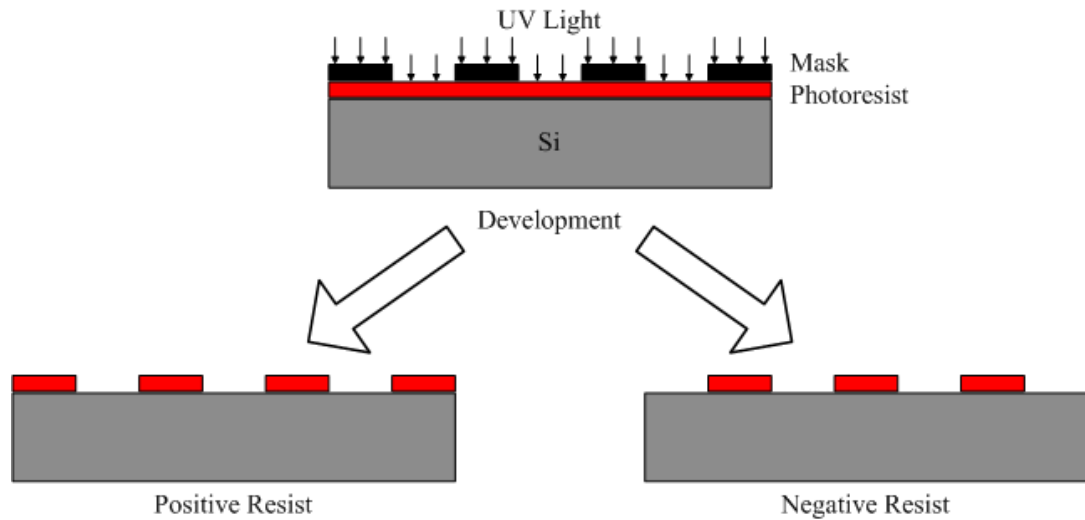


Figure 2.19 -Persists of positive and negative photoresists after development

2.6.6 DEVELOPING

Developing is the process of selective removal of photoresist. Developing of positive resists is carried out in a solution of alkaline salts i.e. NaOH or KOH with low concentrations. Usually concentrations of 0.5% – 1.0% are used. The solution is usually maintained at room temperature i.e. 25°C. Nominal developing times vary from a few seconds to a couple of minutes depending upon the thickness and chemical nature of the resist. Xylene is an example of negative photoresist developer [51].

After development the desired geometry is patterned onto the resist layer which will now serve as a mask for layers underneath during the subsequent additive or subtractive processes [51].

A very important successor after developing step is rinsing of the wafer with plenty of water to avoid the over dose of developer.

2.6.7 POSTBAKING

Post baking is carried out optionally after the developing in order to enhance the adhesion of resist to the wafer surface which might have damped during the developing. It also serves to harden the resist which increases its resistance to the etching process followed immediately after.

2.6.8 RESIST STRIPPING

Once the desired addition or subtraction step has been carried out, the resist can be removed. It is known as resist stripping.

Wet Stripping

Mostly resists are soluble in solvent like acetone and iso-propanol. The wafer is first dipped into acetone and then into iso-propanol, for a few minutes, to take away the resist. During the dips ultrasonic bath can be used depending upon the mechanical stability of structures on the wafer. After the two dips the wafer must immediately go into water and rinsed for a few minutes.

Dry Stripping

Barrel asher also finds its application in photoresist stripping. Sample is placed on a quartz carrier. Oxygen plasma is used during this process. First the dissociation of molecular oxygen (O_2) to atomic oxygen (O) is carried out [50]. These relatively more reactive oxygen ions then react with the polymers forming carbon monoxide, carbon dioxide and steam.

The process is referred to ashing instead of etching because etching is selective removal of materials while ashing on the other hand removes the polymers and organic layers. For the same reason barrel ashing can also be used for descumming [51].

2.6.9 ETCHING

Etching in microfabrication refers to the process of selective removal of material layers. The basic idea is to transfer the resist pattern onto the wafer surface. Depending upon the etching scheme the outcomes of the etching process can be determined. Etching can be generally divided into wet and dry etching techniques.

Etching results in either isotropic or an-isotropic profile. Isotropy employs the same ratio of etching in all crystal orientations; thus it is a source of under-etch. An-isotropy means less or no etching in one or more crystallographic orientation; thus it is used for structures with high aspect ratios. Both isotropic and an-isotropic profiles are depicted in the Figure 2.20.

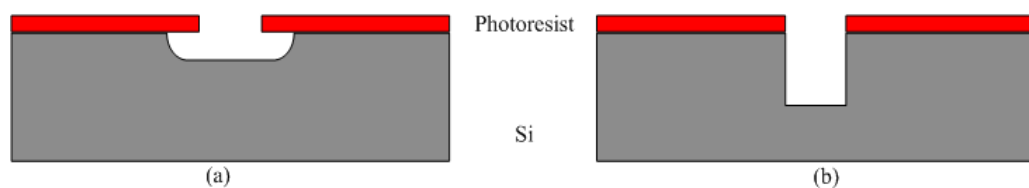


Figure 2.20-Etch profiles (a) isotropic etch profile (b) absolute an-isotropic etch profile

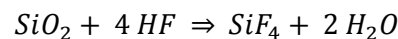
Out of a wide variety of dry and wet etching methods only the ones that have been used during the due course of this project will be presented.

2.6.10 WET CHEMICAL ETCHING

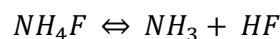
Wet chemical etching is probably one of the simplest forms of etching where the substrate is immersed into an etchant bath.

Buffer Oxide Etch

Buffered oxide etch (BOE) is used to remove Silicon Oxide. BOE is a very selective etch, meaning that it stops at the silicon and does not etch further. The etch may be used in many steps, such as exposing the active region near the beginning of a process or defining contact holes at the end. BOE consists of Hydrofluoric Acid (HF) at high concentration level (about 10 times greater than the oxide strip in the RCA clean). HF is very dangerous and HF burns are particularly hazardous. An insidious aspect of HF burns is that there may not be any discomfort until long after exposure. The overall reaction for etching Silicon Oxide with BOE is the following:



Where a buffering agent, ammonium fluoride (NH_4F), is added to maintain HF concentration and to control pH minimizing photoresist attack. The buffering reaction is the following:



The etch rate of BOE is about 1000 Å/min. The time in the BOE bath is calculated accordingly.

PES Etch

PES etchant is used to etch Aluminum. It is a mixture of phosphoric acid, nitric acid, acetic acid and water. The solution is heated to 40 °C. Etch rate for Aluminum is 100 nm per min. Oxide or silicon can be used as an etch stop layers. The etching procedure is followed by rinsing (Quick Dump Rinse) and a drying step.

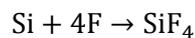
2.6.11 REACTIVE ION ETCHING

Reactive Ion Etching (RIE) is a dry etching technique which uses both physical and chemical effects to remove the material. It uses chemically reactive plasma, generated electromagnetically under low pressure, to knock out the bits. The plasma is generated in the same chamber where wafer is placed.

A typical setup for RIE consists of a cylindrical vacuum chamber. The wafer is placed on the grounded bottom electrode. The situation where the wafer is placed on the cathode is referred to as reactive ion etching or reactive sputter etching [51]. Gas inlets are on top while the exits are located at the bottom. SF₆ is generally used for the etching of poly-silicon as sulfur atoms are heavy enough to remove the material physically [50].

Initiation of plasma is carried out with a strong RF field, typically 13.56 MHz, to the wafer electrode. The strong oscillating field ionizes the gas molecules by ripping apart electrons and the ionized atom. Capacitors are used to match the impedance of power supply and plasma for maximum efficiency [50]. Due to the oscillating electric field the electrons move from top to the bottom of the chamber and then back to the top faster as compared to heavy ions. During this motion there are fair chances that the electrons get absorbed by the wafer carrying electrode thus creating a net negative charge on the plate. As a result the plasma itself develops positive charge as it is left with higher concentrations of positive ions. This phenomenon results in a net voltage difference between the plasma and wafer electrode and positive ions tends to accelerate towards the wafer electrode and where they collide with the whole electrode plate including the material to be as etched away thus knocking it out.

During plasma etching chemical effects can occur when some of the gas radicals react with the substrate surface, forming volatile compounds. Following six steps takes place during a chemical etching namely, generation of etchant species, diffusion to the surface, adsorption, chemical reaction and finally desorption [50]. SF₆ reacts with silicon resulting in SiF₄ which is a volatile product. Chemical reaction is given by [50]:



Chemical effects dominate when the process is carried out at high pressures and vice versa. Chemical etch generates an isotropic profile, while physical etch generates a side wall angle fairly close to 90°. RIE cannot be used to produce very deep structures because the top region of side walls is exposed to etchants all the time which can result in a funnel like structure. Combined etch rate is sum of chemical and physical effects and thus depends upon nature of gas mixture, flow rate, pressure and temperature inside chamber and RF power.

When compared to wet chemical etching, RIE has higher anisotropy, better uniformity and control, and better selectivity [53].

2.6.12 DEEP REACTIVE ION ETCHING

Reactive ion etching cannot be used for generating high aspect ratio systems because the top of side wall is exposed more to etchants as compared to the bottom of the deep structures thus resulting in a wedge shape profile. So a solution must be found to this problem. Two main approaches introduced to overcome this situation are Bosch process and cryogenic process [50]. Focus here is on the Bosch process.

The Bosch process also named as Deep Reactive Ion Etch (DRIE) or Advanced Silicon Etch (ASE) is probably one of the most important and frequently used etching technique in microfabrication. The crux of the Bosch process lies in the alternative etching and passivation cycles. The etching is carried with SF_6 while C_4F_8 is used for passivation. Cycle time usually varies from 5-30 sec [50].

Passivation is done in order to prevent the sidewalls from chemical etching, while the bottom of the trench is open to physical etch resulting in nearly vertical side walls.

DRIE uses an inductively coupled plasma (ICP) to create a magnetic envelop inside the etch chamber, thus minimizes the loss of charged species to the surroundings and helps to achieve and maintain a higher plasma density [50].

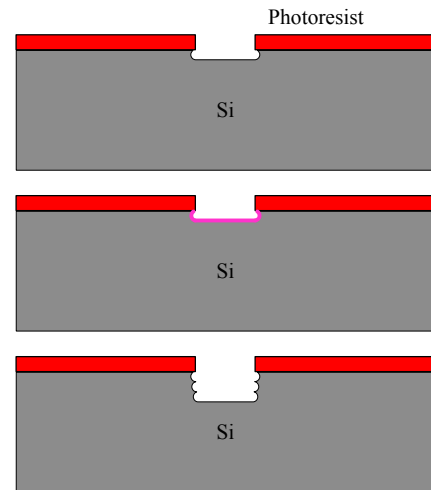


Figure 2.21 - etch (black) and passivation (pink) steps of DRIE

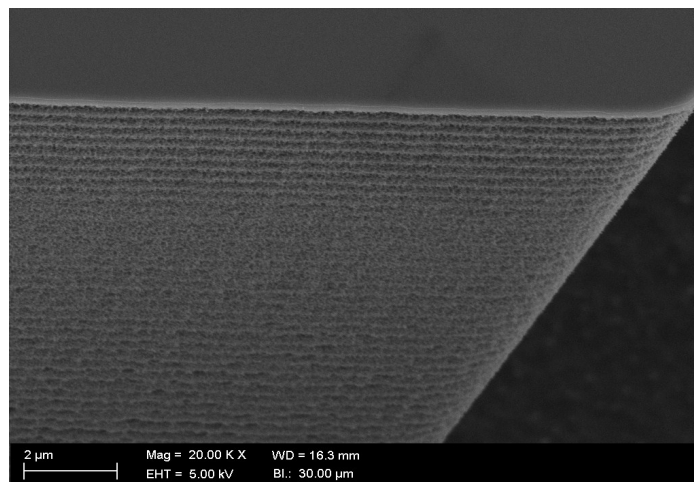


Figure 2.22 - Typical profile of deep reactive ion etching (SEM micrograph). Each ripple shows one complete cycle (etching and passivation)

An ideal profile for DRIE has been shown in Figure 2.20-b. Sidewalls should be smooth and vertical, while the bottom of the trench has to be smooth and flat. The real profile on the other hand looks like Figure 2.21 i.e. the sidewall is scalloped shaped, the size of which depends upon the cycle time. The pink layer inside the etch trench shows Teflon passivation layer. A typical high aspect ratio system as a result of deep reactive ion etching has been shown in Figure 2.22.

3. COMPLEMENTARY EXPERIMENTS

In order to run the fabrication process and collect results from the devices produced, some procedures were required. This chapter describes the technology around the fabrication process. Patterning the chips through photo lithography requires the design of a set of masks able to reproduce on the silicon wafer several combinations of islands integrated in the substrate, varying parameters such as the islands' dimension, distance and shape. The possibility to compare the results obtained in the laboratory with theoretical simulations can be achieved thanks to the Finite Element Method (FEM); these simulations, performed with COMSOL Multiphysics, gave us important evidences, orienting the improvements of the project as in the case of the anti-delamination shields. The necessity to test different configurations and collect results from experimental trials requires a background theory about bulge test and the realization of a device able to stress the chips, giving us the desired results.

3.1 MASK DESIGN

As previously discussed in the paragraph about Microfabrication fundamentals, a mask is necessary to pattern the chips. In our case both topside and backside masks were necessary. Two different topside masks allowed the patterning of the islands, whereas the backside mask allowed the creation of the holes inside the silicon layer in order to leave the stretchable membranes free to be inflated. A fourth mask became necessary in the development of the project in order to avoid the delamination of the islands from the surrounding substrate we noticed after the first results.

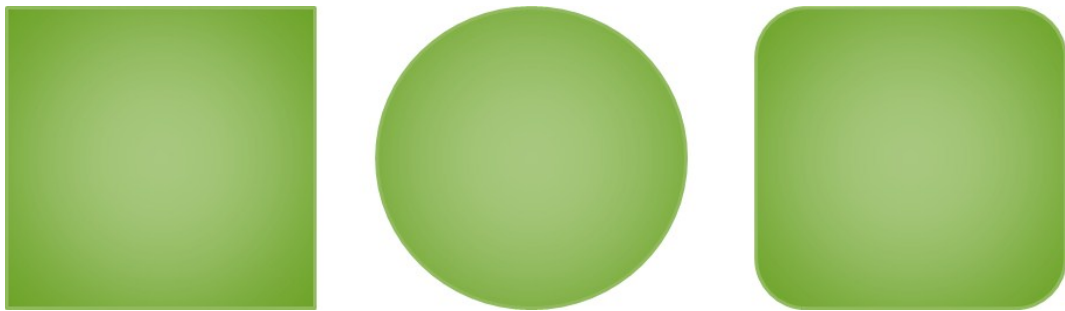


Figure 3.1 : Three different island shapes have been tested, varying their dimensions and the distance between them

In order to investigate the influence of the geometry on the cracking behavior of the stiff islands under inflation, three different geometrical parameters have been examined: the shape of the islands, their dimensions and the inter-island space.

As showed in Figure 3.1, three different shapes have been studied: square, circle and rounded square. In the first set of experiments three different island dimensions have been tested: small islands configuration with 50 μm size, 100 μm medium islands and 200 μm large islands. As the strain in the membrane is also influenced by the density of stiff material in the cross-section, three different interisland spaces of 50 μm , 100 μm and 200 μm have been investigated.

In order to reproduce all the possible combinations of those three parameters on different chips, 27 different configurations were required. Each chip was designed to be a square of 1 cm length (Figure 3.2 A); using 6 inch wafer each combination can be placed at least four times in different positions of the same wafer surface. After the first results we decide to test also more severe conditions, increasing the amount of stiff material in the membrane cross section. A second topside mask was designed with 200 μm and 300 μm islands size and 25 μm , 50 μm , 75 μm and 100 μm interisland spaces. A fourth mask was projected in order to avoid islands delamination from the substrate (Figure 3.2 B); the principle of this mask will be discussed in the next chapters.

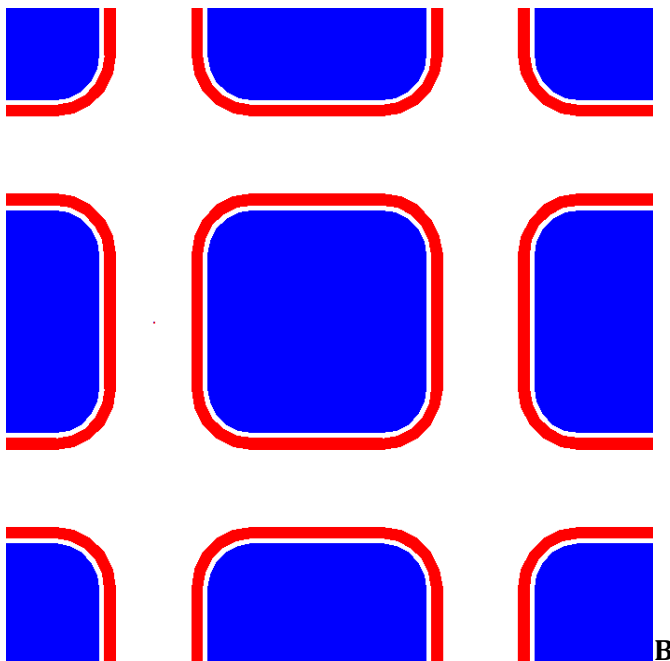
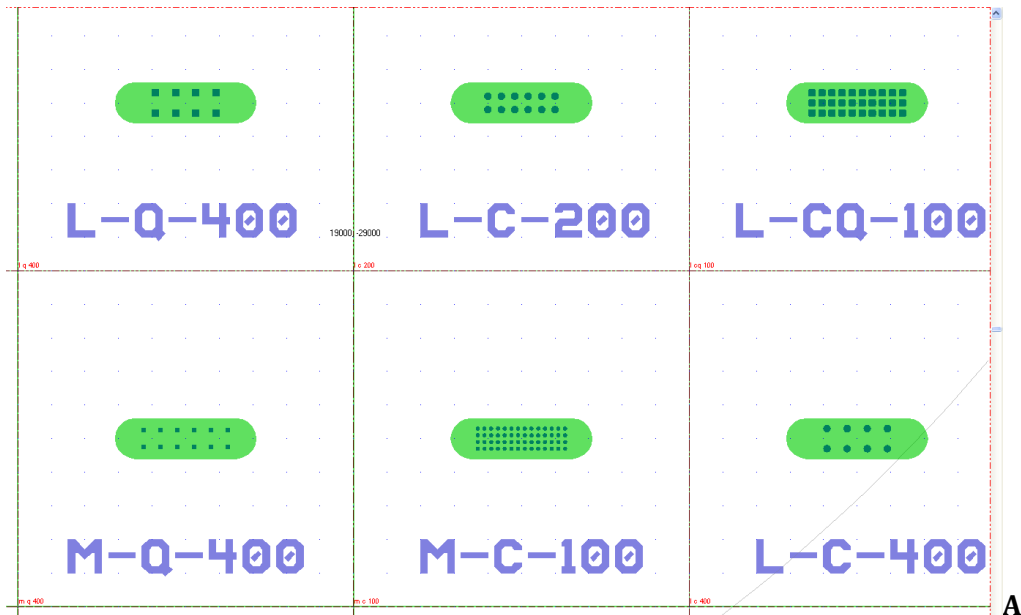


Figure 3.2 - Snapshot from Cadence. A) a view of some chips. The grey line around them fix the borders of each chip (1 cm x 1 cm) for the backside mask, Light green shape in the center of each chip represent the hole and dark green structures inside the hole are the islands of the first topside mask. Also a code allows us to distinguish the chip during the microscope inspection. The first part indicates the dimension of the island (S for 50 μm , M for 100 μm , L for 200 μm and XL for 300 μm islands). The second part indicates the shape of the island (C for circle, Q for square and CQ for rounded square). The last number indicates the interisland space (in μm). B) a detailed view of some islands (blue) surrounded by the anti-delamination shield (red)

The dimension of the holes (light green structures in Figure 3.2 A) in the backside mask was chosen re-elaborating the dog-bone shape adopted by [1]. We opted for rounded extremities in place of straight lines both to avoid the delamination of the membrane, from the Silicon substrate that surrounds it, during the inflation and to have no sharp corners that would have been hard to reach by the surfactant during wet etching treatments.

The mask design was carried out in CleWin under Windows and Cadence under UNIX operative system.

3.2 FEM MECHANICAL SIMULATION

In order to assess the behavior of the elastomeric membrane, simulations based on the Finite Element Method have been performed. These simulations have a double functionality: on the one hand they allowed us to have a reference, comparing the experimental results we got in the laboratory with the outcome of the simulations. On the other hand they were able to give explanations to particular phenomenon that took place in the membrane, suggesting us practical ways to improve the behavior of our device, as in the case of the anti-delamination shield we introduced after the first set of experimental results.

The finite element method (FEM) is a numerical technique for finding approximate solutions of partial differential equations (PDE) as well as integral equations. The solution approach is based either on eliminating the differential equation completely (steady state problems), or rendering the PDE into an approximating system of ordinary differential equations, which are then numerically integrated using standard techniques such as Euler's method, Runge-Kutta, etc. In solving partial differential equations, the primary challenge is to create an equation that approximates the equation to be studied, but is numerically stable, meaning that errors in the input and intermediate calculations do not accumulate and cause the resulting output to be meaningless. There are many ways of doing this, all with advantages and disadvantages. The finite element method is a good choice for solving partial differential equations over complicated domains, when the domain changes (as during a solid state reaction with a moving boundary), when the desired precision varies over the entire domain, or when the solution lacks smoothness [54].

For this study the problem has been solved using COMSOL Multiphysics version 4.2. This method is computationally expensive and requires a converging solution to have the possibility to get reliable results. Hence, unnecessary complexity should be avoided and the size of the problem should be as small as possible. The purpose of these simulations is not to model a structure that exactly matches our PDMS membrane in all its features. It is quite obvious that the computational power of the system will not be enough to give us results. However simple structures that represent particular aspects of our membrane can be analyzed giving us interesting outcomes.

3.2.1 MEMBRANE INFLATION

In our first simulation we successfully studied the behavior of a membrane with one island in its center (Figure 3.3). The first issue we had to face using COMSOL was to

define a geometry for the problem. We created a 100 μm thick block with a rectangular surface of 1 mm width and 0.5 mm depth. In the center a 100 nm thick rounded square island has been placed on the top of the membrane. Its size is 100 μm .

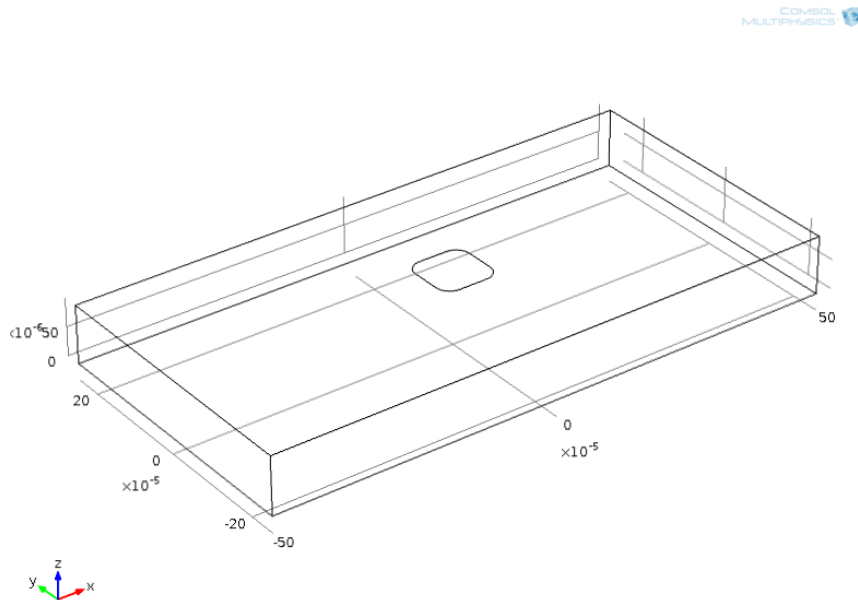


Figure 3.3 - The one-island membrane that has been inflated in the first simulation

The second step was to define the properties of the materials involved. We assigned PDMS to the elastomeric membrane and Silicon Nitride to the stiff island. Their properties are listed in Table 3.1.

	YOUNG'S MODULUS [MPa]	POISSON'S RATIO	DENSITY [Kg/m ³]
SUBSTRATE	1.2 [16]	0.47 [16]	1050 [55]
ISLAND	$310 \cdot 10^3$ [44]	0.24 [45]	3270 [45]

Table 3.1 - Mechanical properties of the element involved in the simulations. The substrate is made by PDMS and the island is made by Silicon Nitride

Once we defined the geometry and the mechanical properties of its components, it is necessary to characterize to load we want to apply on this structure. We started assigning the fixed constrains, or rather the surfaces or edges that are fixed and not free to move. All the four lateral surfaces of the membrane have been set as fixed constrains, simulating the real device in which none of them is free to move. Than a boundary load, in form of a pressure of 70 KPa, has been applied on the backside of the membrane; its purpose is to inflate the elastomeric substrate, as we did in practice on the chips we fabricated. Therefore just the topside of the membrane remained free from load and constrains, as in the real device.

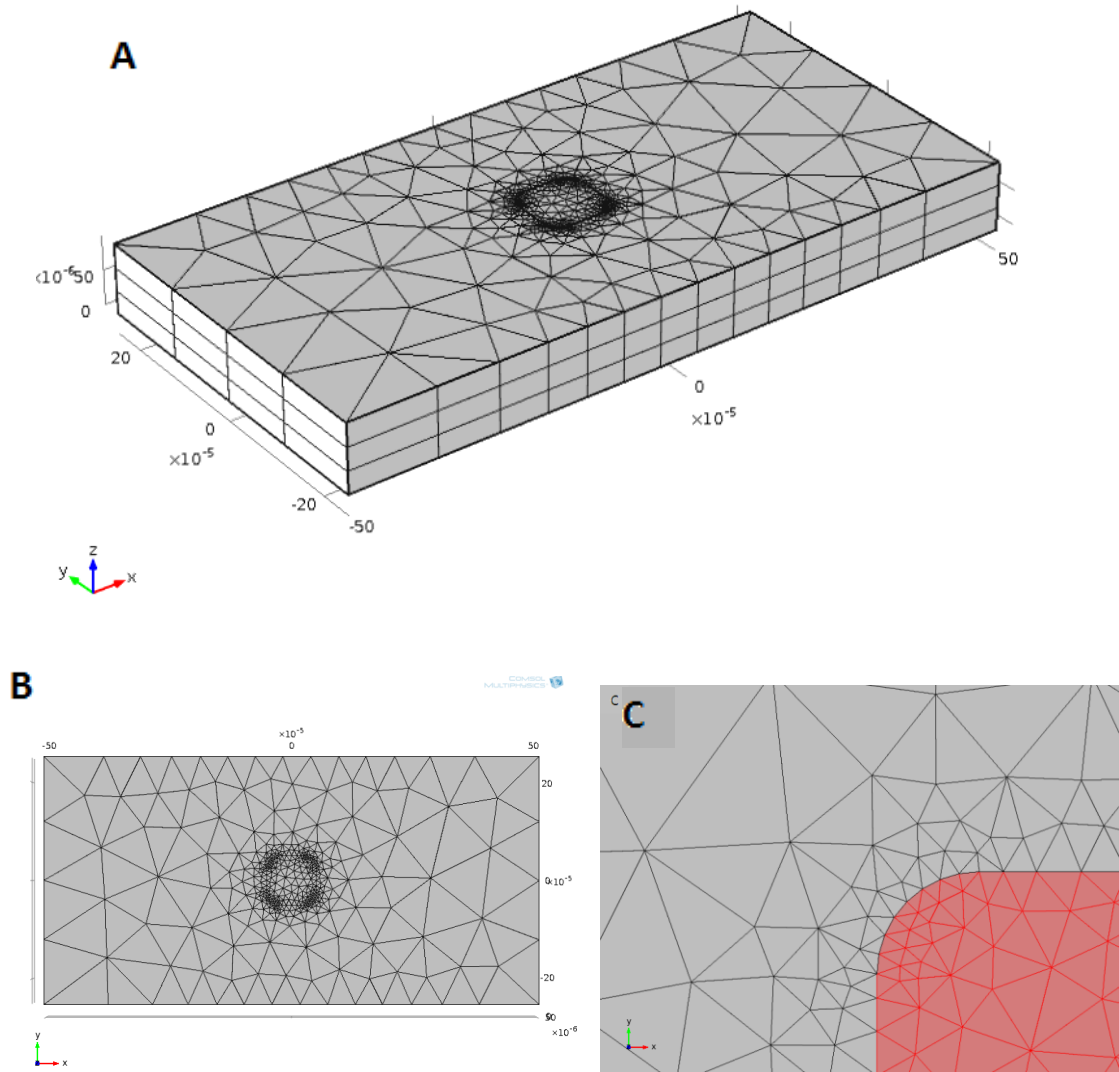


Figure 3.4 - User defined mesh. A) The overall mesh is presented in the 3D structure. As explained before, we defined the mesh on the top surface and swept it through the whole thickness of the membrane. **B)** Top view of the mesh. In the corners of the island the elements become smaller and the accuracy higher. **C)** A detail of the corner, the island is highlighted in red

A delicate aspect is represented by the meshing of the device that consists into discretizing the space into small elements. The solution of the FEM is going to be computed at the vertices of those elements. If the elements of the mesh are small the solution will be accurate, however the total number of elements will increase the complexity of the problem, requiring longer time to compute a solution and even increasing the risk that the simulation fails, without converging to a result [19]. The mesh can be adjusted manually as needed; for example there is the need of a coarser mesh in areas in which higher strains are expected; in our case this happen in the regions between the island and the membrane. Also the corners of the island need denser mesh. However perfect corners (matching between two straight lines) are

singularity points, in which some property, such as differentiability, cannot be defined. This leads to discontinuities which will cause the method to generate inaccurate results. To avoid this problem straight corners have been replaced with small size-filled ones. Defining manually a mesh we created the elements on the top surface and then we swept them through the whole thickness of the membrane. The highest accuracy has been put in the rounded corners of the islands. Several views of the mesh are reported in Figure 3.4.

Results

The problem has 40257 degrees of freedom. Normal time of computation, on a mainframe computer, is in the range of minutes. The solution converged as showed in following Figure 3.5 and Figure 3.6. We mainly studied the strain in order to predict ruptures and scratch in the device. Higher strain increases the possibility that cracks took place. The strain is a vector; therefore it can be described with three components orthogonal to each other (Figure 3.5 A and Figure 3.6 A-B). The simulation also revealed the strain concentration in the substrate near the island edges. In agreement with the study from [3], while the strain in the island edge remain insignificant, the surrounding substrate may stretch by several tens of percent to accommodate the overall elongation (Figure 3.6 D). Three-dimensional stresses and strains build up in many directions. A common way to express these multidirectional stresses is to summarize them into an equivalent stress, also known as the Von Mises stress [19]. The study of this value allowed us to analyze what happen inside the island (Figure 3.6 C). If on the one hand the strain is almost equivalent to zero all over the island, the distribution of the Von Mises stress showed the weaknesses of this stiff structure.

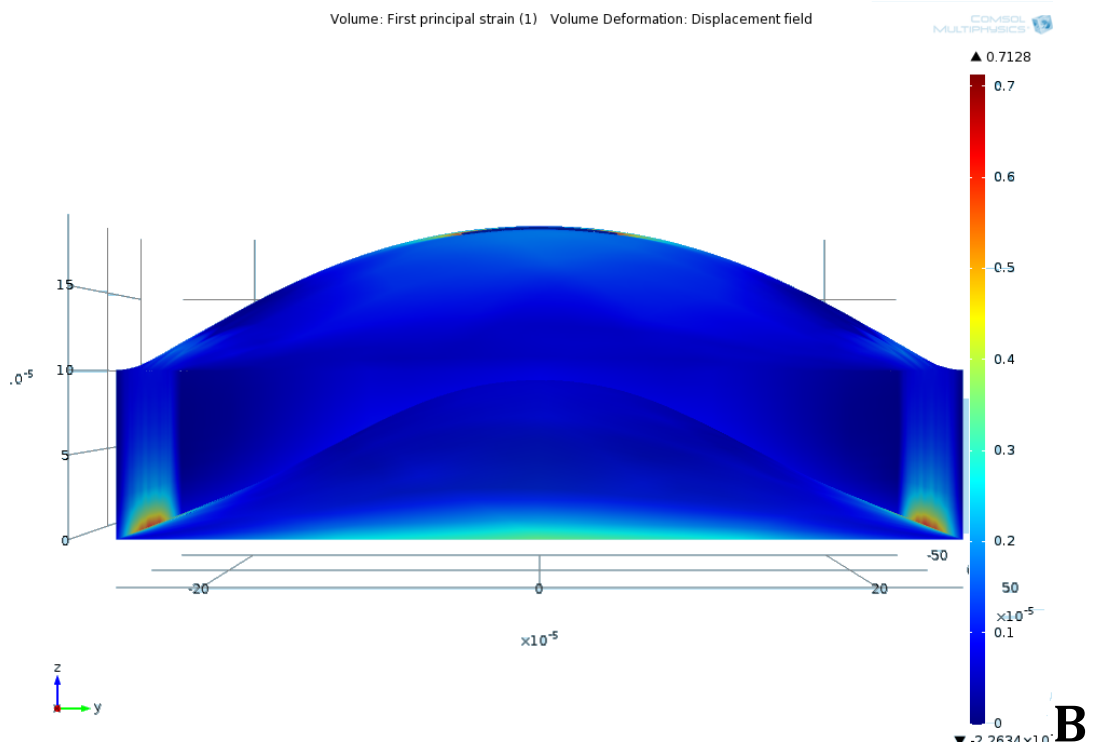
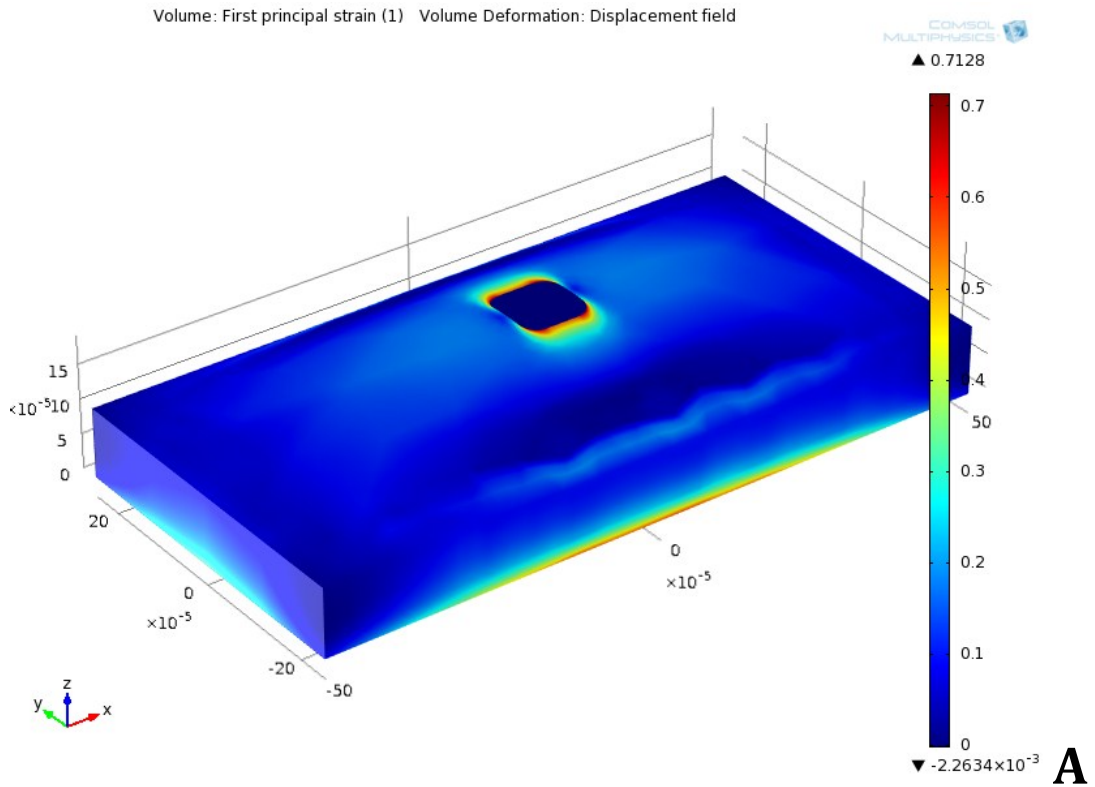
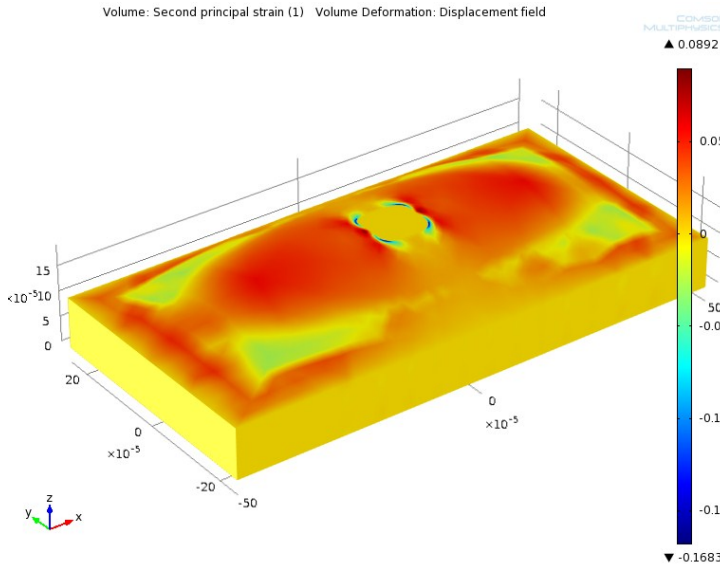
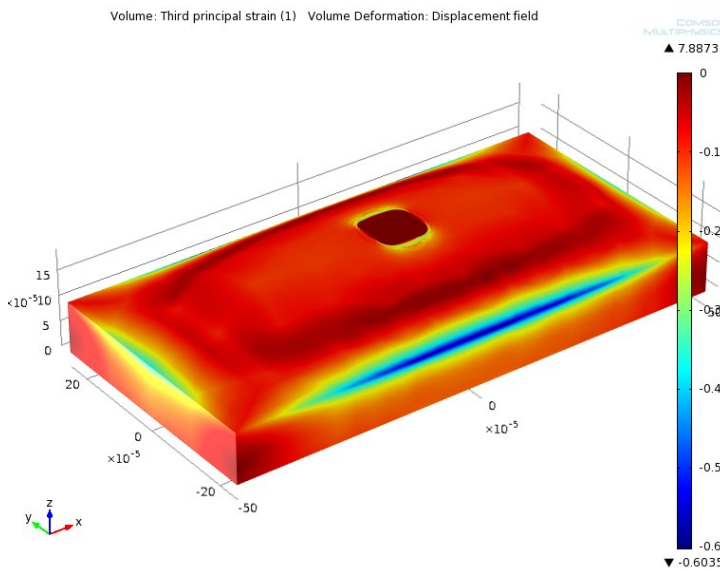


Figure 3.5 - First principal strain in the membrane inflated from the backside with a 70 KPa pressure. A) A three-dimensional view of the device. As expected the higher strain are in the region surrounding the stiff island along the y axis. B) The frontal view of the membrane. We can see the shape of the substrate once the pressure is applied. Higher strain is also at the bottom sides of the membrane, possible cause of delamination of the substrate from the surrounding



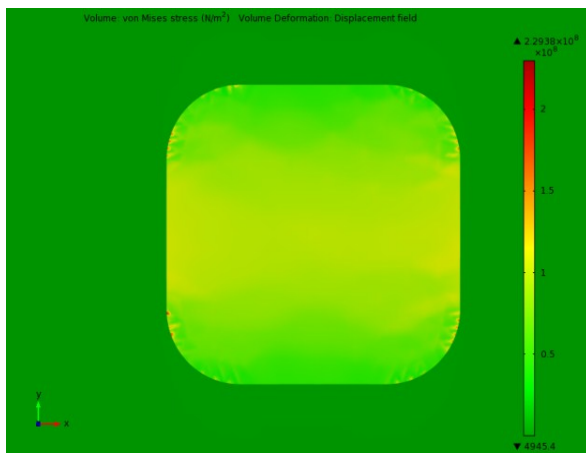
A



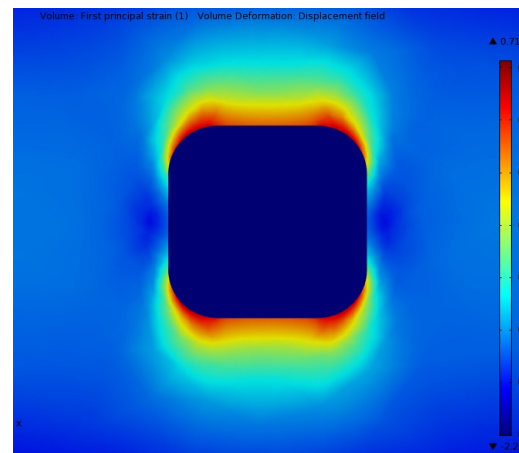
B

Figure 3.6 - A view on the second (A) and third (B) principal strain. Strain is a vector that can be completely described with three orthogonal components. However, as we can see in these pictures, the values of these two components are really lower compared to the first one. In a first approximation we can consider just the first principal strain showed in Figure 3.5 to study the behavior of the membrane.

C) A view of the Von Mises stress to investigate what happen inside the island. Along the edges some portions reach the higher strain, therefore we expect that in real inflation test these regions will be the ones in which cracks first take place. D) The two region of the membrane attached to the island along the y axis are the one that show the higher strain. This will be translated, in the real case, in a delamination of the membrane from the island.



C



D

3.2.2 EFFECTS OF ISLAND'S SHAPE AND DIMENSIONS

An interesting study about island parameters has been conducted by [19]. Despite the experimental setup is different to the one used in this project, same materials and similar dimensions were involved, allowing us to get interesting observation from the results achieved. The way in which both the shape of the island and its dimension affect the maximum strain in the membrane has been analyzed. The load applied is a unidirectional stretch of the elastomeric substrate. Starting from a square island and increasing step by step the ray of the corner we can obtain a shape that become a circle once the ray reaches the half of the side length. Parametrical COMSOL simulations have been performed, retrieving the maximal strain of the membrane in function of the ray of the corner. Results are shown in Figure 3.7.

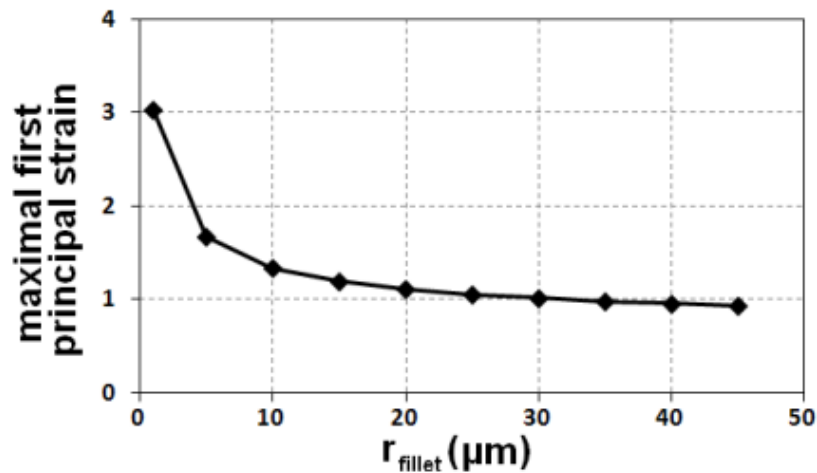


Figure 3.7 - First principal strain in the proximity of the round island. Physical deformation is included in these plots [19]

As expected, circle shape islands imply a lower peak-strain in the surrounding membrane compared to one of the square islands. However a squared surface is bigger than the one of a circle inscribed in its center; moreover bigger surfaces allow us to place more circuitry on the same island. From the peak strain point of view a good compromise seems to be represented by intermediate solutions. The biggest drop in the membrane strain is obtained for smaller rays, meaning that a rounded square island would provide a good compromise between the amount of circuitry that can be placed on it (the total surface) and the stress in the surrounding substrate. Practical experiments, discussed in the conclusion, will show interesting phenomenon related to this aspect.

In the second study the maximal strain has been related both to the dimension and to the shape of the island. As we can see in Figure 3.8 bigger islands means higher strain in

the surrounding. As it will be explained in details in the paragraph about the Bulge Test, more stiff material in the cross section requires the same amount of deformation to a reduced amount of PDMS (the island is stiff for hypothesis and does almost not deform). Therefore the strain in the PDMS will be higher in relative terms.

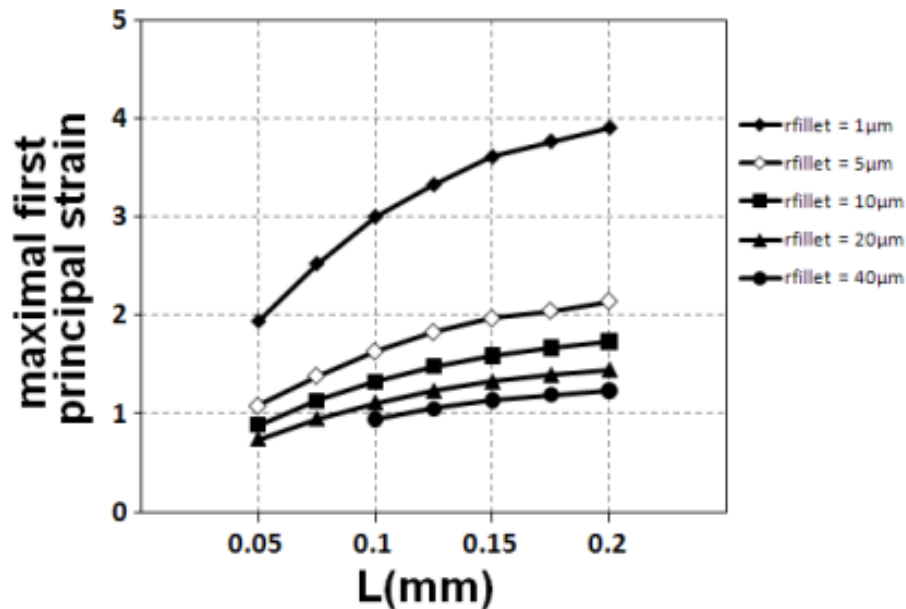


Figure 3.8 - First principal strain in the proximity of the round island for different island shapes (r_{fillet}) varying the island size L. Physical deformation is included in these plots [19]

3.2.3 ANTI-DELAMINATION SHIELD

As we have noticed studying the strain in the inflated membrane, the highest deformations are required to the elastomeric substrate in the regions surrounding the island along the y axis. As we can see in Figure 3.9 this strain creates a valley in the PDMS region next to the stiff islands. This delamination we observed turns into a problem when it causes the islands to detach from the substrate in which they are embedded. Also for future developments, when interconnections will take place among the islands, delamination can turn in an obstacle. In fact, for a future MEA, not only electrodes that will collect signals but also wires are required. These interconnections can transfer for example signals to other components inside the device (such as multiplexer or amplifier) or outside the device itself for further elaborations. If these wires are connected to an island and this island start to delaminate from its substrate, the interconnection can detach or even break. In light of this, we studied an approach able to reduce this phenomenon. A simple solution can be represented by the creation of an indentation in the membrane that redistributes the strain, decreasing the one in the regions close to the islands. In order to prove this theory, COMSOL simulations have been performed.

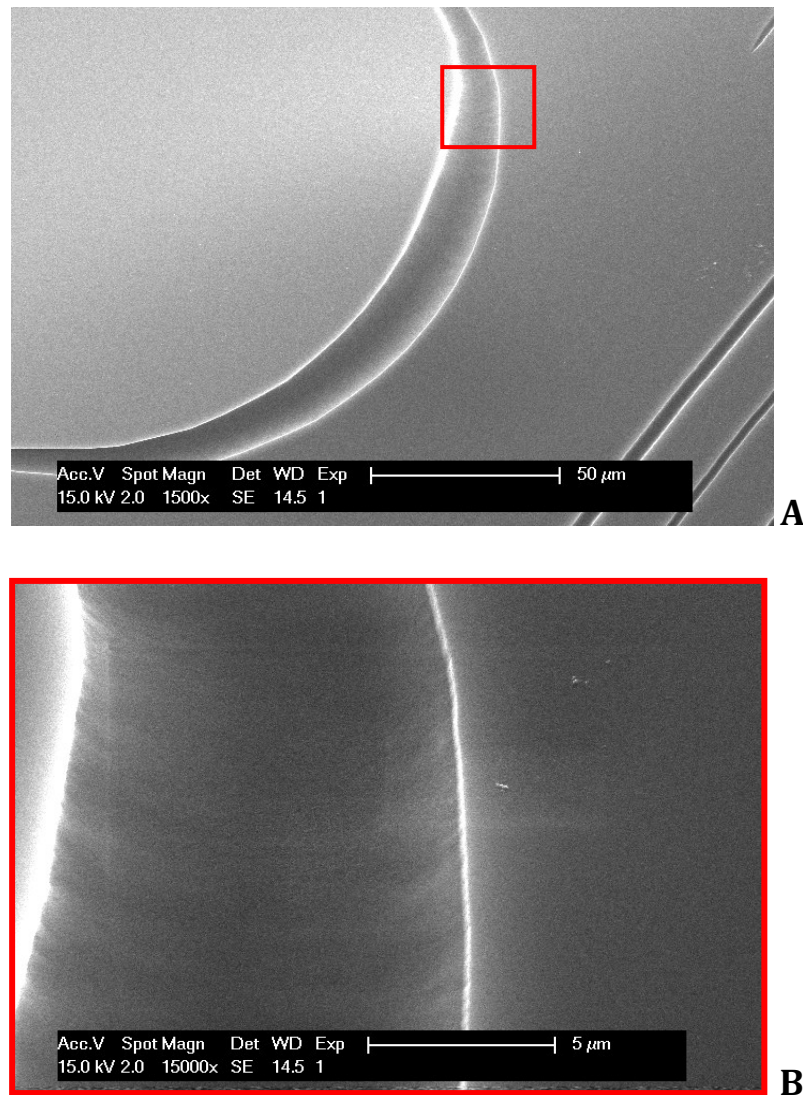


Figure 3.9 - Scanning Electron Microscope (SEM) pictures of the inflated membrane. A) Delamination around islands is due to the high strain in the elastomeric membrane that is surrounding the stiff material B) A detail of the same delamination. A small valley in the PDMS takes place at the edges of the island

We were interested in the strain along the cross section of the membrane, and a 2D model can give us reliable results with lower time of computation. Meanwhile the symmetry condition along the vertical axis allowed us to define just one half of the device, computing the structure with higher accuracy. With the aim of finding the correct deep of this indentation in our 20 μm thick membrane we run two different simulations, one with 4 μm and the other with 8 μm (Figure 3.10). These values have been chosen according to the fabrication process required to create this indentation in the PDMS. An indentation of 8 μm reduces the maximum strain in the membrane by more than 50% (Figure 3.11). Obviously this peak in the strain is reached in the region of the membrane attached to the island, the same one in which we observed delamination.

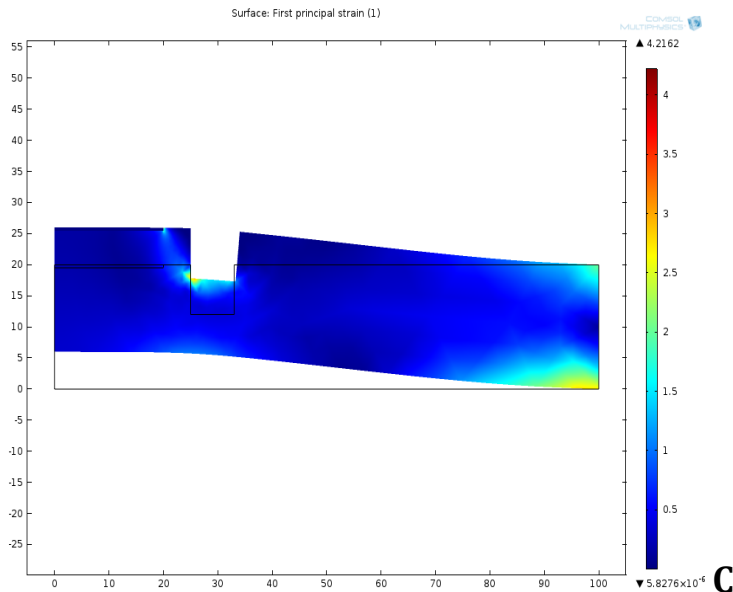
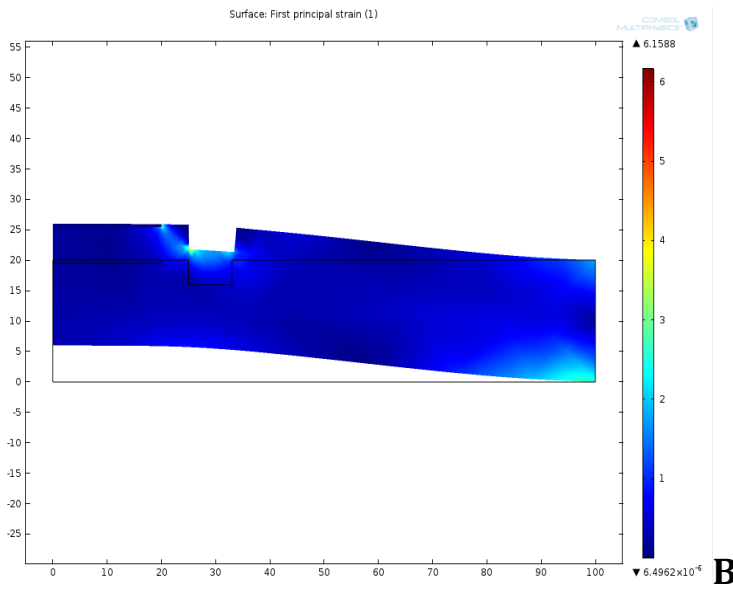
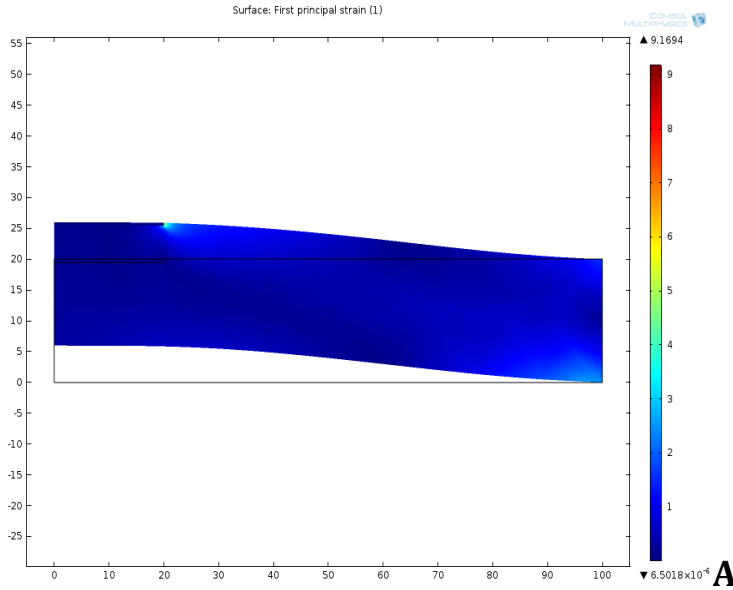


Figure 3.10 - Two-dimensional views of the membrane cross section once a 70 KPa pressure is applied from the backside. Symmetry condition is imposed along the vertical axis, allowing a more accurate simulation of the first principal strain. Second and third principal strains are not reported in this study, their values are extremely lower compared to the first principal one. Three different configurations have been analyzed, without any indentation (A), 4 μm indentation (B) and 8 μm indentation (C). The shape of the membrane when no pressure is applied is showed with a black line beneath the inflated membrane.

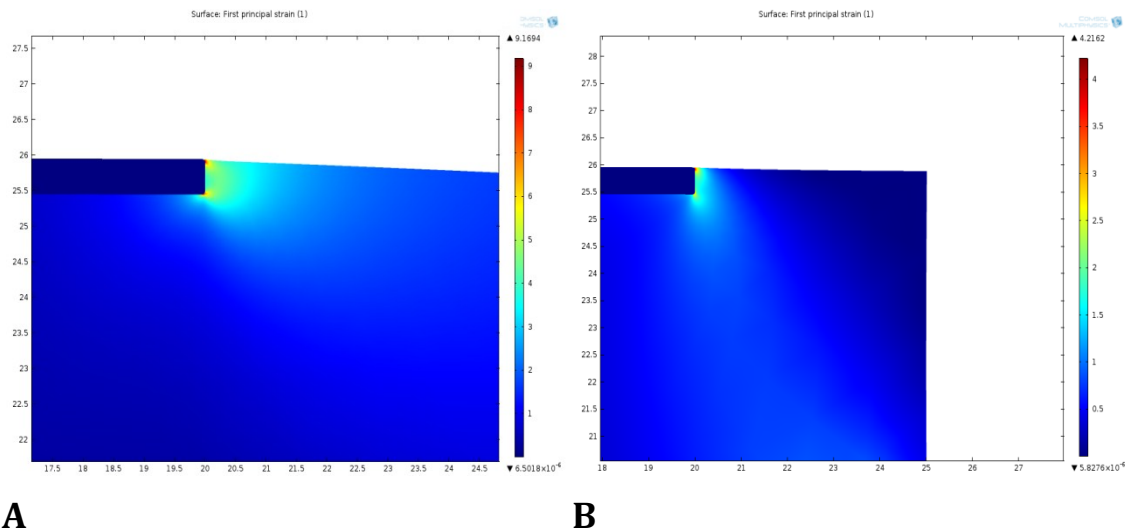


Figure 3.11 – A detail of the inflated membrane surrounding the island. With an 8 μm indentation (B) the maximum strain is reduced by 54% compared to the base condition without any indentation (A)

The reduction we observed gave us evidences of the effectiveness of this approach. In the results section experimental outcomes will be showed and discussed.

3.3 BULGE TEST

Having fabricated stretchable membranes combined with stiff material, in the form of rigid Poly-Silicon or Silicon Nitride islands, the next step, after the fabrication process, is to investigate the ability to stretch of the membrane. Conventionally, for this purpose two different tests can be performed. The first approach is the tensile test, whereby a sample with known geometry is loaded at its both ends by an increasing force, while the change in its length is recorded. Exactly this technique was used by Lacour as well as by Shea to test the stretchability of metals deposited on 1 mm [9] and implanted in 200 μm [11] thick PDMS substrates. However, in this project, the fabrication process performed and the small size of the elastomeric membrane do not allow us to peel off the flexible part of the device from the surrounding. Even the small thickness of the elastomeric membrane, in some experiments below 30 μm , can present problems in handling.

As alternative to the tensile stress test, the bulge test technique was implemented in this project. This measurement method is usually used to characterize the material properties of thin rigid films such as Si, Si_3N_4 and hard polymeric films [11].

The method was firstly applied to a compliant material by Shea to test the stretchability of implanted metal ions in PDMS [11]. In this work a pressure was applied to the elastomeric substrate containing stiff islands, which resulted in change of the inflection height of the membrane.

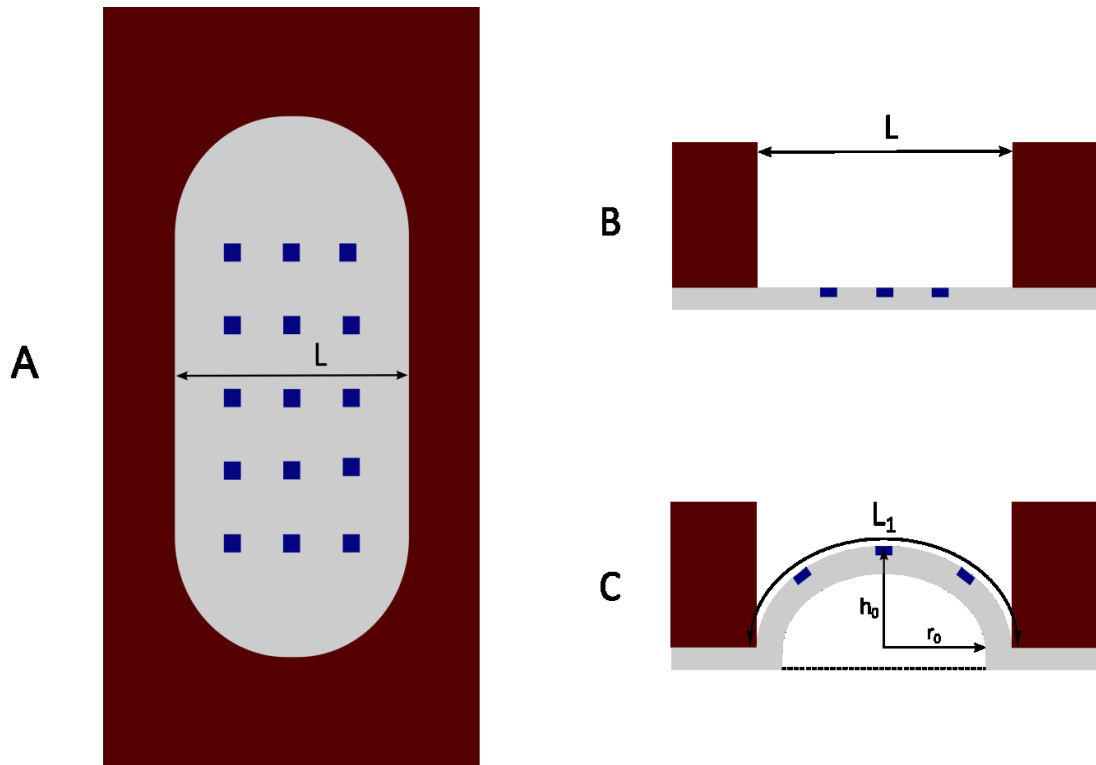


Figure 3.12 - Bulge test principle: A) a free-standing membrane (in grey) on a rigid substrate (in brown) with an initial length L . B) side view of the stack, stiff islands are represented with blue rectangles. C) As pressure is applied, the planar membrane transform into a cylindrical cup with height h_0 and the elastomeric substrate elongates to a new length L_1 .

From these measurements the inflection height as a function of the applied pressure was obtained. In detail, the bulge test principle developed in this project is overviewed in Figure 3.12. A free-standing planar PDMS membrane (in grey) with a length L (1.2 mm) is partially supported by a rigid Silicon substrate (in brown). On the backside of the membrane stiff islands are deposited (in blue). A side view of the membrane is shown in Figure 3.12 B; this image depicts the length of the membrane L once no pressure is applied. The membrane is then inflated by applying a back pressure; as a result the planar membrane deforms to a hemi-cylindrical cup with height h_0 (Figure 3.12 C) and the elastomeric substrate is stretched. The membrane is elongated to length L_1 ; as the pressure is stepwise increased, the vertical displacement of the membrane center h_0 is measured via confocal microscopy and the strain in PDMS can be consecutively deducted. Considering the difference between the Young modulus of the substrate and the one of the islands, that is roughly 10^3 times bigger, we can assume that just PDMS deforms while the membrane is inflated. Also the simulations performed by [3] in similar setup showed that the strain within the islands is negligible, while the elongation is mainly accommodated by the substrate. We are now interested in calculating the strain in the PDMS both according to the inflection height that has been measured and the

percentage of PDMS in the cross section. The strain is calculated from the vertical displacement as follows [11]

$$\varepsilon_0 = \frac{L_1 - L}{L_{PDMS}} \approx \frac{2}{3} \left(\frac{h_0}{r_0} \right)^2 \left(\frac{L}{L_{PDMS}} \right)$$

Where h_0 is the maximum vertical displacement of the membrane, r_0 is half of the total diameter L of the membrane, L_1 is the length of the membrane once inflated and L_{PDMS} is the length of PDMS in the cross section before the membrane is inflated. The term $\frac{L}{L_{PDMS}}$ adapts the strain according to the assumption that the stiff islands do not deform while the membrane is stretched or inflated. This concept is clarified in Figure 3.13, where two membranes with the same initial and final length, but with different amount of PDMS and stiff material in the cross section, are stretched.

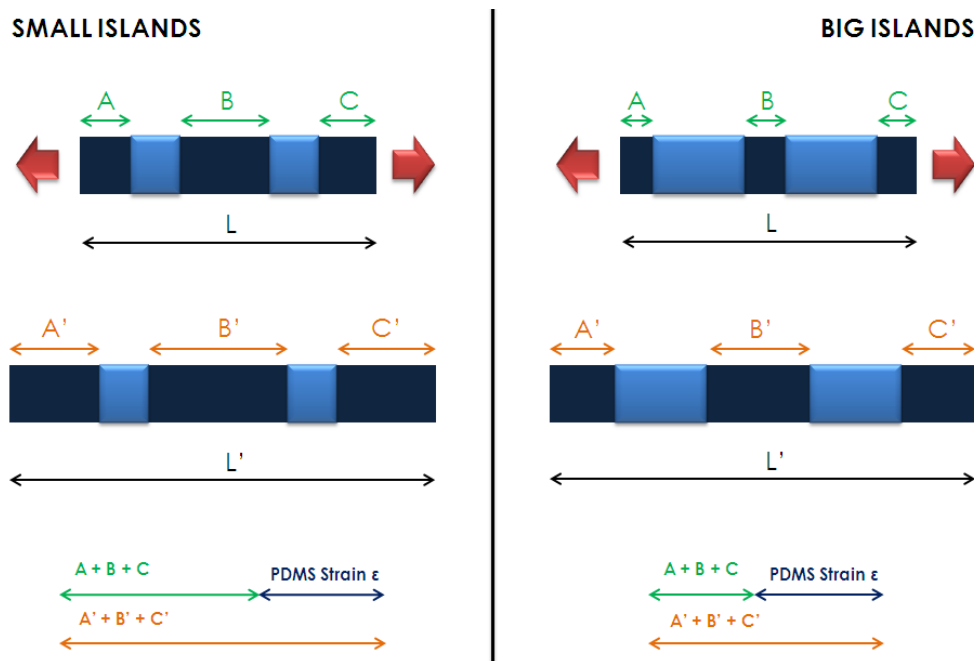


Figure 3.13 - Cross section of two different membranes with different islands size, before and after stretching. The elastomeric membrane is represented in dark blue and the islands are depicted in light blue. Notwithstanding the initial and the final length of the two membranes are the same, the hypothesis that stiff islands do not deform requires, in case of big islands, a higher percentage strain of the elastomeric substrate.

Also the absolute strain in the PDMS is the same in both of the two situations, but in relative terms the condition with bigger islands requires a percentage strain of PDMS that is higher compared to the one of small islands condition.

The detailed calculation of the strain in the membrane is now introduced. When the membrane is inflated, its surface can be considered as being part of a cylinder. If a cross section is made through the membrane, with initial length L , during inflation, the

membrane can be considered as being an arc length of a circle with radius R_1 and an angle θ . The interconnect length after deformation L_1 can be related to the radius R_1 as follows:

$$L_1 = R_1 \theta$$

Where θ is the angle that determines the size of the arc length L_1 (Figure 3.14). The vertical displacement h_0 of the membrane center is known from measurement and the radius R_1 can be related to it according to the following equation:

$$R_1^2 = (R_1 - h_0)^2 + r_0^2 \Leftrightarrow R_1 = \frac{h_0^2 + r_0^2}{2h_0}$$

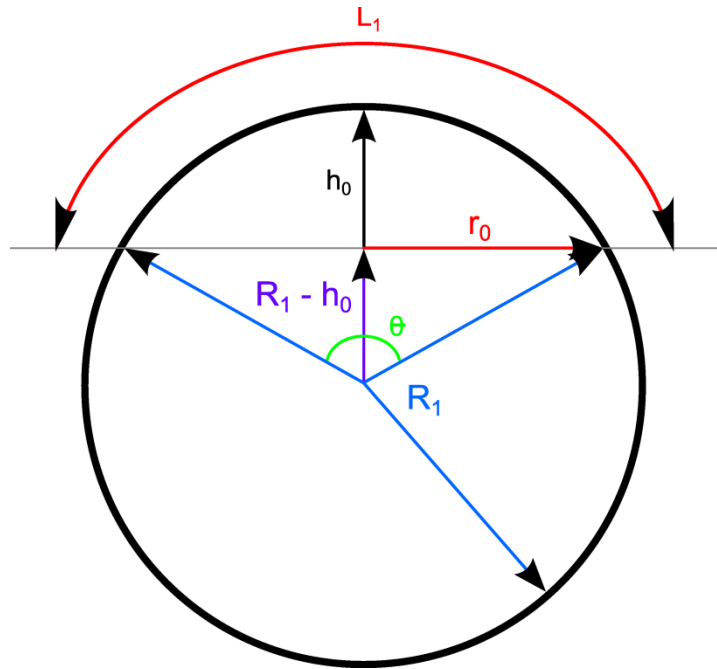


Figure 3.14- Cylindrical modeling of the membrane inflation. A cross-sectional view

Where r_0 is the radius of the planar non-inflated membrane. The angle θ can also be related to R_1 and r_0 as follows:

$$\sin \frac{\theta}{2} = \frac{r_0}{R_1} \Leftrightarrow \theta = 2 \sin^{-1} \left(\frac{r_0}{R_1} \right)$$

According to the previous equations, the following relation for L_1 is delivered:

$$L_1 = R_1 \theta = 2 \frac{h_0^2 + r_0^2}{2h_0} \sin^{-1} \left(\frac{2r_0 h_0}{h_0^2 + r_0^2} \right)$$

Which can be simplified by replacing the arcsine function by the first two terms of its power series, namely:

$$\sin^{-1} = \sum_{n=0}^{\infty} \frac{(2n!)}{(2n+1)(n!)^2 4^n} x^{2n+1} \approx x + \frac{1}{6}x^3$$

For $|x| \leq 1$. The length of the arc L_1 can be expressed as following:

$$L_1 \approx 2r_0 \left(1 + \frac{2h_0^2}{3r_0^2} \right)$$

From which follows:

$$\varepsilon \approx \frac{2}{3} \left(\frac{h_0}{r_0} \right)^2 \left(\frac{L}{L_{PDMS}} \right)$$

Where ε is the strain in the PDMS and $\left(\frac{L}{L_{PDMS}} \right)$ is the term previously discussed, introduced because of the assumption that the islands do not deform under stress.

3.3.1 BULGE TEST DEVICE

In order to stress the membrane of the chips, we projected and developed a bulge test device (Figure 3.15). Its goal is to apply a pressure able to inflate the elastomeric membrane. Once this pressure is applied, the chip should remain in contact with the device without being blown away from it. Therefore, together with the need to stress the membrane, we also faced the problem of clamping the chip on the bulge test device during the experiments. The third point we had to consider was to possibility to look what was happening on the membrane during the inflation, in order to understand where cracks take place and from which pressure level they start to propagate. This last point required the possibility to put this device under a microscope during the experiments.

The microscope also provides a way to relate the inflection high to the strain in the PDMS; once the microscope is focused on the membrane, a needle can measure the height of the plate. Increasing the pressure and focusing every time on the membrane, the needle can measure the inflection height. The strain in the PDMS can be accordingly deducted, as previously showed.

The mechanism of the bulge test device is really simple. Referring to the cross sectional view of the device showed in Figure 3.16, we can notice the function of the two channels drilled in the material. The external one is connected to a vacuum pump. The chip should be correctly placed on top of the device and then the vacuum can be applied; the edges of the chip result clamped on the device thank to this negative pressure.

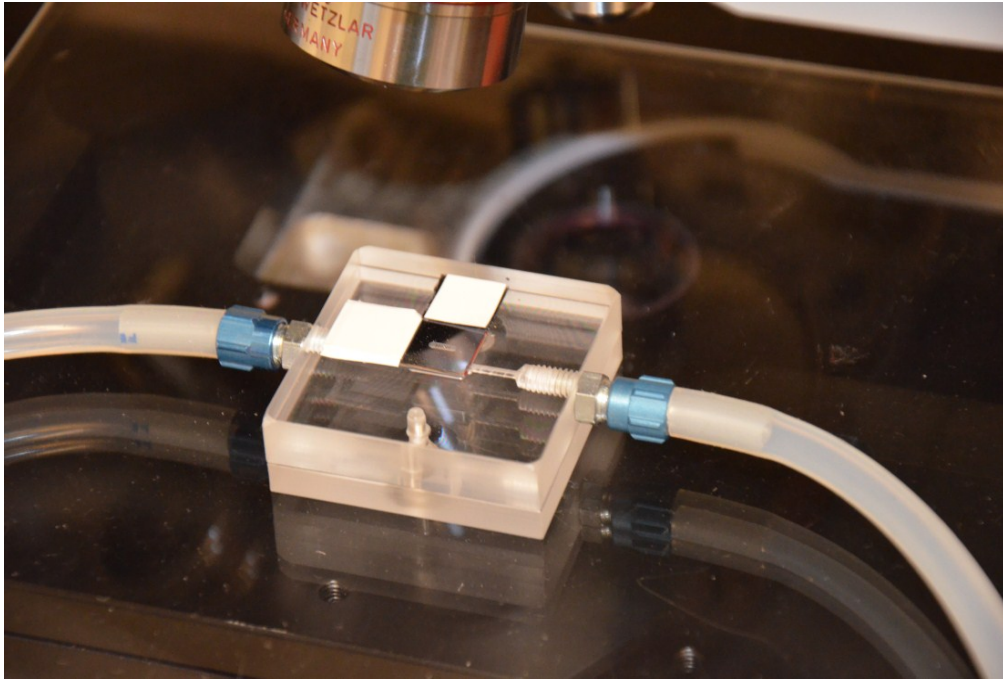


Figure 3.15 - The bulge test device mounted on a microscope plate. Two cables connected on the sides provide the vacuum clamping and the inflection respectively. The white blocks on the two sides of the chip allow a correct positioning of the chip itself

Once the chip is clamped, positive pressure can be applied from the internal channel; this pressure inflates the elastomeric membrane of the chip. Positive pressure can be manually adjusted from 0 to 150 KPa. Meanwhile the microscope needle can measure the height of the plate once the image is focused. The difference between the current height and the one measured when no pressure was applied gives us the current inflection height, which corresponds to a specific strain level in the PDMS.

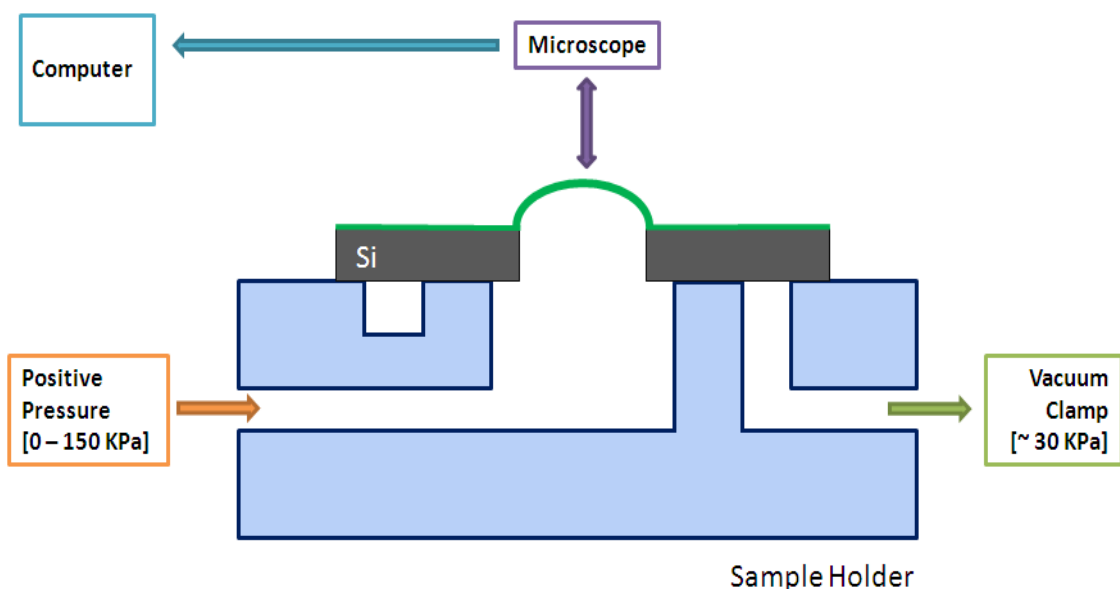


Figure 3.16 - A cross sectional view of the testing device. The green layer on top of Silicon substrate (in grey) represents the inflated membrane.

The overall instrumentation involved for the bulge test is showed in Figure 3.17.

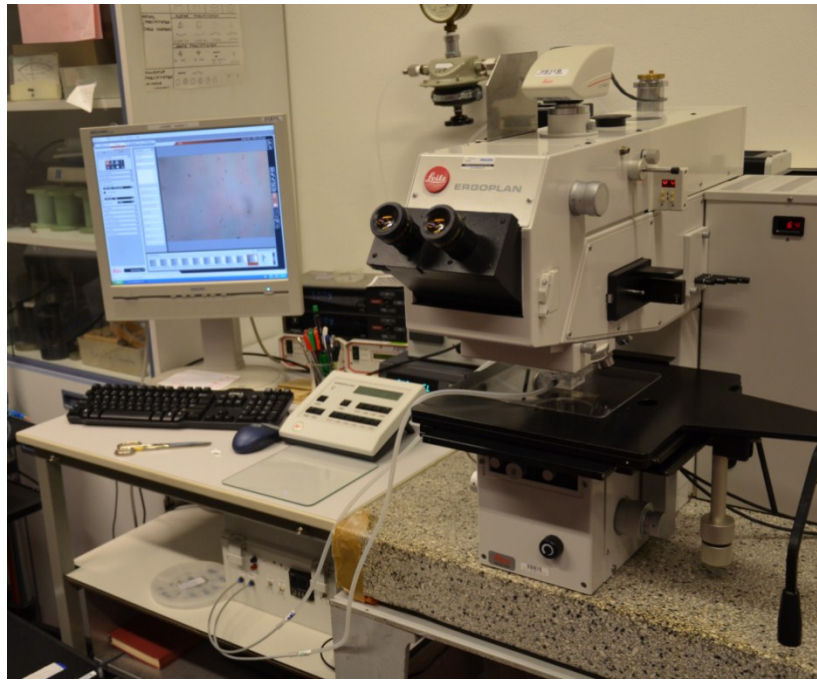


Figure 3.17 - An overall view of the experimental set used to apply pressure on the chips and collect information of their behavior under stress

4. FABRICATION PROCESS

*In this chapter all the approaches used to get stretchable devices are described. For each one all the steps are reported and discussed. The main difference among these approaches lies in the material used as etch stop layer. This material plays its role in the end of the fabrication process, in the moment the Silicon substrate is removed starting from the backside of the chips. Once the Silicon is removed, the elastomeric membrane has no more constrains and can start to be deformed. The etch stop layer is directly in contact with both the PDMS and the stiff islands. In light of this the main problems that can occur can be resumed in two points. The first point is the **adhesion** between the stiff islands and the etch stop layer compared to the one between PDMS and the islands. If stiff islands have strong adhesion with the etch stop layer, its removal can cause the detachment of some islands, affecting the functioning of the chips. This problem can be faced increasing the adhesion between stiff islands and PDMS; primers can be useful for this purpose. The second one is the **mechanical behavior** of the etch stop layer. If the etch stop layer cracks, these cracks can also extend to the islands placed on the top of the etch stop layer. This problem becomes more important if also interconnects are placed among the islands; to make this device working properly almost no crack has to appear inside the elastomeric substrate. In the next paragraphs we discuss different approaches made in order to get stretchable devices.*

4.1 THERMAL OXIDE AS ETCH STOP LAYER

The first trial uses thermal oxide as etch stop layer. Thermal oxide is an optimal etch stop layer, and this is the reason why it has been tried firstly. The results of this first set of experiments gave us important instruction about how to proceed improving the quality of the devices. The thickness of this etch stop layer was chosen to be 1 μm . The strong difference in term of etch rate between Silicon and thermal oxide guarantee optimal device performance during the etching, preventing the elastomeric substrate to be affected by this procedure.

Figure 4.1 resumes all the steps carried out to obtain the final device. Both poly-Silicon and Silicon Nitride have been tested as stiff island materials.

The fabrication process starts with 6 inch Silicon wafers with 1 μm of thermal oxide on both sides (Figure 4.1 A). Wafers have been previously cleaned with two different cleaning procedures. The first one removed organics on the wafer surface while the second one eliminated ions; hydrofluoric and hydrochloric acids are both involved in these procedures. While the presence of ions can affect the outcome of the next fabrication steps, organics removal is quite important mostly for future application of the device, especially if the chips are going to be put in contact with the human body or with cell cultures. After this step wafers have been split in two groups. 200 nm of LPCVD Nitride (low stress) have been deposited on the first group and 550 nm of poly-Silicon have been deposited on the second group (Figure 4.1 B). After the lithography and the etching just few parts of these materials will remain on the top surface of the wafers, representing the stiff islands. For this first step we were more interested in the behavior of each material itself than in a comparison between them; for this reason in place of using the same thickness for both Silicon Nitride and poly-Silicon, we used the maximum thickness possible for both of them. Deposition of Silicon Nitride is quite time consuming; moreover a thicker layer of Silicon Nitride risks to affect the machine used for the deposition depositing dirties on its surface. Due to these reasons 200 nm can be considered as a limit thickness for Silicon Nitride deposition. Poly-Silicon has less strictly limits and these allowed us to place a thicker layer of this material compared to the Silicon Nitride one.

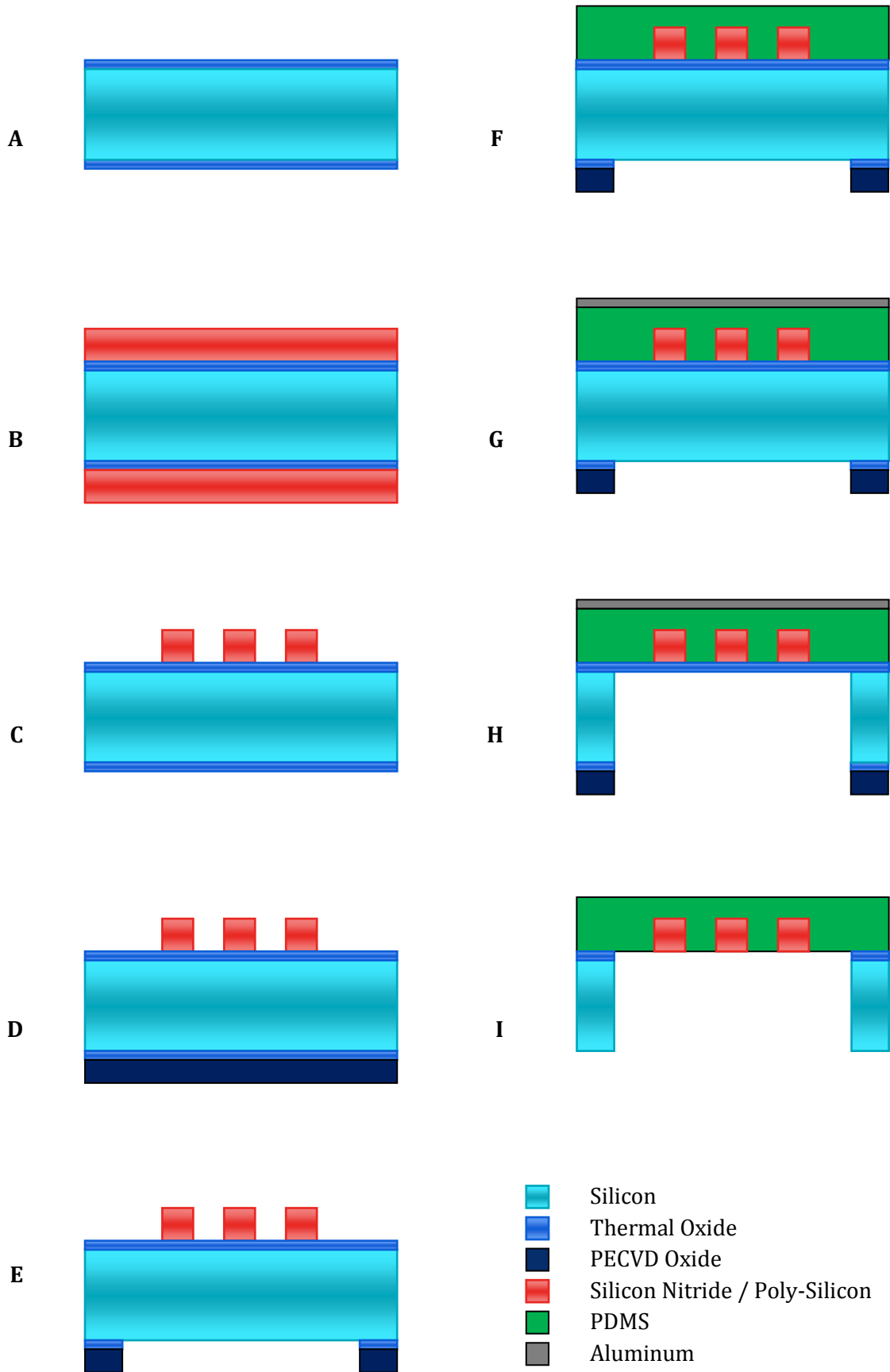


Figure 4.1- Complete fabrication process sequence

Poly-Silicon and Silicon Nitride have been deposited on both sides of the wafer because of the machine configuration that doesn't allow the deposition of these materials just on one side, as we desired. Therefore we dry etched the backside of both the 2 groups of wafers, stopping at the thermal oxide layer on the backside.

Wafers have been cleaned again, removing organics and ions from the surfaces. The cleaning process eliminates all the OH- groups from the surface. These groups are important for the next step of the fabrication process, the wafer priming. The primer is a gas; in order to attach to the wafer surface it needs to find OH- groups on the wafer. Consequently wafers have been rinsed in water and dried before priming with TMSDEA. Then a layer of HPR 504 resist has been deposited on the top of the wafers at 4000 rpm. The thickness of this layer is related to the speed of the deposition process, higher speed creates thinner layer. According to Figure 4.2, 4000 rpm create a 1.37 μm layer of resist.

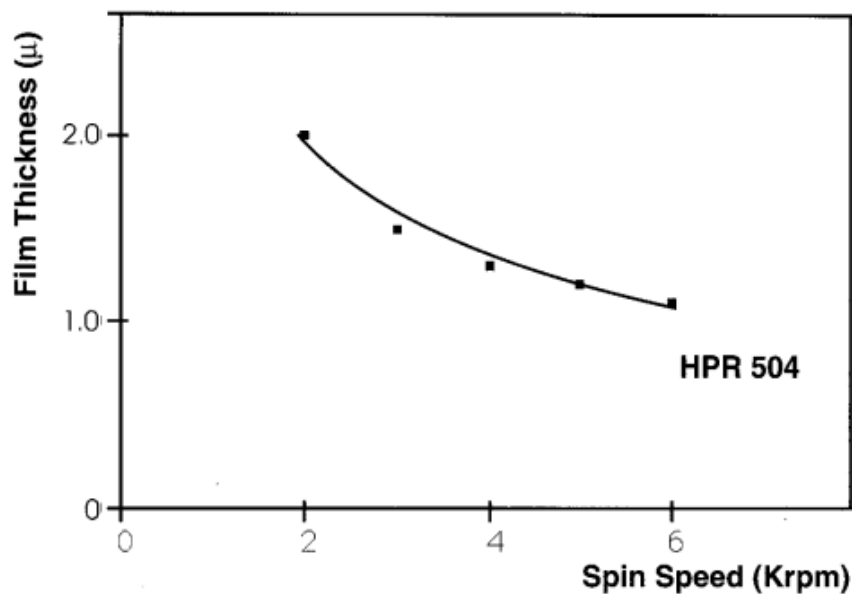


Figure 4.2 - Spin curve for HPR 504 resist [56]

After the deposition of the resist wafers were ready for the photolithography; the aim is to transfer the pattern realized on the first topside mask on the wafers; this pattern represent the distribution of stiff islands on the different chips in the wafer. Hard contact alignment option is chosen for this purpose and, according to the thickness of the resist, we used an exposure time of 7 seconds. Wafers have been developed and some undesired traces of the developer appeared on the backside were removed after rinsing in water and drying the wafers. Some pictures have been collected under the microscope proving no errors occurred until this point (Figure 4.3 and Figure 4.4).

Both poly-Silicon and Silicon Nitride have been dry etched from the topside, than in the barrel we stripped the resist using oxygen plasma for 60 minutes at 130°C with 1000 W power (Figure 4.1 C). Organics and ions have been removed again with traditional cleaning procedures. Then we performed step height measurements, using a load on the needle of 3 mg, to evaluate the size of the step between stiff islands and the surroundings. These measures, performed on all the wafers, revealed the height of the step perfectly matched the thickness of the stiff islands layer.

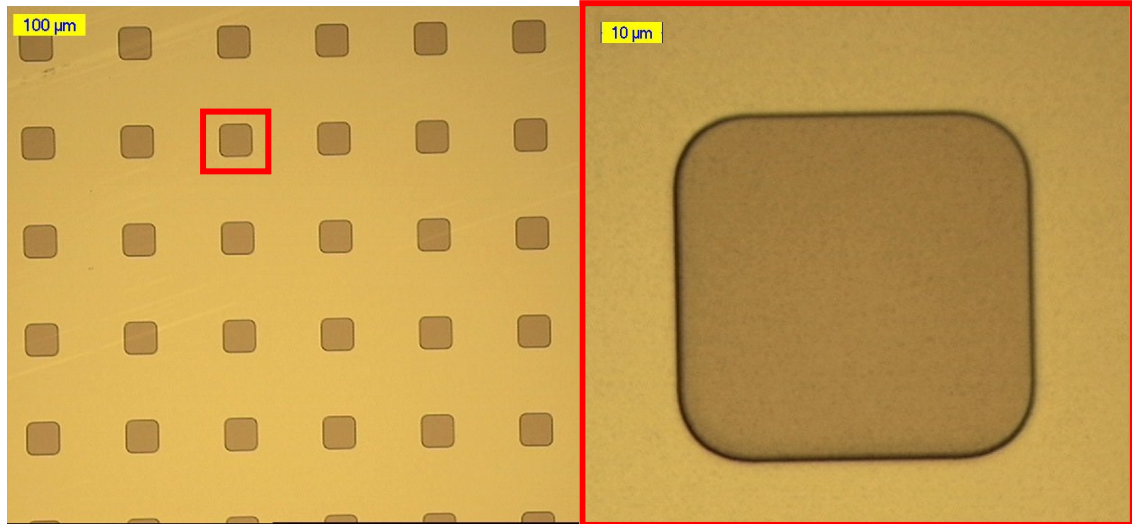


Figure 4.3- 50 μm circled squared islands with 100 μm interisland space

Figure 4.4- A detail of one 50 μm circled squared island after resist development

The second part of the process required patterning the backside in order to transfer the shape of the holes to be etched to get the flexible membrane of the device free to be inflated. On the backside just 1 μm of thermal Silicon Oxide was present; in order to have a thicker layer in which imprint the mask, we deposited other 2 μm of PECVD oxide (Figure 4.1 D). Photolithography with the backside mask has been run in order to transfer the shape of the holes at the backside. After rinsing in water and drying, TMSDEA primer has been placed on the wafers followed by the deposition of 2.5 μm HPR504 resist at 1000 rpm (Figure 4.2). For the exposure of the backside we needed to carefully align the backside mask to each wafer; thus we used the alignment marks placed on the mask and patterned on the topside of the wafers. Due to the thicker resist compared to the one used for the topside, we increased the exposure time to 18.5 seconds and then primer has been developed. Also in this case traces of developer appeared on the opposite side; rinsing in water and drying the wafers removed these spots.

Wafers have been dry etched from the backside through the 3 μm thickness of the two oxide layers, until reaching the Silicon substrate. After 60 minutes in the barrel with oxygen plasma at 130°C (1000 W power), the resist has been stripped (Figure 4.1 E). Normally acetone is enough for resist removal. However the etching process asks for high temperature, that turns the organic material of the resist into Teflon. This is the reason why no more acetone, but oxygen plasma at high temperature, is the way to take the resist out of the wafers. Both cleaning processes have been carried out to remove organics and ions from the surfaces of the wafers. Images from the backside have been collected under the microscope, revealing the outcome matched the requirements (Figure 4.5); also step height measurements showed the size of the step was exactly 3 μm for all the wafers.

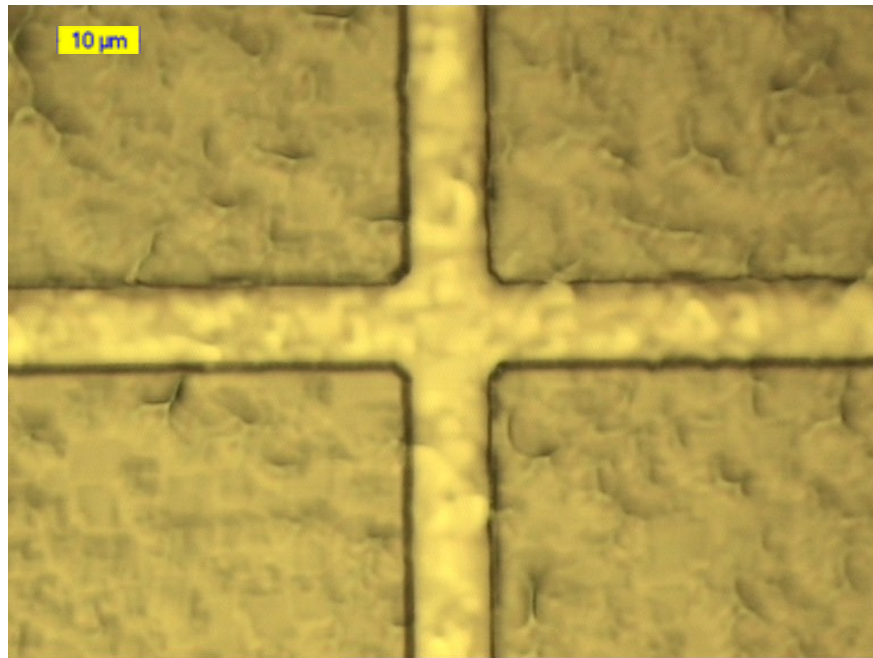


Figure 4.5- 10 μm grooves on the backside designed to facilitate the splitting of the chips at the end of the fabrication process

4.1.1 20 μm PDMS LAYER

Wafers are now ready for spin-coating PDMS on top of them. We prepared PDMS using Sylgard 184 from Dow Corning with 10:1 weight ratio between pre-polymer gel and cross-linker. After the preparation air bubbles inside the polymer have been eliminated using a speed mixer for 90 seconds at 1800 rpm.

To promote the adhesion between PDMS and the topside of the wafers we rinsed in water and dried them in order to restore all the OH- groups on the surface. PDMS has been spincoated on the top of the wafers at 3000 rpm for 60 seconds, allowing us to obtain the desired 20 μm thickness of elastomeric membrane (Figure 4.1 F).

To dry etch the backside it is necessary to place the top side of the wafers on the spincoater; PDMS is a delicate material and would be damaged during this process, therefore a thin anti-stiction layer of Aluminum (50 nm) is deposited on top of PDMS using low power (125 W) and low temperature process because of the mechanical properties of the polymer in the wafers (Figure 4.1 G).

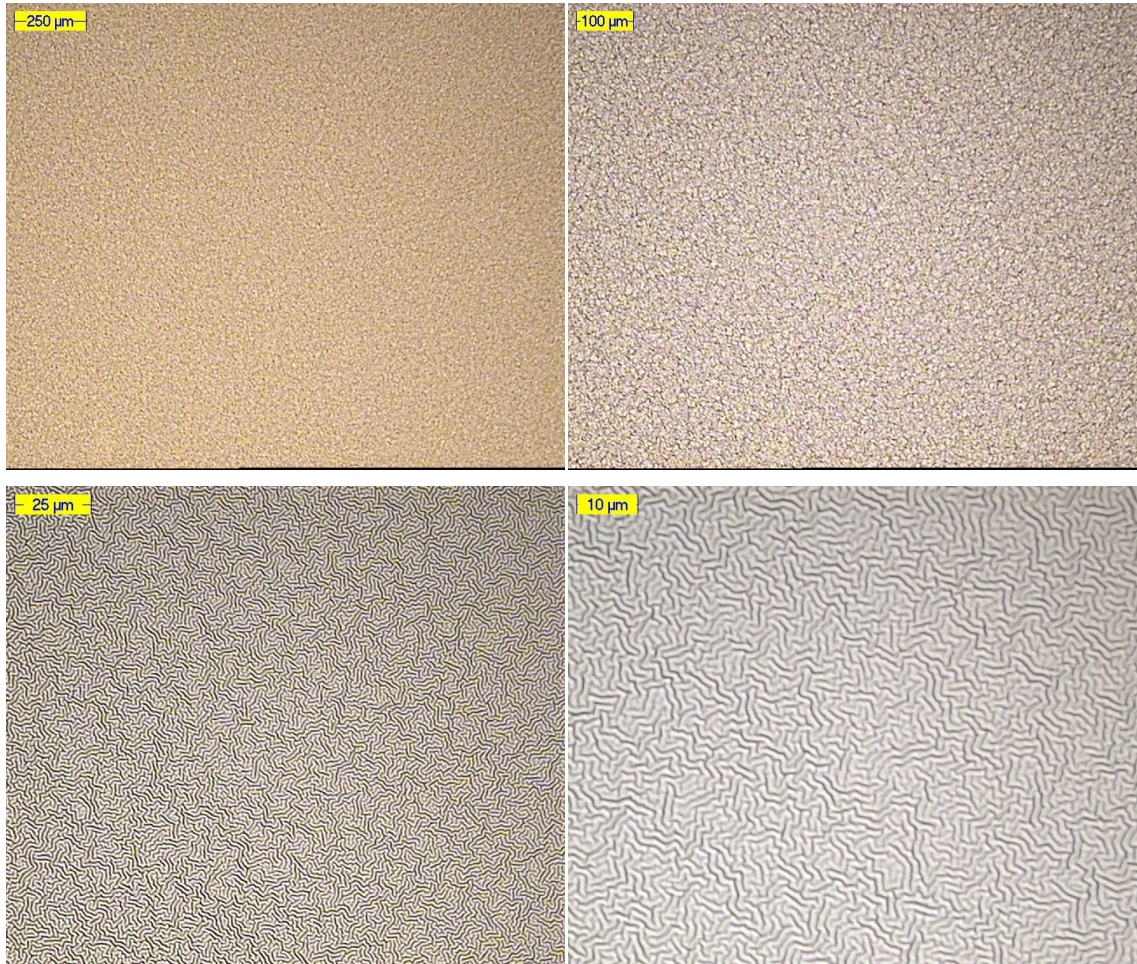


Figure 4.6-Aluminum wrinkles on PDMS seen from increasing magnitudes

As we can see in Figure 4.6 Aluminum use to form very regular structures of wrinkles once spin-coating on PDMS; this is due to the compressive stress that Aluminum releases once spin-coating on the elastomeric substrate. Properties that metals showed in contact with PDMS have already been presented in the PDMS paragraph inside Materials and Methods chapter.

Using the etch mask on the backside, made by 2 μm of PECVD oxide plus 1 μm of thermal oxide wafers have been dry etched from the backside until the 1 μm thermal oxide etch stop layer on the topside (Figure 4.1 H). Inspections under the microscope revealed some cracks took place on some of the islands; fortunately just a few of them were compromised. Interesting aspects about wrinkles and cracks on the elastomeric

substrate can be analyzed. Firstly, the presence of wrinkles is quite interesting; according to the directions of the stress, wrinkles propagate horizontally, vertically or sinusoidally (Figure 4.7). These wrinkles took place both in the oxide layer and in the Aluminum one that are going to be removed; nonetheless they do not affect the performance of the final device.

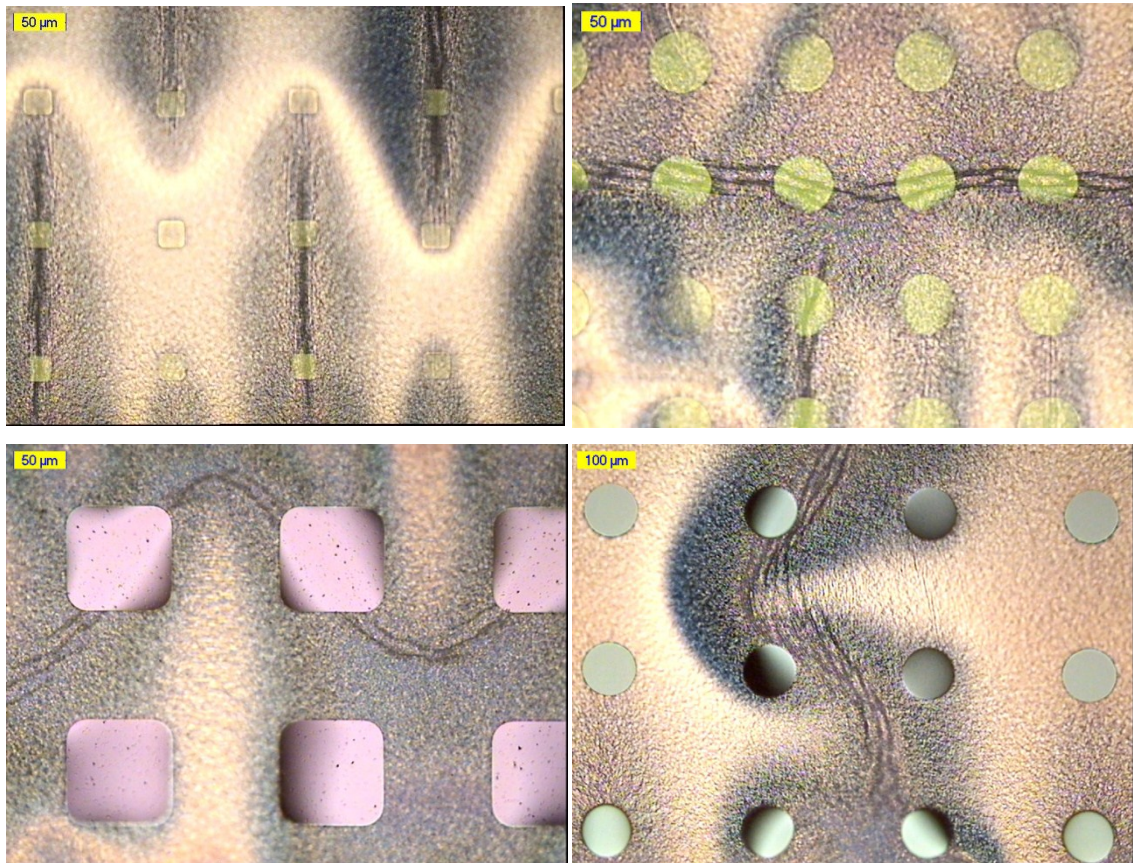


Figure 4.7- Wrinkles on Aluminum and Silicon Oxide layers after Silicon is dry etched from the backside. According to the direction of the stress in the membrane, these wrinkles propagate horizontally, vertically or sinusoidally

Thermal oxide layer is the reason why this phenomenon occurs. When this oxide layer is thermally grown on Silicon, it tries to expand according to the force raised while the process takes place; conversely the Silicon layer prevents the thermal oxide to enlarge. A compressive stress rises in the oxide layer and, when the Silicon is removed from the backside, the oxide finally releases its stress. Smaller wrinkles are the ones that take place in the Aluminum layer, in the thermal oxide layer, bigger wrinkles appears. Thin layers are more flexible than thicker ones; in our case Silicon Oxide is 20 times thicker than Aluminum. In light of this, its flexibility is lower and its wrinkles are supposed to be bigger compared to the Aluminum ones. According to the position of the islands and the shape of the hole, this stress can be released horizontally, vertically or on both the directions. The membrane follows the expansion of the oxide layer, and Aluminum on

top of it forms wrinkles in the regions in which it is compressed. An example of what can happen is reported in Figure 4.8; here the membrane is supposed to release its stress horizontally. In light of this, the Aluminum layer is compressed in the valleys of the sinusoid, forming wrinkles in these regions. Cracks will most probably take place vertically, in the direction in which Oxide was not able to release its stress.

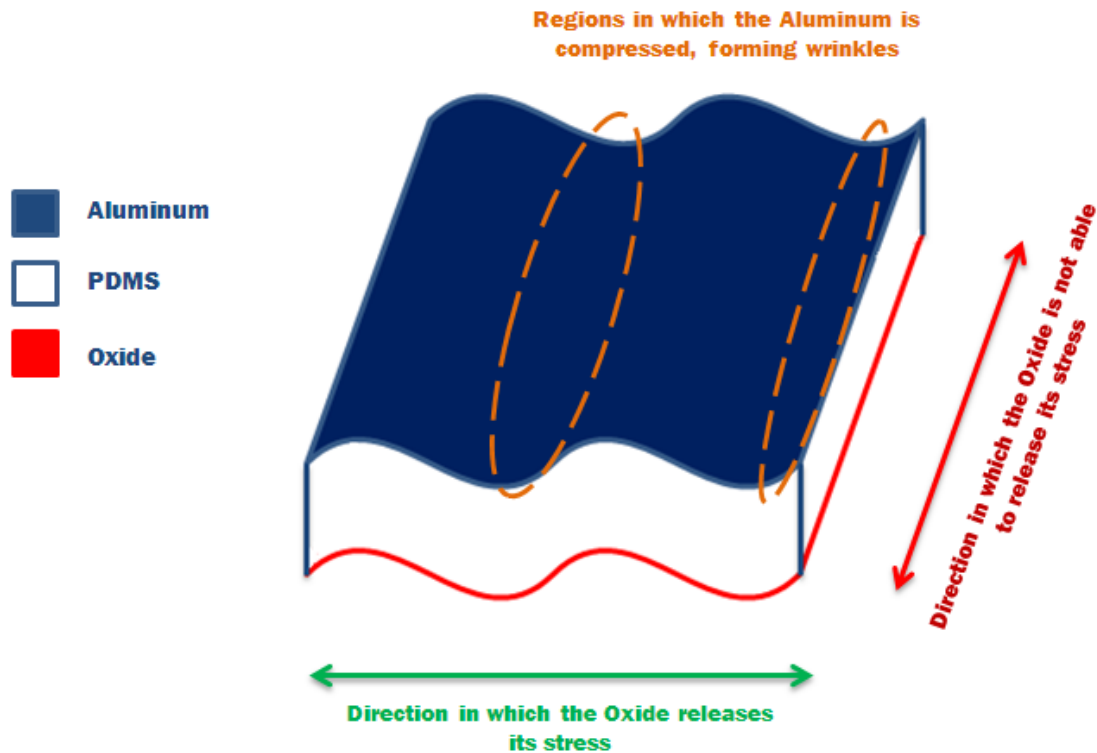


Figure 4.8 - A schematic of the membrane. In this example stress is supposed to be released horizontally. Therefore Aluminum forms its wrinkles vertically on the top of the membrane

Also some cracks appeared in the oxide layer; cracks are more problematic for the reliability of the device, because they can affect also the islands and the interconnections that should be placed in between, preventing the device to work properly. Silicon Oxide is a brittle material that cracks easily; these cracks do not affect the elastomeric substrate but they can effortlessly propagate to the islands attached to the oxide layer as well. Silicon Oxide cracks when it cannot expand; most of the time these cracks are perpendicular to the wrinkles, as we can see in Figure 4.9. In these cases the oxide layer was able to release its stress only in one direction, as the wrinkles on the Aluminum layer show; conversely in the other direction the stress, still present, was not released, causing cracks.

Once the Silicon Oxide is removed, these cracks are no more present; however if they have affected the islands, these islands remain cracked and they would not operate

properly. This phenomenon requires further investigations in order to address how different islands shape, dimension and position can affect the way the oxide releases its compressive stress.

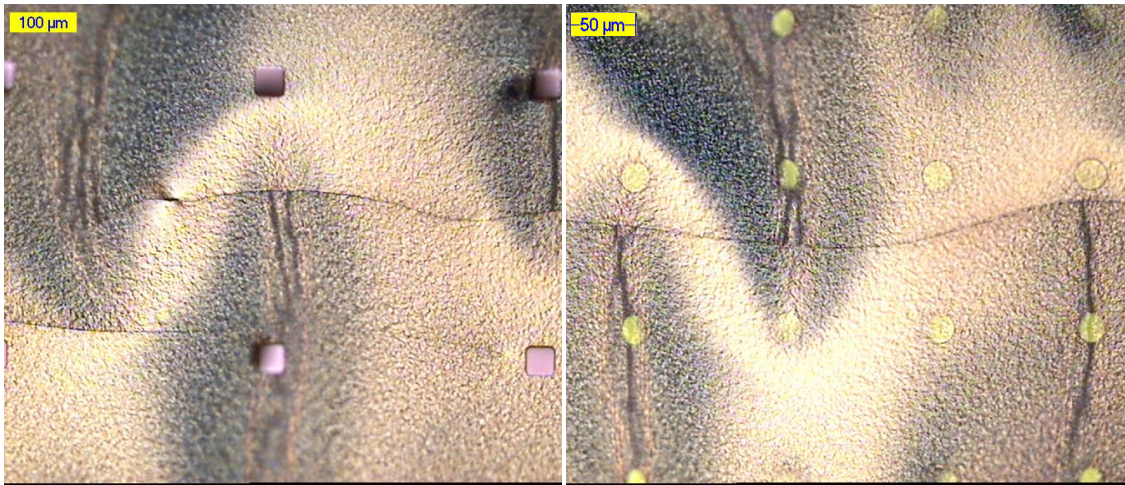


Figure 4.9- Cracks on the membrane. These cracks are often perpendicular to the wrinkles of the membrane. As explained before in this case the membrane was able to release its compressive stress just in one direction, causing bending of the membrane (described by wrinkles on the two extremity surfaces) and cracks in the other direction.

Aluminum layer was wet etched in PES at 30°C for 1 minute (Figure 4.1 I) and then we rinsed the wafers in water for 10 minutes; in order to investigate the best way to remove the oxide several approaches have been made.

In the first approach we filled the holes of the wafer with Triton X-100 before etching the thermal oxide with BOE. Triton X-100 (Figure 4.10), a commonly used detergent in laboratories, is a nonionic surfactant which has a hydrophilic polyethylene oxide group (on average it has 9.5 ethylene oxide units) and a hydrocarbon lipophilic or hydrophobic group.

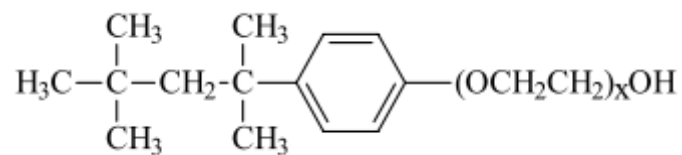


Figure 4.10- Molecular structure of Triton X-100 [57]

We left the wafer for 10 minutes in the BOE etchant and then rinsed it in water and dried at room temperature. A lot of wrinkles appeared looking at the surface under the microscope (Figure 4.11); they formed in the oxide layer, the Aluminum, in fact, has already been removed. These wrinkles formed because the oxide layer, not completely removed, has become really thin, thus more flexible, than before. It can now release its stress in the whole membrane except where stiff islands are. This evidence explains also

the regular structure of the wrinkles all around the islands. Both the quality of the surfactant and the time we left the wafer in the BOE etchant can have affected this outcome.

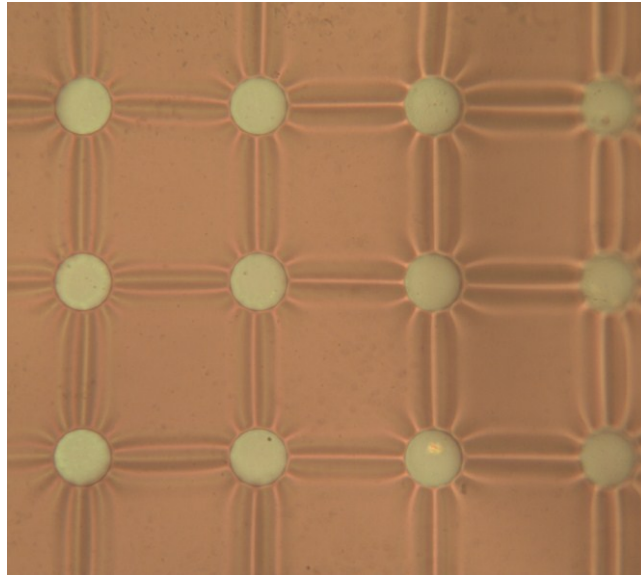


Figure 4.11 - Elastomeric substrate after BOE etching previously treated with Triton X-100. Wrinkles are all over the surface [100x magnification]

To improve this result we decided to change the surfactant because of some dirties we saw under the microscope and to increase the time in the BOE etchant in order to completely remove the oxide layer (the presence of wrinkles is a good evidence to understand whether the oxide layer is still present or not). For the second experiment we used 1% Decylamine in Isopropyl alcohol (IPA) and we left the wafer for 15 minutes in BOE etchant. Results showed improvements in the quality of the device (Figure 4.12), however not all the oxide has been removed yet.

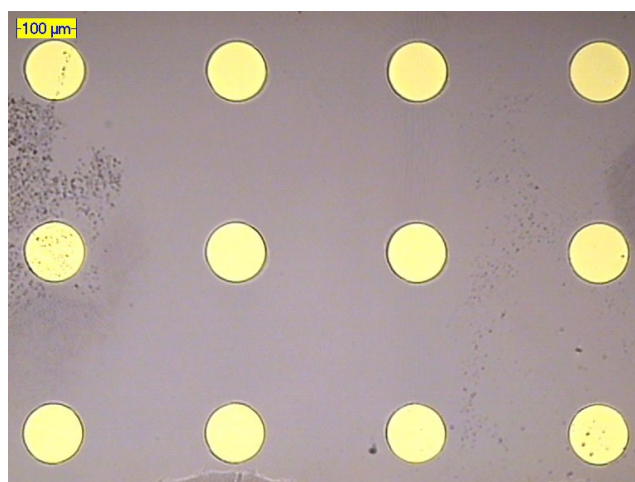


Figure 4.12- Membrane inspection after removal of Silicon Oxide. No more wrinkles are present; the oxide layer has been completely removed

As we can see in Figure 4.13, wrinkles are still present in some of the chips; differently from the first trial, these wrinkles are not on the whole surface of the wafers but close to the edges of the holes. Therefore the oxide layer has been completely removed just from the central part of the hole.

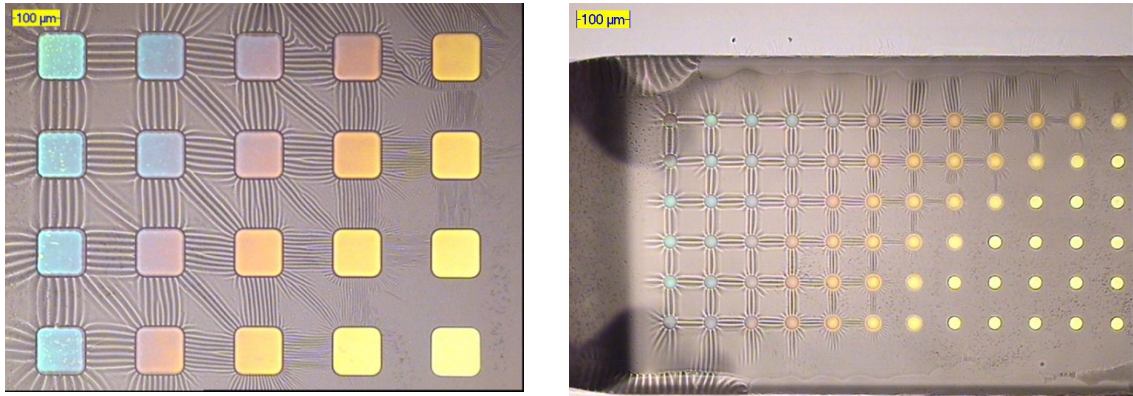


Figure 4.13 - After BOE etching the silicon oxide has been completely removed from the center of the hole but not around the edges. Different colors of the islands refer to different thickness of the oxide layer still present above

In order to improve this result, our idea was to bring the edges of the hole hydrophilic and increase again the time in the BOE etchant. The PDMS surface can switch to hydrophilic thanks to oxygen plasma [46]. The wafer has been exposed to oxygen plasma at 25°C for 1 minute with 300 W power and then left in the BOE etchant for 17 minutes; the result showed another important step forward for the quality of the device (Figure 4.14).

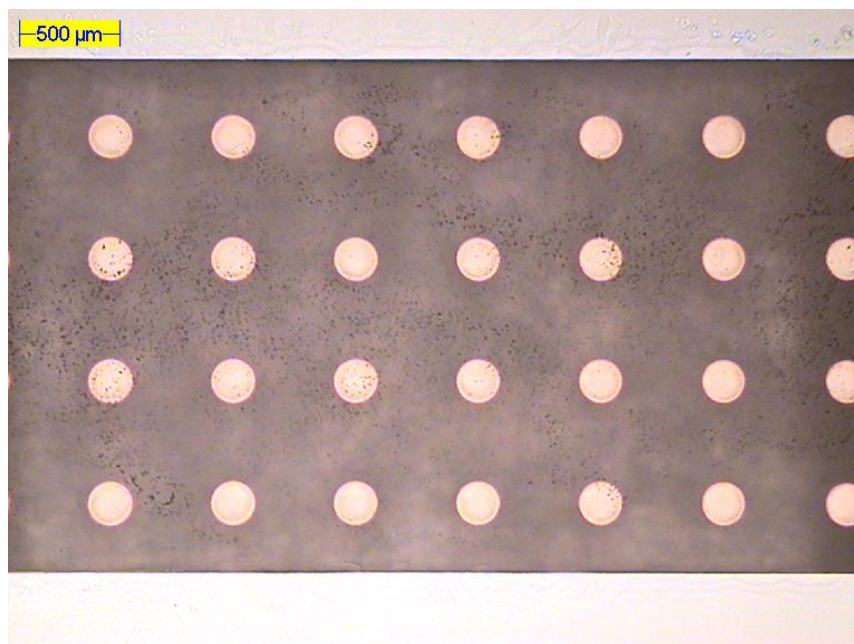


Figure 4.14 - Inspection of the membrane after silicon plasma exposure and BOE etching. No more wrinkles affect the membrane; the entire Silicon Oxide layer has been removed

The only problem is related to dirty appeared in some corners of the holes (Figure 4.15), probably due to some reactions with the surfactant.

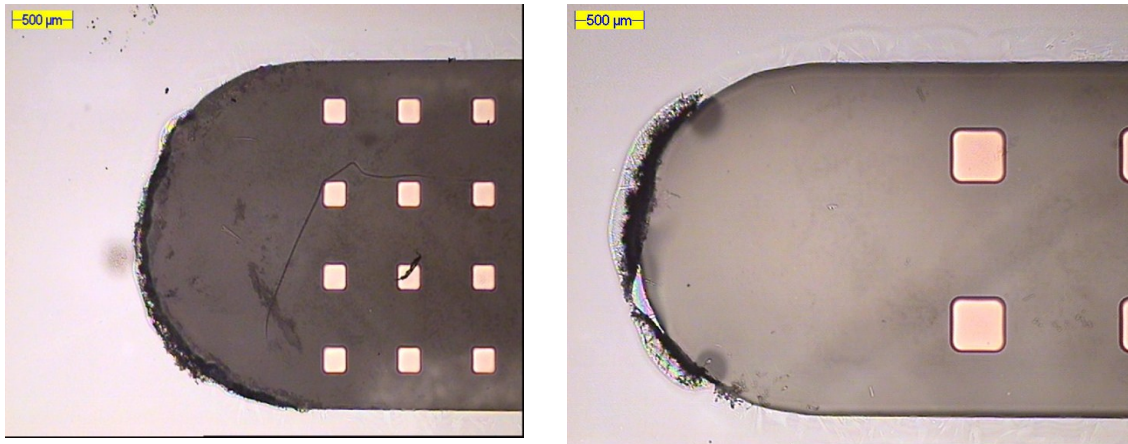
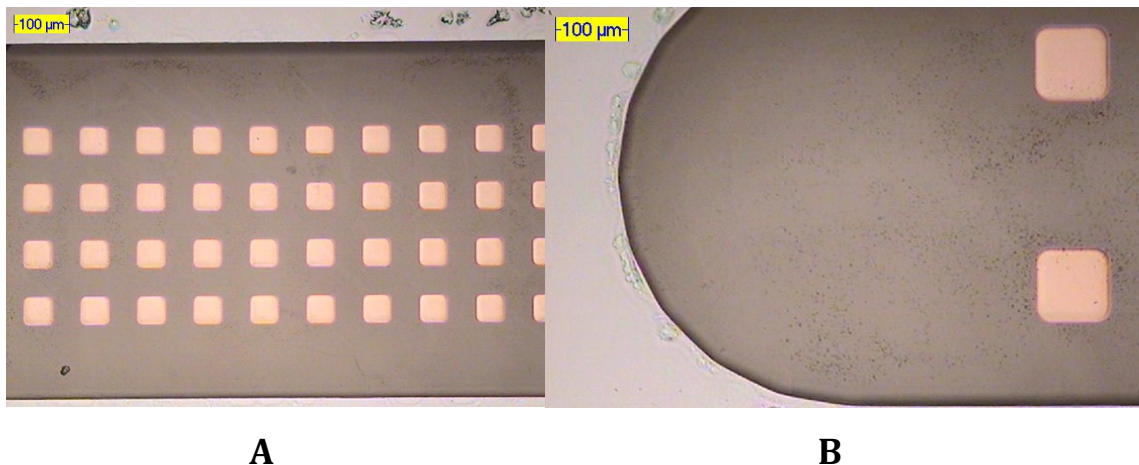


Figure 4.15 - Dirty spots in the corner of the edges. In order to inspect the role of the surfactant in the formation of these spots we repeated the experiment using water in place of it

These dirties do not affect the functioning of the device but can compromise the growth of cells once they are placed on top of the membrane. In order to have a better understanding of this phenomenon we repeated the last experiment using water in place of the surfactant. If these dirty disappeared the reason would probably have lied in the surfactant and the reactions that involves it. The best results have been reached with this last approach; neither wrinkles nor dirties appeared on the chips, that are ready to be tested under mechanical stress (Figure 4.16 A and B).



A

B

Figure 4.16 - A) No more wrinkles affect the membrane B) No dirty spots are now in proximity of the corners, showing that their formation in the previous experiment was mostly due to the reactions that take place with the surfactant

4.1.2 80 µm PDMS LAYER

In this second set of experiments we decreased the spin speed from 3000 to 1500 to increase the thickness of PDMS layer. Before spin-coating PDMS we differentiated the wafers in two groups in order to investigate different approaches improving the islands'

adhesion to the elastomeric substrate. In the first group we rinsed in water and dried the wafers restoring the OH- groups on the surface; in the second approach we performed a plasma descum at 25°C for 2 minutes, with 600 W power. Plasma descum represents an advanced cleaning procedure, that oxidizes the wafer surfaces. PDMS has been spin coated on all the wafers and cured in the oven at 90°C for 30 minutes. According to the experimental measures from [31], with 1500 rpm a 80 μm layer of PDMS should be created (Figure 4.17).

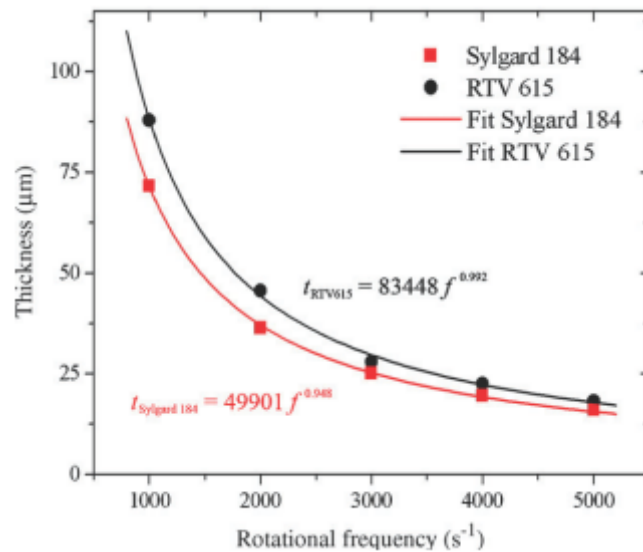


Figure 4.17 - Spin curve of RTV615 and Sylgard 184, mean across the whole wafer area [31]

Thin Aluminum layer (50 nm) has then been deposited on the top surface as done for the first experiment; consequently the silicon has been dry-etched from the backside. A thicker layer of PDMS implies thinner wrinkles of the Aluminum layer on top of it (Figure 4.18).

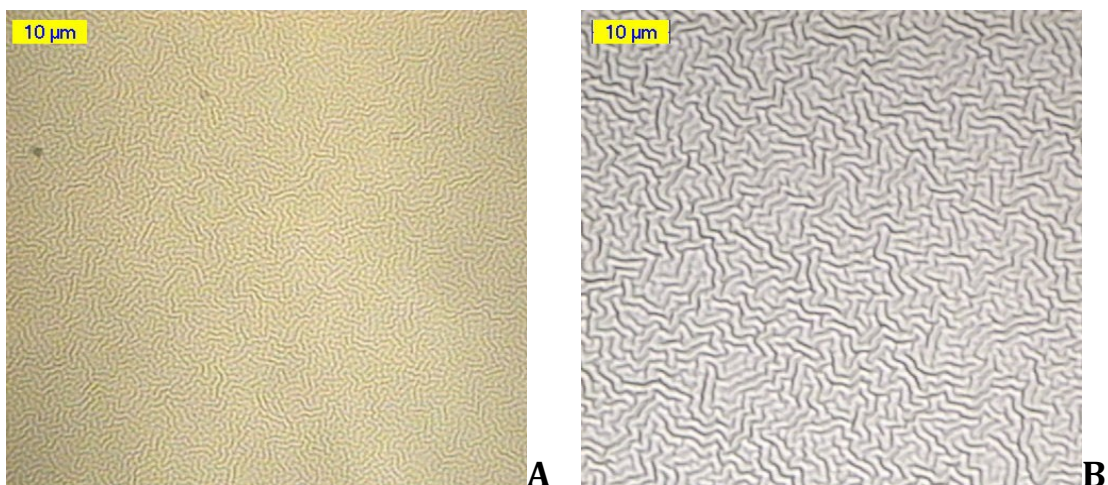


Figure 4.18 - Comparison between Aluminum wrinkles above 80 μm (A) and 20 μm (B) PDMS layer

The process is completed with the wet etching techniques. PES etchant removed Aluminum from the top surface. Then we placed Isopropanol in the holes and we left the wafers for 20 minutes in the BOE etchant for the Oxide removal. Because of the compressive stress released by Thermal Oxide once Silicon is removed, some membranes showed wrinkles and few of them cracked; however the outcome of the fabrication process was positive (Figure 4.19) and the chips have been inflated in order to compare the effect of a different thickness of the PDMS layer.

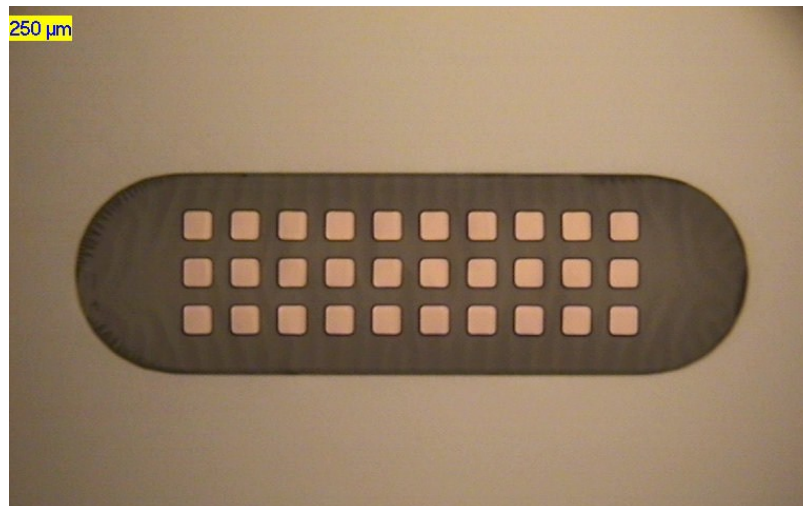


Figure 4.19 - An overall view of the 80 um thick PDMS membrane after Aluminum and Oxide removal. In this case nor wrinkles neither cracks took place on the membrane

4.2 ZERO-STRESS PECVD OXIDE AS ETCH STOP LAYER

This second fabrication process tried to improve the previous one in terms of wrinkles, cracks and island delamination. For wrinkles and cracks the reason was mostly the compressive stress inside the Thermal Oxide layer. As we observed, this stress can be released when the silicon is removed from the backside. Compressive stress, once released, generates wrinkles and cracks in the membrane; these cracks can also propagate to the islands. Two approaches can solve this problem; the first one replaces Thermal Oxide with Aluminum as etch stop layer. Aluminum has a tensile stress; therefore once this stress is released the surface remains flat in place of bending, as in the case of Thermal Oxide. However using Aluminum as etch stop layer may be a problem with the clean room instrumentation; some particles during the etching can be released contaminating the machine. The other option, the one we chosen, is to replace Thermal Oxide with Zero-Stress LPCVD Oxide, a material supposed to nullify the compressive stress inside the etch stop layer, maintaining almost the same fabrication process described in the first paragraph (Figure 4.20). To avoid delamination, we used the strategy discussed in the FEM paragraph, creating an indentation in the membrane in the proximity of the islands, reducing the strain of PDMS in those regions.

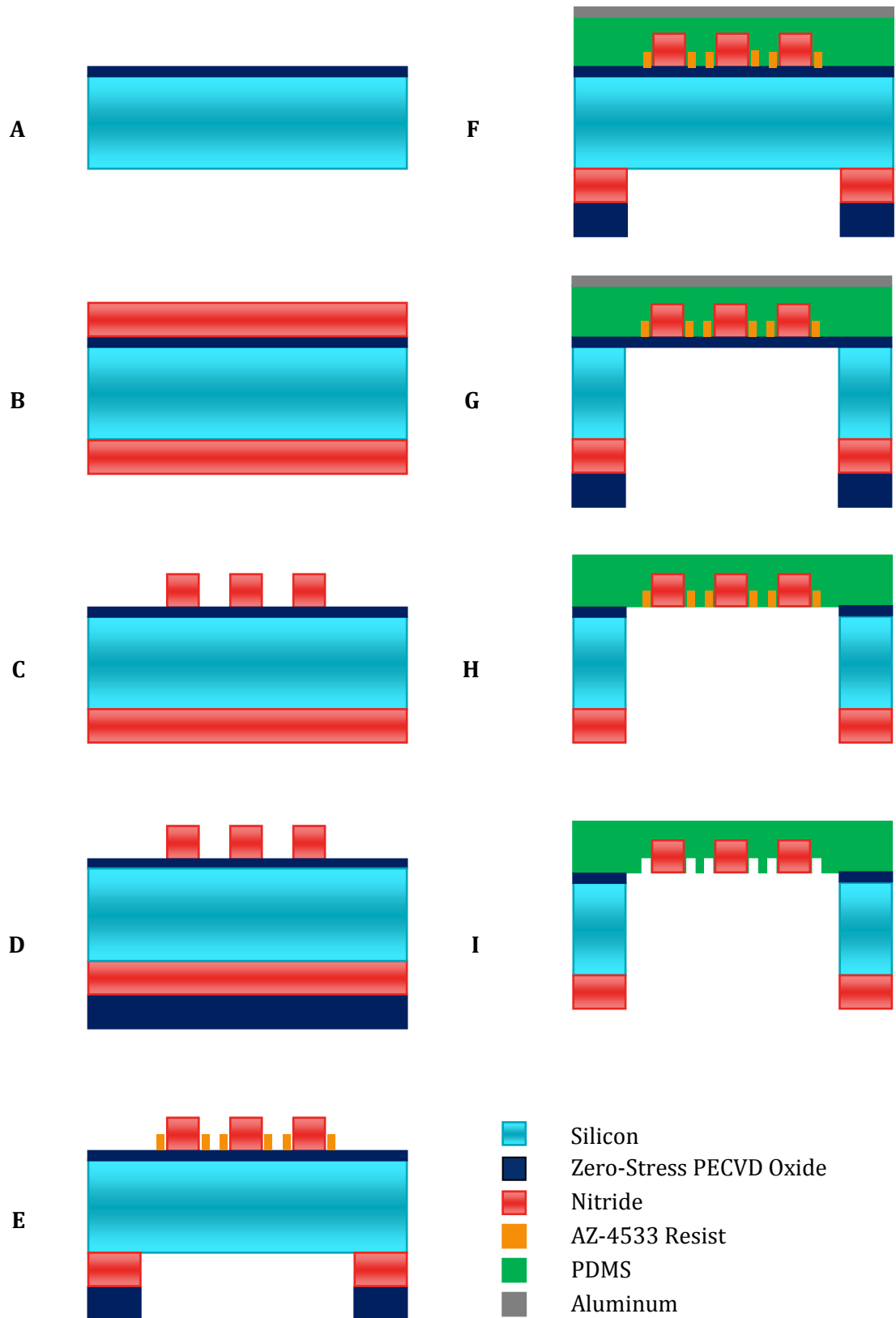


Figure 4.20 - Complete fabrication process sequence for Nitride islands. Variations for Poly-silicon will be described in the chapter

The fabrication process adopted for Silicon Nitride islands is described in Figure 4.20. For Poly-Silicon the difference lies in the step E; when the wafer is dry-etched from the backside the etching does not go through Poly-Silicon as it goes through Nitride, but it stops at the beginning of this layer. Poly-Silicon and Silicon will be dry-etched together in the second etching process (G), giving the same final condition. In order to test more severe condition, for this process we designed a new topside mask, with bigger islands and lower interisland space (details have been already explained in Mask Design paragraph).

In this case we started with Silicon wafers without any thermal oxide on the surfaces. Zero-stress PECVD Oxide has been deposited on the top surface at 400°C (Figure 4.20 A); the thickness for this etch stop layer was set at 2 μm . After cleaning, 200 nm layers of Poly-Silicon for the first group, and of Silicon Nitride for the second one, have been deposited on the wafers. Same thickness of these two stiff materials can allow us to compare them both in terms of outcome and performances. After cleaning, rinsing in water and drying, wafers have been primed with TMSDEA and then HPR 504 resist has been spin coated at 4000 rpm, generating a 1.37 μm layer on the topside of each wafer. Lithography has been completed exposing the wafer for 7 seconds under the new topside mask and developing the resist. The stiff material on the front side has been dry-etched until reaching the 2 μm PECVD Oxide layer (Figure 4.20 C) and the resist has been removed using plasma at 130°C for 60 minutes (1000 W). Subsequently, 3 μm PECVD Oxide layer has been deposited on the backside (Figure 4.20 D). In order to start the second lithography process, wafers have been cleaned, rinsed in water, dried and primed with TMSDEA afterwards. HPR 504 resist has been spin coated at 1000 rpm on the backside, creating a 2.5 μm layer of resist. We exposed the wafer for 18.5 seconds under the backside mask and then we developed the resist. For the nitride wafers both the LPCVD Oxide and the Nitride have been dry-etched from the backside and the Silicon acted as etch stop layer (Figure 4.20 E). Conversely, for Poly-Silicon wafers, Poly-Silicon itself played the role of etch stop layer. In this case, as previously explained, just PECVD Oxide has been dry-etched from the backside. We removed again the resist in Plasma at 130°C and cleaned the wafers.

With the aim of creating the indentation in the membrane to avoid delamination, we deposited a layer of resist on the wafers topside that we patterned with the anti-delamination mask. After this step just a small amount of resist, in the surrounding of each islands, remained on the surface. This resist will be removed at the end of the fabrication process, leaving the indentation in the membrane completely empty. The

resist chosen for this application was AZ 4533, spin coated at 1000 rpm after priming the wafer with TMSDEA. The thickness of the resist was 7.87 μm , subsequently the anti-delamination mask has been reproduced on the top surface, exposing the wafers for 18 seconds and developing the resist (Figure 4.21).

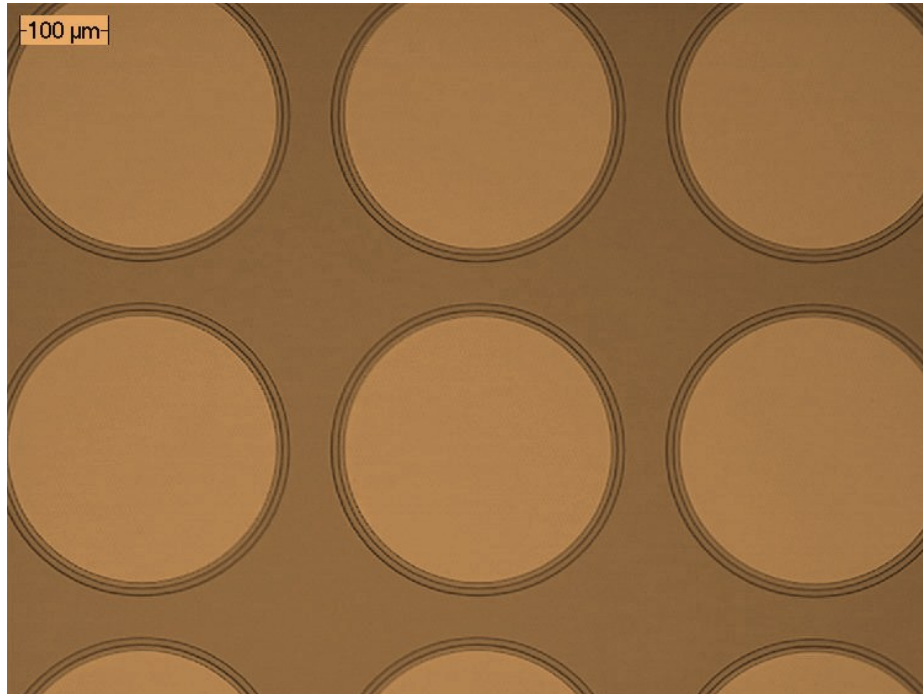


Figure 4.21 - Circle islands surrounded by a thin layer of resist. At the end of the fabrication process, once this resist will be removed, the indentation will remain in the membrane, reducing the strain in the PDMS around the islands as showed in the FEM paragraph

25°C plasma descum at 600 W for 2 minutes has been performed on the wafers before spin-coating PDMS (Sylgard 184 ® from Dow Corning, 10:1 ratio) at 3000 rpm in order to create a 20 μm elastomeric layer on top of the wafers. PDMS was cured in the oven at 90°C for 30 minutes and then 50 nm layer of Aluminum was deposited on top of PDMS at low power (125 W) and low temperature (Figure 4.20 F). For Nitride wafers, Silicon has been dry-etched from the backside stopping at the Zero-Stress PECVD Oxide etch stop layer on the top side (Figure 4.20 G); on the other hand both Poly-Silicon and Silicon have been etched for Poly-Silicon wafers. Compared to the first fabrication sequence, results showed a huge improvement; the elastomeric substrate remained flat and all of the membranes showed neither wrinkles nor cracks (Figure 4.22). Therefore, we proved the compressive stress in the Thermal Oxide layer was the reason of wrinkles and cracks that took place in the membrane after Silicon removal. Aluminum has been removed in the PES etchant (2 minutes at 30°C) then the holes have been filled in with Isopropanol before Oxide removal in the BOE bath (16 minutes of wet-etching) as indicated in Figure 4.20 H. The last step of this fabrication process consists in the removal of the resist in

order to leave the indentations empty, creating the anti-delamination shield around the islands (Figure 4.20 I). For this purpose we placed the wafers in Acetone to let the resist dissolve. SEM pictures have been collected showing Acetone was able to completely remove the resist, giving us the desired indentation in the membrane (Figure 4.23).

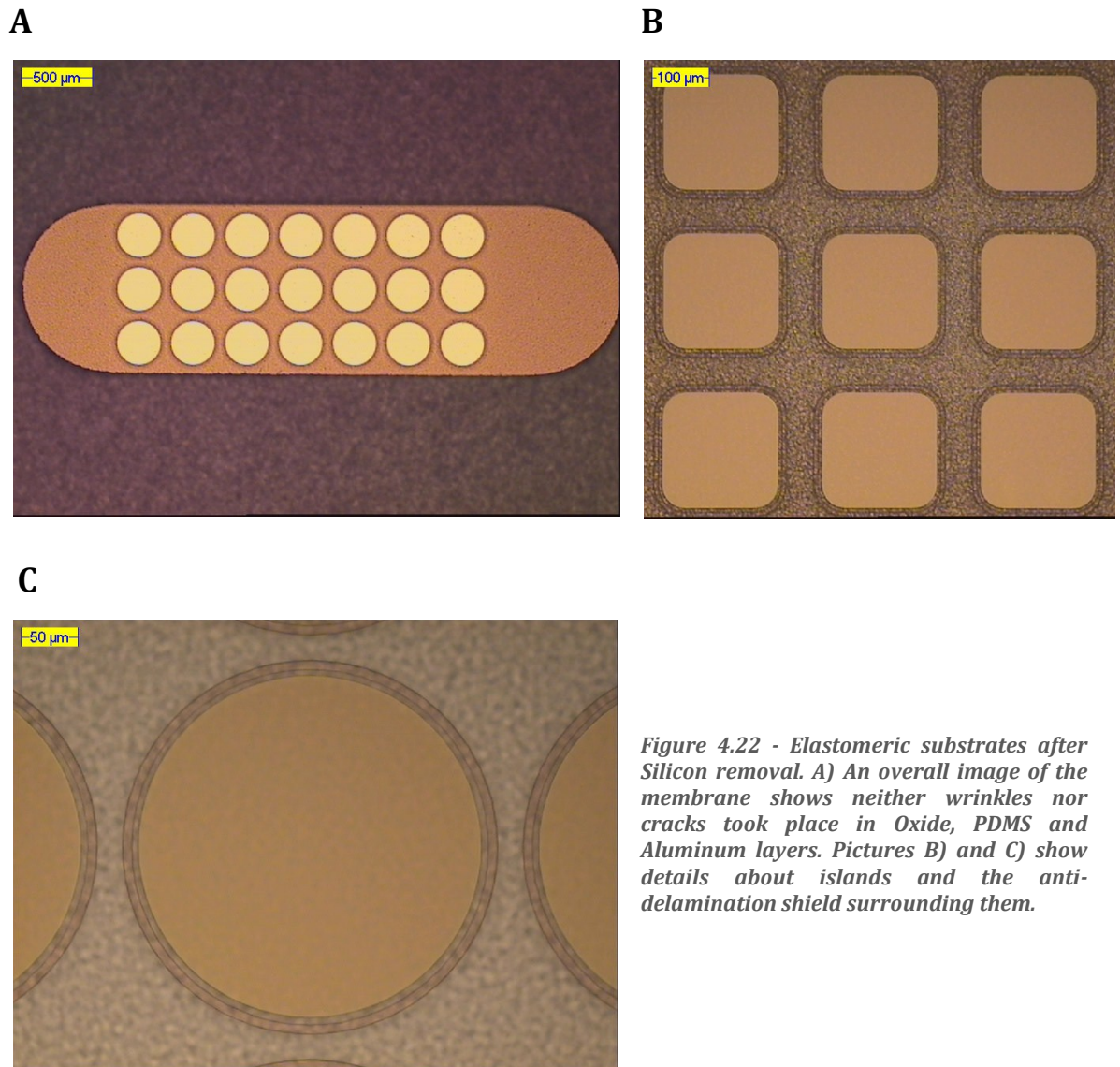


Figure 4.22 - Elastomeric substrates after Silicon removal. A) An overall image of the membrane shows neither wrinkles nor cracks took place in Oxide, PDMS and Aluminum layers. Pictures B) and C) show details about islands and the anti-delamination shield surrounding them.

This last fabrication process successfully faced the problems emerged after the previous one; devices were finally ready to be stressed under bulge test, evaluating their ability to stretch and inflate.

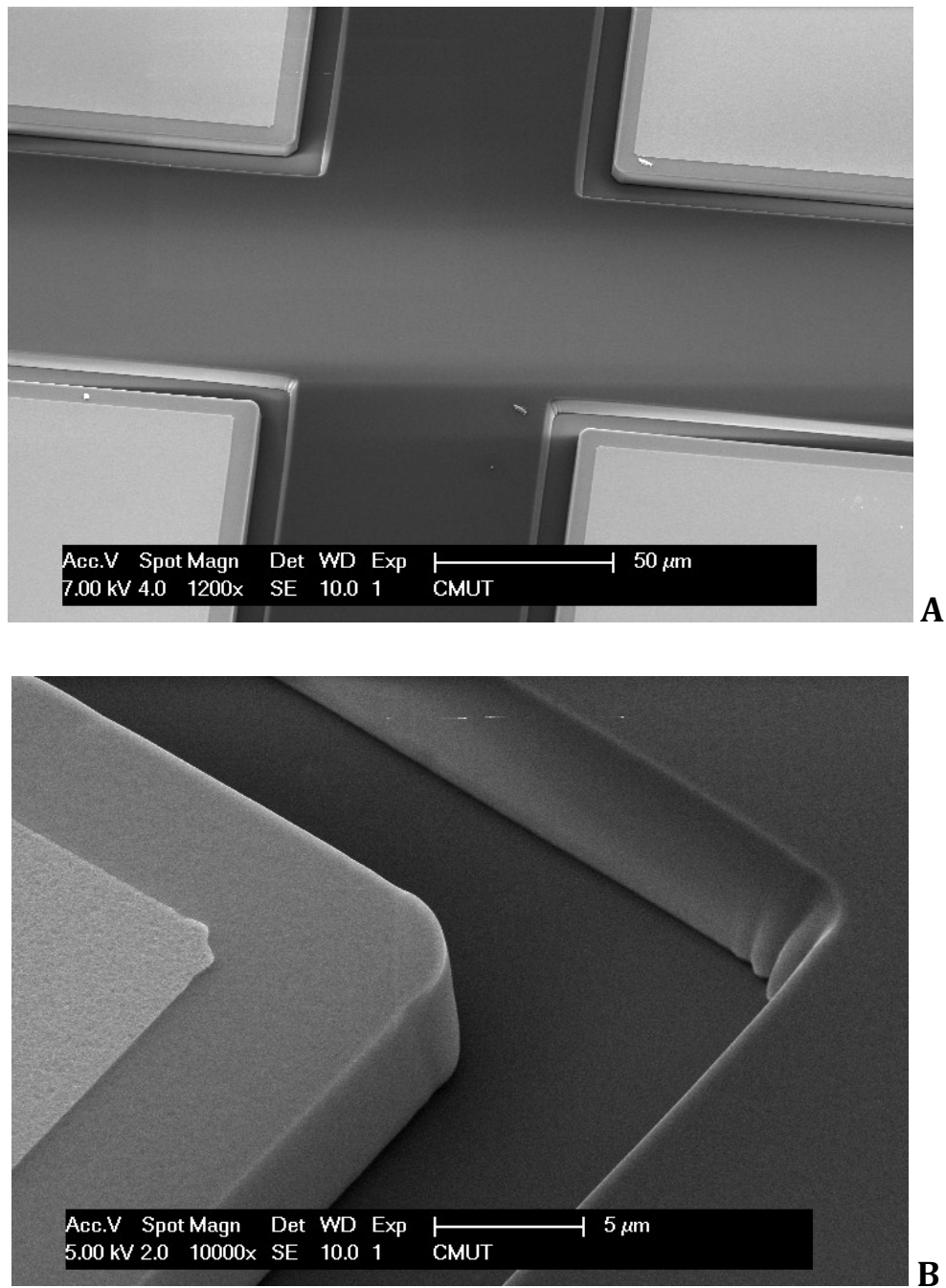


Figure 4.23 - SEM pictures of the anti-delamination shield surrounding the islands. A) An overall view of the islands surrounded by these channels. B) A detail of one corner; the island is surrounded by a small PDMS layer (5 μm length) before the indentation. The size of the indentation is 10 μm and its depth is 7.87 μm (the same thickness of the resist spin coated in the indentations and then removed with Acetone)

5. RESULTS

In this chapter we present and analyze the results from membrane inflation of the chips obtained after the fabrication sequence, previously introduced. Effects of different membrane thicknesses and islands shapes are reported and studied. Evidences in literature supporting our results are showed. Observations about the improvements offered by the anti-delamination structures we projected are then discussed.

5.1 EFFECTS OF PDMS THICKNESS

Two different thicknesses have been tested in order to assess how this parameter influences the mechanical behavior of the stretchable membrane. The desired thickness of PDMS is achieved adjusting the speed during the spin-coating phase. 20 μm and 80 μm thick elastomeric layers have been fabricated and then stressed under the same pressure conditions, comparing the inflation high of the membrane and then deducing the strain in the elastomeric substrate. We were interested in the phenomenon that takes place in the membrane under stress condition in order to find potential factors that contribute to the failure of the membrane. Further considerations can be made testing other membrane thicknesses; however a particular feature about spin-coating of PDMS on Silicon wafers needs to be considered. In fact, as showed in Figure 5.1, PDMS forms *edge bead* once deposited on Silicon. When its thickness become too high (over 100 μm), these edges become too big, preventing the anti-stiction layer of Aluminum to be correctly deposited on top of PDMS. Edge beads can be removed with several techniques, for this purpose some patents have been released; however this aim lies outside of this project.



Figure 5.1 : Locations of edge bead formed during the spin-coating of PDMS on top of the wafer

Same islands configurations with different thicknesses have been inflated with the same pressures, recording the inflation high of the membrane and analyzing the behavior of the device. Before every test, samples have been pre-loaded. The results from the inflation tests are reported in Table 5.1 and summarized in Figure 5.2. These results show quite clearly the effect of the membrane thickness: the higher is the thickness of the membrane, the lower is the inflation high (and also the strain of PDMS) the membrane reaches when the same level of pressure is applied. The strain in PDMS is deducted using the formula previously deducted in the Bulge Test paragraph. This approximation works when the inflated membrane can be considered as a circumference arc. For inflation high higher than the membrane radius (half of the

membrane length), this assumption is no more valid. For these values, in Table 5.1, just the inflation high has been reported.

APPLIED PRESSURE [KPa]	20 μm PDMS MEMBRANE		80 μm PDMS MEMBRANE	
	INFLATION HIGH [μm]	NORMALIZED STRAIN IN PDMS	INFLATION HIGH [μm]	NORMALIZED STRAIN IN PDMS
15	430	68,48 %	215	17,12 %
20	493	90,01 %	246	22,41 %
25	539	107,60 %	274	27,80 %
30	583	125,88 %	298	32,89 %
35	606	--	323	38,64 %
40	631	--	342	43,32 %
45	648	--	365	49,34 %

Table 5.1 - Results of the inflation tests to compare the inflation high and the strain occurred in PDMS for the same island configuration, with two different membrane thicknesses. When the inflation high is higher than the membrane radius (600 μm), the strain in PDMS cannot be approximated anymore with the formula from [11]

However, the inflation high trend has been extended also to these last pressure levels, in order to make a comparison with the trend of the thicker membrane.

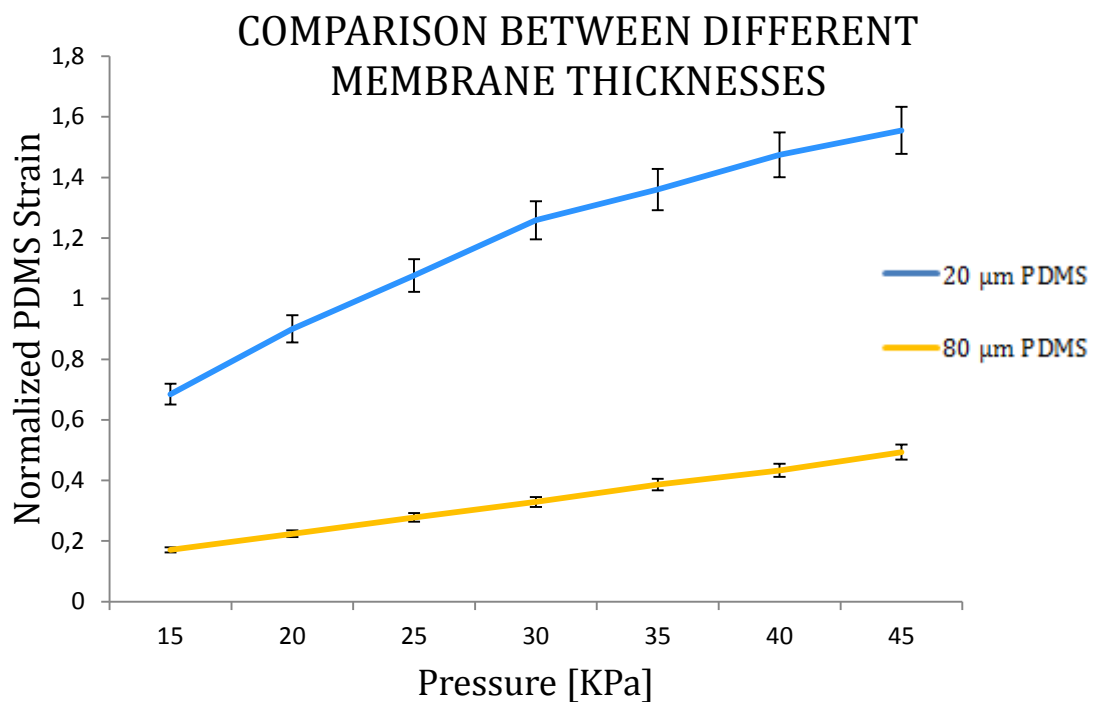


Figure 5.2 - Strain-trend in PDMS for two different membrane thicknesses when the same pressure is applied to the same islands configuration. Vertical bars indicate the standard deviation out of 15 measures

The overall membrane showed able to withstand strains higher than 100% without breaking. Also the islands showed no crack; this happened because almost all the strain

was accommodated by the PDMS, as we already supposed from FEM simulations. The inflation test also showed that the adhesion between stiff islands, both in Poly-Silicon and in Silicon Nitride, and PDMS was very good; none of the islands detached from the substrate under pressure.

By applying excessive back pressure on the thin membrane, scratches started to appear in the PDMS, especially in the regions between the islands, the same regions that are accommodating higher strain, as already discussed (Figure 5.3). These scratches remained confined at a surface level, without propagating through the whole PDMS surface, causing the membrane to crack.

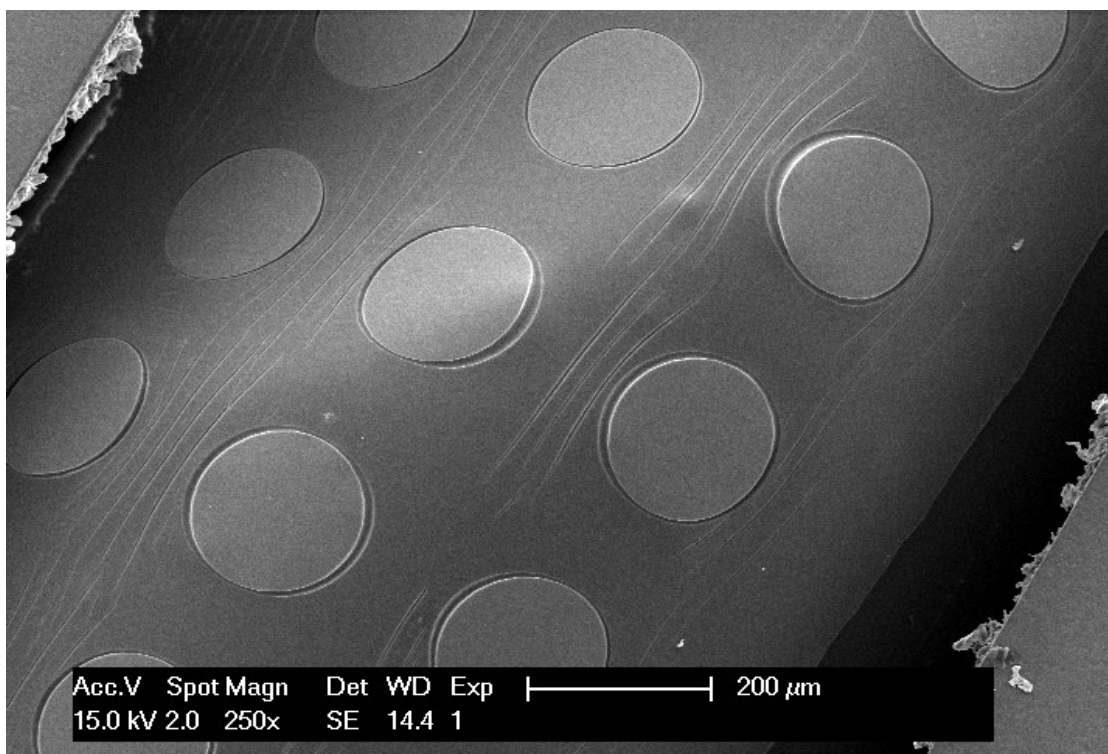


Figure 5.3 - SEM pictures of PDMS scratching in the regions between the islands

This behavior has been noticed exclusively for thin membranes and not for thicker ones. The first explanation possible is that thicker membrane requires higher pressure to reach the same amount of PDMS strain. Examining this topic further, we applied higher pressure (more than 80 KPa) to the thicker membrane, to see if these scratches start to appear. The evidence that also for higher pressure this phenomenon didn't take place finds a literature support from Liu [32] as explained in Figure 5.4.

According to the research from Liu, thinner membrane can withstand higher stresses; however they fail for lower strains. This theory can support the evidence that thicker layers didn't show scratches even when, applying higher pressure, we were able to

reach almost the same amount of strain that cause scratches in thinner PDMS membranes.

This first set of results provided some guidelines choosing the ideal thickness of the device. This decision can be related to the application of the stretchable MEA. If its membrane is conceived to be exposed to high pressure levels without compromising its functionality, thick membrane can represent the correct option. In fact the strain in this membrane will be

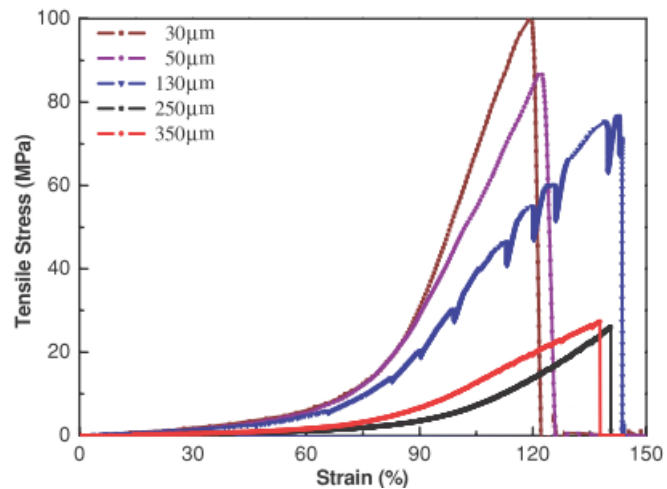


Figure 5.4 - True stress versus true strain of PDMS membrane with different thicknesses [32]

lower, preserving the PDMS from scratching. On the other hand, if the membrane has to reach high values of deformation, for example in case it has to be inflated, growing cardiomyocytes deposited on its surface (as explained in the next chapter), thinner substrates are preferable. Lower pressure will be required, also reducing the energy consumption.

5.2 EFFECTS OF ISLANDS' SHAPE

To test how the islands' shape affects the behavior of the membrane, structures with the same dimension and interisland space, but different shape, have been studied. What we observed analyzing the FEM simulation in Chapter 3 was that, increasing the ray of the corners, we can reduce the peak-strain in the membrane, usually located in the region surrounding the islands (Figure 3.7). In terms of peak strain, circle islands seem to offer the best solution. On the other hand squared islands of the same dimension offer a higher surface, able to accommodate more circuitry. According to these premises rounded square islands offer a good compromise between these two factors. However, inflating the membrane of different island shapes revealed interesting outcomes. As we can see comparing Figure 5.6 and Figure 5.7, circle islands show a delamination from their substrates extremely higher compared to the one of square islands. A good explanation of this phenomenon is provided analyzing the FEM simulation performed by [19] and represented in Figure 5.5.

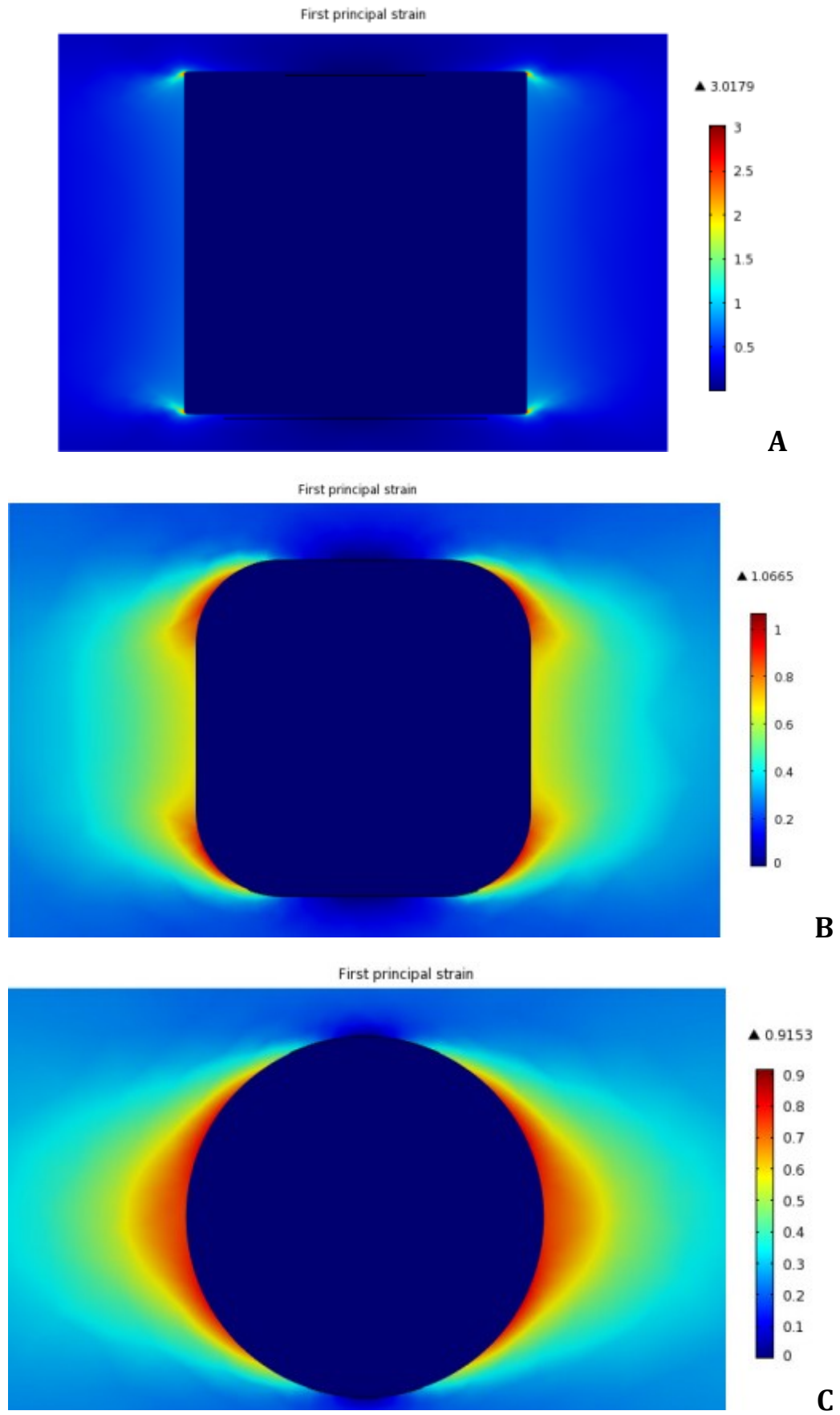


Figure 5.5 - Distribution of the first principal strain in the PDMS membrane surrounding the island according to the island shape [19]

On the one hand circle islands (Figure 5.5 C) show a lower peak strain than the square ones (Figure 5.5 A), under the same stress condition. On the other hand the distribution of this strain strongly affects the delamination from the substrate.

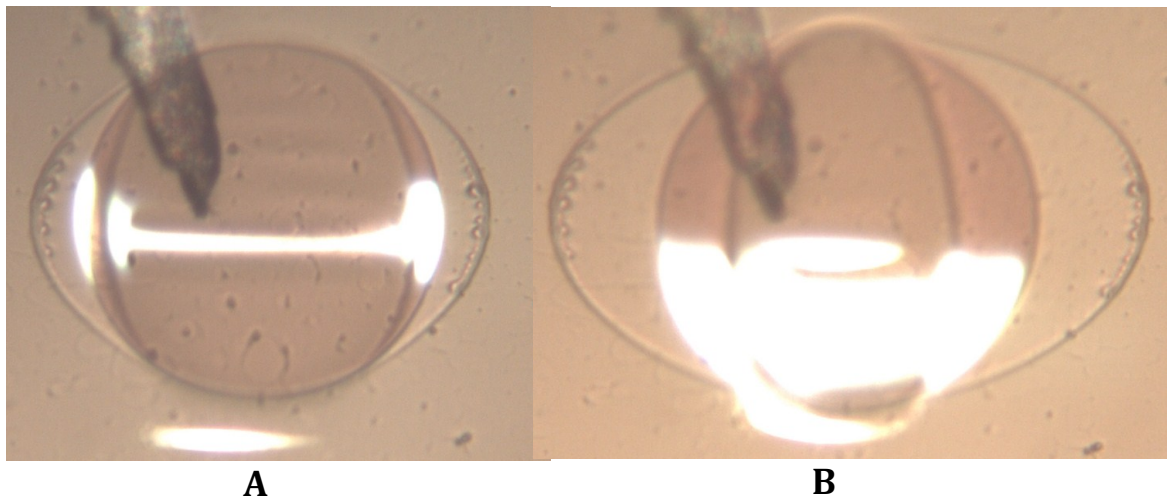


Figure 5.6 - 300 μm Nitride circle island inflated by 65 KPa (A) and 80 KPa (B). Huge delamination from the surrounding membrane took place

Notwithstanding the strain in the membrane surrounding the squared island is higher, this strain is confined in a small region around the corners of the island. Conversely, in circle island the high-strain region embraces a huge area on both side of the circle, the same area in which we can observe a huge delamination in Figure 5.6 B.

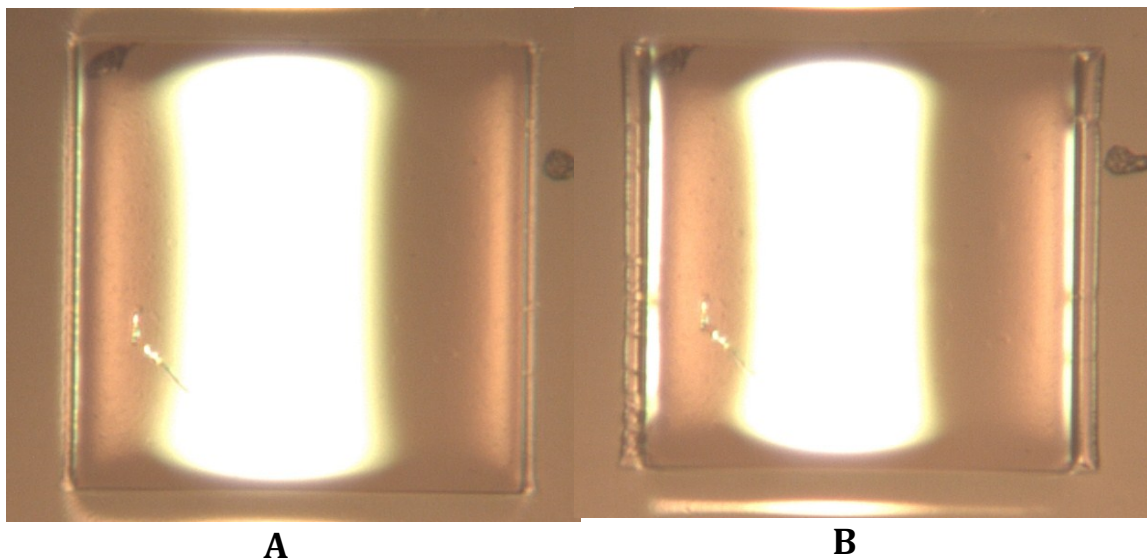


Figure 5.7 - 300 μm Nitride square island inflated by 65KPa (A) and 80 KPa (B). Delamination is quite confined

Two main reasons make island delamination from its substrate a tricky problem. The first reason is that it can cause the island to detach from its substrate, losing the

contribution that can be provided by future electronics that is going to be placed on it. The second reason is that future interconnections can detach from the islands or even break, compromising their functioning. For this reason we also implemented an *anti-delamination* structure, made by empty channels in the membrane surrounding the islands, with the aim of accommodating and reducing the strain in these regions, as discussed in the FEM paragraph.

5.2.2 EFFECTS OF ANTI-DELAMINATION STRUCTURES

As expected from the simulations previously performed and showed in chapter 3, the anti-delamination structure improved the behavior of the device, reducing the phenomenon of islands detachment.

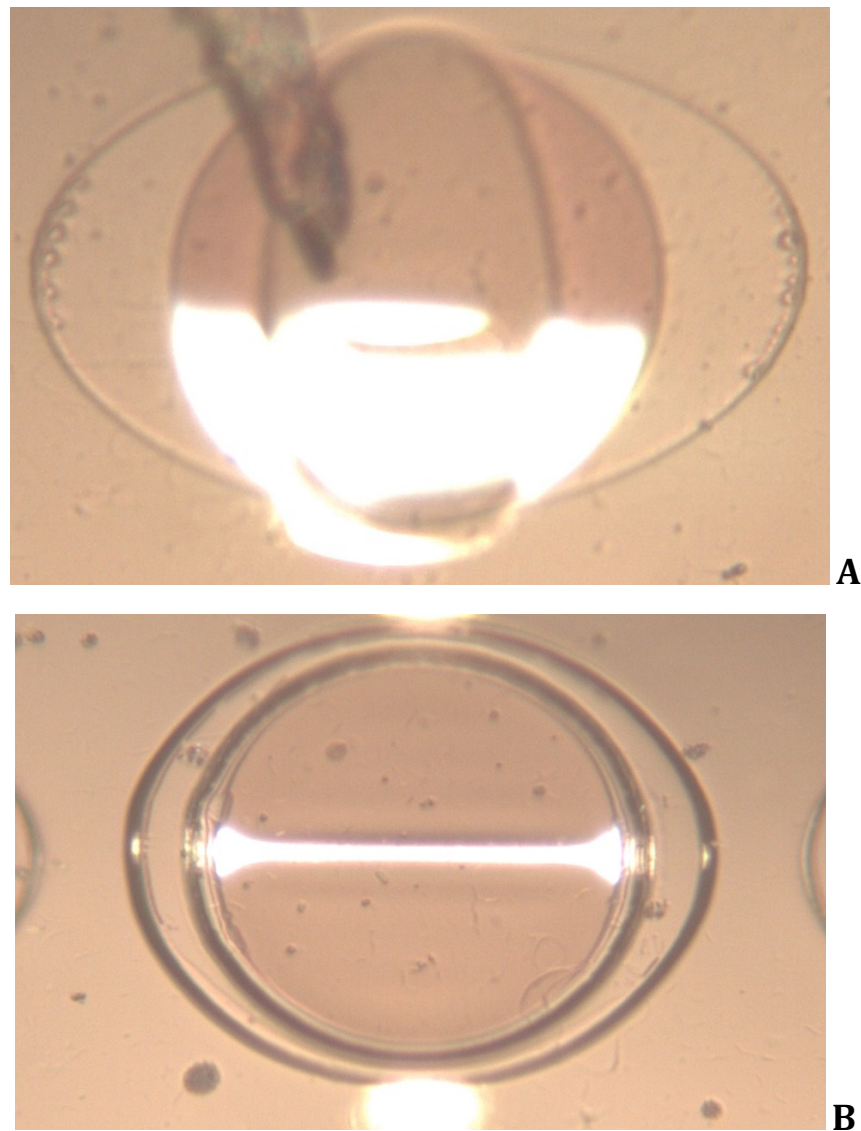


Figure 5.8 - Circle island (300 μm) with (B) and without (A) anti-delamination structure. Same pressure is applied (80 KPa). The anti-delamination shield proved to reduce significantly this phenomenon

Figure 5.8 compare the same island with (B) and without (A) anti-delamination shield. All the configurations have been compared, showing important improvements in the reduction of this phenomenon.

6. APPLICATIONS OF STRETCHABLE ELECTRONICS

In this chapter the biomedical background of this project is highlighted. Realization of electronics with performance equal to established technologies that use rigid semiconductor wafers, but in lightweight, foldable and stretchable formats would enable many new applications [4]. We face the realization of a stretchable multi-electrode array for cardiotoxicity drug screening applications. The paragraph starts taking into account the problem from the biomedical perspective, then technological solutions are studied and first results referring to cells' behavior on the substrate are presented; these results offer a prove of the advantages a stretchable MEA can provide in place of a traditional rigid MEA. Finally, applications of stretchable electronics for implantable devices are showed; these applications mostly refer to neuroprosthesis implants, such as cochlear and retinal prosthesis and deep brain stimulation probes. They will be briefly introduced, focusing on improvements they can benefit from stretchable electronics.

6.1 STRETCHABLE MEA FOR CARDIO-TOXICITY DRUG SCREENING APPLICATIONS

In recent years, several drugs have been withdrawn from the market. Terfenadine, used to treat allergic rhinitis (hay fever), is one of the best known example. After being on the market for almost 15 years, the drug was withdrawn as it became evident that it can induce serious ventricular tachyarrhythmia [58]. This is not the only case of drug withdrawn: Vioxx (2004) [59], Adderal XR (2005) [60] and Pergolide (2007) [59] are some other meaningful examples in this field. For Vioxx, by the time the danger was discovered, the medicine had already been taken by thousands of people [59]. It is becoming increasingly clear that drugs can pass all of the present regulatory requirements and be authorized for prescription to patients or even sold “over the counter” for many years before rare and lethal adverse effects become apparent [58]. The need of new devices able to integrate current drug screening methods, providing more reliable outcomes, is clear. In this paragraph we consider a stretchable Multi-Electrode Array (MEA) for drug screening applications. We start presenting the state of art, considering the actual limits of in-vivo models. Ventricular tachyarrhythmia, responsible of many drug withdrawals, is often the result of ion channels dynamics alteration; we distinguish genetic and acquired diseases and highlight how pathological functioning of the ion channels can lead to these abnormalities. Human cardiomyocytes revealed as a potential target for in-vitro drug screening application; we discuss the ways to get these cells through stem cells biology techniques. The properties of a MEA conceived for drug screening application will be listed, and then we focus on the improvements a stretchable device can hold, compared to a traditional rigid one. Protocols developed in literature for drug screening procedure using MEAs are presented. We conclude proposing technological solutions for cells alignment on the stretchable MEA membrane. Finally, we present the results of experiments conducted by Leiden University Medical Center in collaboration with Philips Research. These analyses investigated the behavior of cells cultured on both rigid and stiff substrate; they offer an important highlight comparing stretchable and rigid multi-electrode array.

In-vivo and in-vitro models

The use of stem cells to discover new pharmaceuticals rather than only as therapeutics is possibly among the most significant conceptual changes in stem cell biology of the past decade. Cells of the heart are of particular interest because prolonged function of this organ is crucial to human health and yet can be jeopardized by malfunction of just one cell type – the cardiomyocytes [61]. Experimental animals, such as the mouse,

guinea pig, rabbit and dog, cannot completely model human cardiomyocytes [61, 62]. These in-vivo approaches share high costs and ethical implication, besides it is not easy to extrapolate the results obtained from such models to humans [63]. As we can notice In the example reported in Figure 6.1, humans exhibit significant differences in cardiac electrophysiology when compared with mice [61]; in fact these animals have a much shorter cardiac AP that lacks a clear plateau phase.

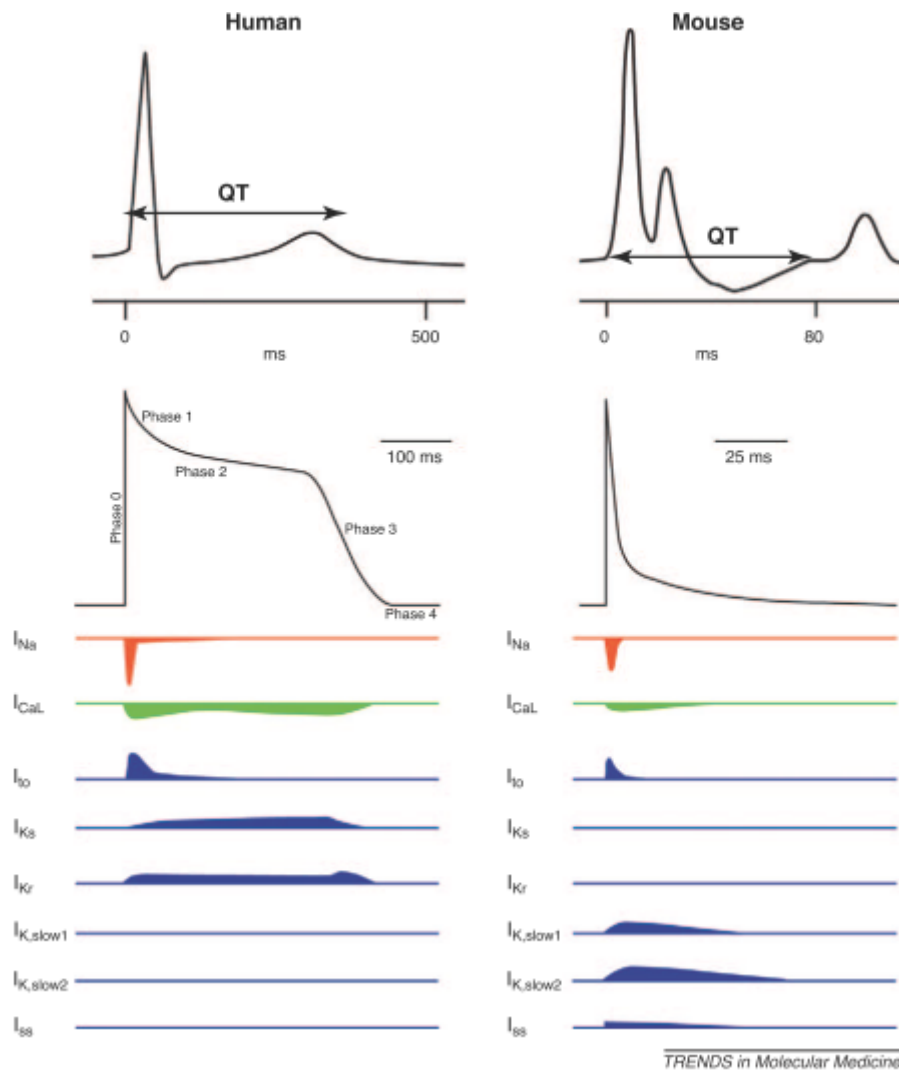


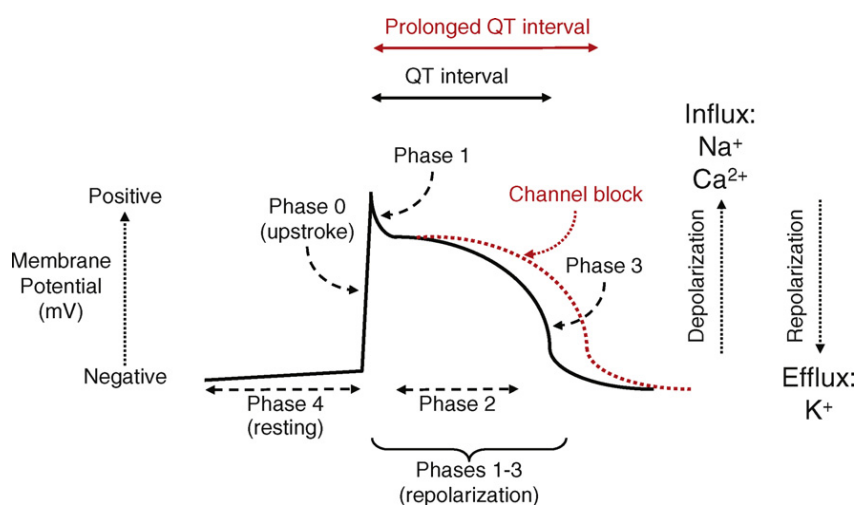
Figure 6.1 - Electrophysiological differences between adult human and mouse CMs. Human and mouse hearts display unique ECG profiles, with the QT interval in humans approximately five times longer than in mice. This is also reflected in the different AP durations and shapes of the ventricular CMs from these two species and is due to their instinctive ionic currents. Although the inward Na^+ and Ca^{2+} currents (I_{Na} and I_{CaL} , respectively) are comparable between mouse and human CMs, major differences are observed in the various outward K^+ currents (in blue), which play distinct roles in human and mouse AP repolarization. The I_{Ks} and I_{Kr} are the major repolarizing currents in human CMs, whereas in mice I_{to} is the predominant current. Additionally I_{Kslow1} , I_{Kslow2} and I_{ss} contribute to repolarization in mouse CMs, but are absent from human ventricular CMs. The APs and their underlying ionic currents are aligned with their approximate time of action during the QT interval shown in the ECG examples. (ms, millisecond) [61]

Alternatively to in-vivo strategy, several in-vitro models are currently used in the process of cardiovascular drug development testing, and toxicity screening [64].

In the field of cardiac electrophysiology, these models are aimed at assessing the potential efficacy of different antiarrhythmic compounds on one hand and on determining the potential pro-arrhythmic risk of other pharmacological agents on the other hand. While the existing models for target and/or toxicity screening are well-characterized, extensively studied and widely accepted by the academia, drug developers and regulatory agencies, none of them utilizes human cardiac cells. Hence, development of an in-vitro model that is based on human cardiac tissue has the potential to bring an additional value for electrophysiological drug testing as well as for different patho-physiological studies.

Screening through ion channels dynamics

Ion channels are pore-forming, transmembrane proteins that establish and control voltage gradients through the selective and directional flow of ions [61]. The balance between depolarizing and repolarizing ion currents through these specialized channels creates the “action potential” (AP) in electrically active cells such as cardiomyocytes. The AP essentially determines the electrical activity of the heart, although conduction and propagation through the myocardium depends on the electrical coupling between cells, mediated by gap junctions. Mutations in genes encoding any of these proteins can cause abnormalities in ion channel function or cell-to-cell electrical coupling and can evoke life-threatening cardiac arrhythmias that can evolve into ventricular fibrillation, the most common cause of sudden cardiac death.



Drug Discovery Today: Therapeutic Strategies

Figure 6.2 - QT-interval Prolongation shown on the cardiac action potential [64]

Syndromes resulting from ion channel mutations are termed congenital cardiac channelopathies and, depending on the gene affected, include Brugada disease, long QT (LQT), short QT (SQT) and catecholaminergic polymorphic ventricular tachyarrhythmia (CPVT). They are often caused by single genetic mutations that result in distinctive abnormalities evident on an ECG.

QT interval refers to the the duration of ventricular depolarization and subsequent repolarisation, measured from the beginning of the QRS complex to the end of the T wave of the heart rhythm as measured by the body surface ECG (Figure 6.1). LQT, the most common electro-physiological disorder, has 12 different sub-types. It is characterized by prolongation of the AP duration (APD) (Figure 6.2) and results in an extended QT interval on an ECG. Mutations in the genes encoding potassium (KCNQ1, KCNH2), sodium (SCN5A) and calcium (CACNA1C) channels are the most common cause of the syndrome, which is usually inherited in an autosomal dominant manner. In the long QT syndromes, malfunction of ion channels may be not only the result of gene mutation, but also may be “acquired” (i.e. caused by metabolic abnormalities or drugs) [65]. Moreover, the vast majority of drugs that result in QT prolongation have been demonstrated to block the α subunit of the I_{Kr} channel (see Figure 6.1), which is encoded by the human ether-à-gogo-related (hERG) gene [64].

Prolongation of QT interval is an important determinant for the development of Torsade de Pointes (French for “twisting of the points”) characterized by QRS complexes that seem to be “twisting” around an imaginary axis because of their changing amplitude and contour [65].



Figure 6.3 - Typical pause dependent Torsade de Pointes (TdP). The tachyarrhythmia is preceded by ventricular bigeminy, creating a series of “long” and “short” cycles (marked L and S). The long QT interval is difficult to appreciate because the extra-systoles conceal the terminal part of the QT segment. [65]

Torsade de Pointes has become the single most common cause for the withdrawal or the administration of restrictions on the use of previously marketed drugs [64]. This kind of disease should represent a target while designing a protocol with the aim to evaluate drugs.

Stem Cell models for cardiac disease

Several tests are based on isolated cardiac tissues. These include Purkinje fibers, papillary muscles and ventricular trabeculae from animals. None is yet versatile and predictive enough to convince regulators that a drug that does not adversely affect these tissues be regarded as safe. The regulatory authorities usually require more complex in-vivo telemetry studies in larger animals like dogs and pigs (International Conferences of Harmonization has approved guidelines S7B and E14 [62]). Nevertheless, it is still not possible to quantify risk/benefit assessment for TdP liability accurately on the basis of the current preclinical assays. This is where cardiomyocytes derived from human pluripotent stem cells may be useful. These cells have a significant potential to be developed into a model with a relatively high predictive value for cardiac safety pharmacology. These are human cells and, as far as we can tell, they can share many features of human adult ventricular cardiomyocytes and can in principle be scaled up to reproducibly produce large cell numbers [58].

Since the first derivation of human Embryonic Stem Cells (hESCs) from normal embryos in 1998, the possibility of using these cells to model human genetic diseases has existed. However, initial difficulties in genetically modifying hESCs and the ethical and legislative issues associated with destroying surplus embryos during derivation restricted research in many countries and limited their use among the wider research community. The discovery that adult somatic cells could be reprogrammed to a pluripotent state by the overexpression of four transcription factors (Sox2, Oct4, c-Myc and Klf4) was a breakthrough in stem cell biology that has resulted in many new groups entering the field. Although human induced Pluripotent Stem Cells (hiPSCs) might not be epigenetically identical to hESCs [61], they clearly self-renew and are pluripotent. PSC models for monogenetic disease can be developed using hESCs derived from diseased embryos or by introducing the variant sequence into the gene. Alternatively, the genetic variant could be corrected in the patient-derived hiPSCs. One of the major challenges in PSC research is to develop reproducible and robust differentiation strategies to derive desired cell types in sufficient quantities for downstream analysis. In the present context, this means first to cardiogenic mesoderm, then to cardiac progenitors and finally to functional cardiomyocytes. Presently, as reported by [61], there are three predominant strategies to differentiate both hESC and hiPSCs to cardiomyocytes: coculture which are END-2 stromal cells, embryoid body differentiation and monolayer differentiation.

Four main observations regarding to these techniques need to be discussed:

- The maturation of the PSC-CMs derived needs to be considered. PSC-CMs typically have an immature phenotype, with a gene expression profile resembling that of fetal cardiomyocytes (comparable to 16-week-old fetal hearts [66]). Additionally, they present less negative resting membrane potentials; lower upstroke velocities and smaller AP amplitudes compared with adult cardiomyocytes, and their sarcomeres and shapes are relatively disorganized and not aligned as in adult cells. Although for many applications an immature PSC-CM model might still offer an improvement over traditional model systems, it remains a challenge to understand and recapitulate *in vitro* the physiological and biochemical triggers active in normal development.
- During assay development, it should also be remembered that the heart is not only composed of cardiomyocytes (~30% of the total cells present) but also two other principal cell types: cardiac fibroblasts (~60%) and vascular endothelial cells (~10%). Although most electrophysiological (EP) disorders and cardiomyopathies directly affect cardiomyocytes, for other cardiac diseases these other cell types might also influence cardiomyocyte function. Additionally, many electrophysiology assays rely on isolated single cardiomyocytes. Maintaining the myocytes in this format might alter their cellular function and does not take into account the intercellular electrical coupling of cardiomyocytes in the heart [61].
- iPSCs have been reported to retain an epigenetic memory of their somatic cell source with a tendency to differentiate more efficiently to lineages of the donor cell. However, this residual memory does not appear permanent, as continuous cell division appears to equilibrate the differentiation capacity of iPSCs derived from different tissue sources [61].
- Inside a population of cardiomyocytes derived from stem cells, cells can be designated as ventricle-like, atrial-like, or pacemaker-like based on the shape of the AP defined considering several parameters, such as AP duration, amplitude and maximal repolarization. Most of the experiments conducted showed ventricle-like as predominant group (more than 90% of the cells population) [66, 67]. This outcome is particularly suitable for drug cardiotoxicity screening, because ventricular-like APs show a plateau phase that results in longer repolarization compared to the more triangular shaped, atrial like APs. Pacemaker-like cells are characterized by slow upstroke velocities and smaller amplitudes [67].

Multi-Electrode Array

Although patch clamp studies can provide important and detailed information regarding the ionic currents and AP properties of individual cardiomyocytes, it is a relatively low throughput procedure and does not allow assessment of multicellular preparations [64]. The MEA mapping technique enables stable and long-term recordings of extracellular field potentials from cardiomyocyte cell cultures at a high spatiotemporal resolution [64]. MEAs represent a novel tool for functional analysis of cell-to-cell interactions in electrogenic tissues, enabling to detect the origin, direction and propagation velocity of the excitation spread in the clusters of ES cell-derived cardiomyocytes (see Figure 6.4). Furthermore, as showed by [64], cardiac Field Potential Duration (FPD) on MEA corresponds with QT interval properties in electrocardiogram. This evidence candidates the MEA approach as a reliable way to study drug induced tachyarrhythmia on cardiomyocytes cultures. Improvements related with a stretchable MEA, compared to a traditional rigid one, lie in three main points. A stretchable MEA is based on biocompatible PDMS in place of glass; as showed in next paragraphs, the use of this material improve the growth of cardiomyocytes placed on its surface.

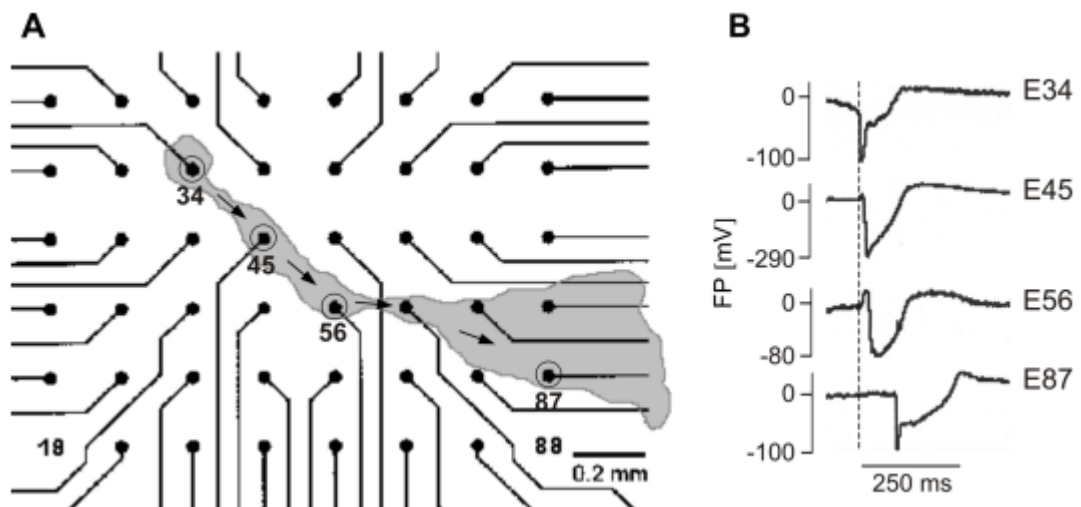


Figure 6.4 - Field Potential recordings from a cardiomyocyte cluster within an Embryoid Body plated onto a MEA. A) elongated beating cell cluster at day 6 after plating the EB. Direction of contraction spread (microscopic observation) is shown by arrows; recording electrodes are marked as circles. B) synchronous recordings from electrodes labeled in A. The sequential increase of delay between spikes registered at electrodes 45, 56, and 87 versus electrode 34 confirms the direction of the excitation wave indicated by arrows in A. Data retrieved from the research of [68]

Moreover, on a rigid MEA there is no possibility to stretch the cells and simulate the strains in a normal beating heart which is very important since, first of all it is known that certain cardiotoxic effects of drugs may only become evident under conditions that simulate a normal beating heart, in either physiological (stretch-contraction cycle) or pathological situation (e.g. excessive stretch). Finally, differentiated cardiomyocytes

derived from stem cells are immature compared to the cells present in the adult human body and mechanical stimulation is expected to help them to mature better [63].

Dimensions of MEA, in terms of number of electrodes placed on the platform, are strongly related to the application of the device. For neurophysiological studies, for example, MEA are typically 1024x1024 electrodes. Almost all the approaches in drug screening applications involve smaller MEA (Figure 6.5), made usually by 60 electrodes [1, 64, 68].

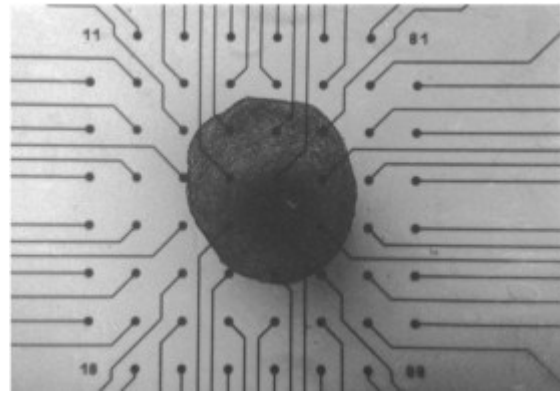


Figure 6.5 - Freshly placed Embryoid Bodies on a 60 electrodes MEA [68]

Protocol overview

With the aim to define a protocol investigating drugs' effects on a stem-cell-derived cardiomyocytes culture placed on MEA, several steps need to be accomplished in order to provide effective results.

As described by [64], pluripotent hESC can be grown in the undifferentiated state on top of mouse embryonic fibroblast feeder layer. Once the differentiation process has been started, the EB can be plated on gelatin-coated culture dishes. The minute contracting areas take place (usually in 5-20 days of plating), they can be plated on top of fibronectin coated MEA plates. MEA data acquisition system can now start to recorder field potentials generated by contracting areas. Supposing a 60 electrodes MEA, as previously discussed, these field potentials can be recorded simultaneously from all 60 electrodes at a sampling rate of 25 kHz [64] and then band pass filtered from 1 to 10 kHz (all measurements need to be performed at 37°C). The field potential duration, determined at each electrode, served as measure for the local electrocardiogram QT interval, as previously discussed. FPD measurements can be normalized to the beating rate of the contracting areas, $cFPD$, using the Bazet's correction formula $\left(cFPD = \frac{FPD}{\sqrt{RR\ interval}}\right)$. To assess the effects of conduction, the local activation time at each electrode can be determined using the timing of the maximal negative time derivative of the signal at every unipolar electrode.

Cardiac FP averaging can yield higher-quality signals than original individual FPs, and therefore promise more accurate detection of different phases and analysis of the

cardiac FP signal, improving the quality of the FP recorded by the MEA. Averaged signals improve the signal-to-noise ratio (SNR) reducing noise to 1/6 of its original level, and provide reliable averages; this procedure requires approximately 50 cardiac cycles, as showed by [69]. This result was achieved detecting appropriate peaks in the imported signals that serve as reference points for aligning the cardiac FP cycles for average calculations. This technique proved its efficacy even in the detection of drug-induced changes in signal shape, comparing the situation before and after the introduction of drugs inside the cell culture.

Different drugs can now be administrated to the culture. Extracellular recordings need to be performed for 30s at baseline and at 5 min following drug application. Several drugs that can be tested on the cell culture are listed in Table 6.1. Interesting comparison can be made between the results obtained and the ones already reported in literature. It is well established that the three key ingredients in the development of slow conduction are reduction in excitability, decrement in cell-to-cell coupling and alteration in tissue architecture. hESC-CM model can assess the possible effects of different pharmacological agents on the former two properties [64].

DRUG	DESCRIPTION	EXPECTED EFFECTS
VERAPAMIL	L-type Ca ²⁺ channel blocker	Arrhythmic spiking [68]
TETRODOTOXIN (TTX)	Na ⁺ channel blocker	Concentration-dependent intermitted AP propagation block [68]
SPARFLOXACIN	hERG channel blocker	Conduction blocks or arrhythmia-like ventricular fibrillation [68]
E-4031	I _{Kr} blocker	Stages of phase 3 repolarization are affected, resulting in a prolongation of the APD. No effects in the earlier phases of the AP [64]
SOTANOL	I _{Kr} blocker Class III antiarrhythmic agent	Significant increase of cFPD [64]
PROPafenONE	Class IC antiarrhythmic agent	Total activation time is prolonged [68]

Table 6.1 : List of drugs administrated to cardiomyocytes cultures available in literature. Results achieved from different research groups are described

The schematic of the overall drug screening set up based on a stretchable MEA, proposed by [1], is depicted in Figure 6.6. In this picture the reader can find all the elements discussed in this chapter.

Human embryonic stem cell derived cardiomyocytes have the potential to be developed into a reasonably inexpensive, predictive human cardiac safety pharmacology model. This may allow researchers to perform drug discovery research and cardiac safety pharmacology in parallel. The outcomes of each process can inform the decision making in the other, ultimately leading to more effective drug development [58]. In the following subparagraph we discuss technological issues regarding cell alignment on the elastomeric membrane.

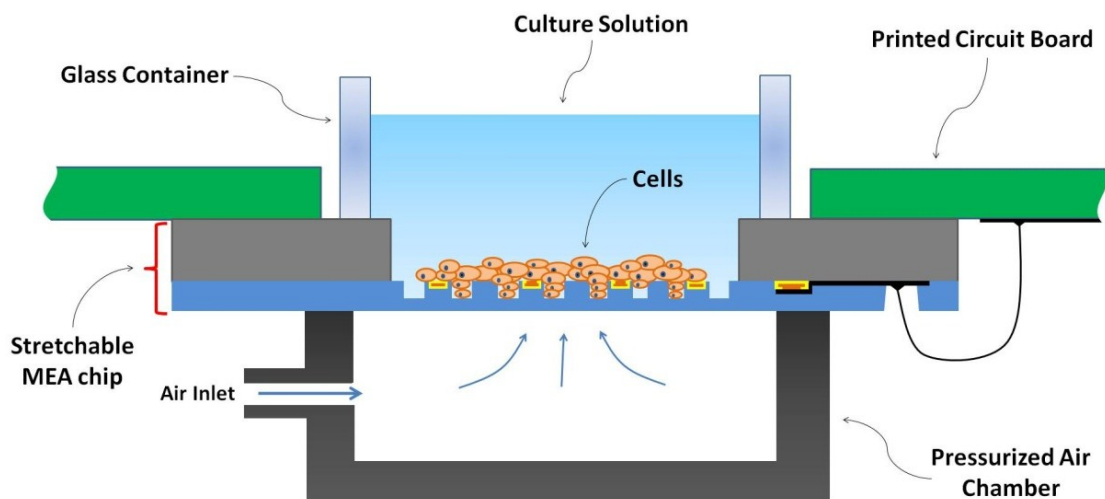


Figure 6.6 - A configuration for the overall set-up for drug screening proposed by [1]

6.1.1 PATTERNING CELLS ON THE MEMBRANE

The alignment of the cells on the device is important since the cardiomyocytes should be uniaxially aligned to provide a directional contraction which can be studied as is the case in the heart tissue [70]. Two major categories of methods for cell alignment exist in the literature, namely, lithographic alignment and topographical alignment [71]. In lithographical methods, the surface characteristics of the substrate are altered according to a pattern providing different conditions for the cells, for example different degrees of cell adhesion. This patterning of the substrate properties can be done by soft lithography (Micro-contact printing) and photolithography [71-73]. In topographical methods, 3D micro structures are formed in the substrate which affects the growth, orientation and activities of the cultured cells [70, 71, 74, 75]. Here the focus is on the cardiomyocytes, so methods more relevant to this line of cells are reviewed.

Lithographical alignment

Coating of MEAs with various materials is used for improving the attachment and growth of cell cultures. Fibronectin is an extracellular protein which is often used to promote the adhesion of (heart muscle) cells [5].

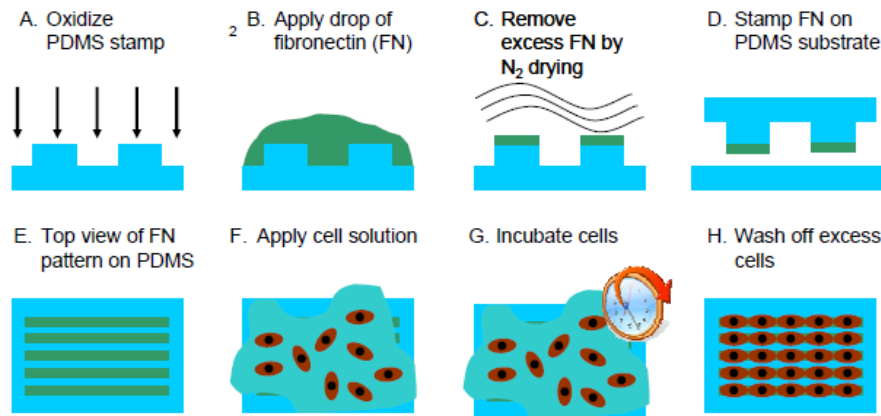


Figure 6.7 - Micro-contact printing for cell alignment procedure [76]

By patterning the fibronectin coating on the device into stripes the cells tend to align themselves with the direction of the stripes over time. In micro-contact printing a PDMS stamp is used to form these patterns on the substrate [70, 72]. The PDMS stamp - usually made by casting PDMS against a photo-resist or silicon mold of the same pattern desired - is first dipped in fibronectin and then pressed against the substrate upon which the stamp pattern is transferred to the substrate. In order for the fibronectin to adhere to the substrate and form a good pattern careful adjustment of the substrate water contact angle should be performed which is usually done by treating the substrate with an oxygen plasma or UV/ozone [73, 77]. After fibronectin pattern transfer the solution containing the cells is added and the device is incubated to allow the cells to adhere to the substrate. After incubation the unattached cells can be washed away resulting in an aligned sheet of cardiomyocytes (Figure 6.7).

Topological Alignment

It has been observed that three-dimensional surface topology of culture substrates significantly affects in vitro cardiomyocytes orientation and attachment [70, 71, 74, 75]. Cells tend to spontaneously align to grooves (with dimensions in range of in vivo dimensions of the cells, e.g. 10-50 micron) in PDMS surface [71, 75]. The micro-topography provides anisotropic or directional growth for cells; and the cells tend to exhibit a more in-vivo like cellular morphology compared to lithographic methods. Figure 6.8, shows the anisotropic alignment of cardiomyocytes on the grooved part of a

membrane as opposed to the isotropic alignment in the flat part. The micro-patterns in the substrate are usually made by replica molding of PDMS against a master mold.

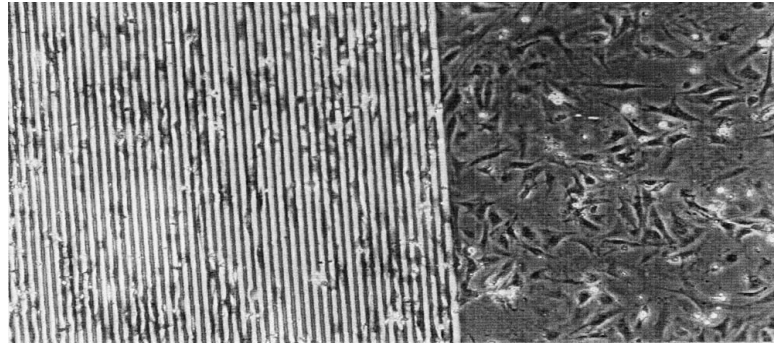


Figure 6.8 - Cardiac myocytes cultured on textured microchannels and untextured silicone [71]

Preferred cell alignment method for Stretchable MEA application

In the work from [1], our project refer to, topological alignment method for the stretchable MEA application has been chosen. Main reasons are the following: first of all it provides better cell attachment to the substrate during mechanical stretch and stimulation. Lithographic methods for cell alignment which use a protein for adhesion promotion are suitable for static settings they are not suitable for applications involving intense mechanical strain; there are significant problems with protein detachment from the silicone substrate due to mechanical strain despite prior surface treatment to adjust surface properties [1]. Secondly, applying and patterning the adhesive protein on the substrate is a cumbersome task which should be done manually or by specially designed robots; it requires careful adjustment of the surface contact angle of the stamps and substrate by oxygen plasma or UV ozone treatment which is generally not available on site where biological testing is performed [73, 75, 77], and also the whole procedure is very difficult to be integrated into a clean room compatible and batch processable fabrication process. However, forming different kinds of micro-patterns in an elastomeric substrate like PDMS for cell alignment are possible with conventional clean room processes.

6.1.2 ADVANTAGES OF STRETCHABILITY

Important evidences about the biocompatibility of the devices achieved with our technique and advantages we can obtain using a stretchable substrate in place of a rigid one, come from analysis performed by Leiden University Medical Centre, partner of Philips Research.

Figure 6.9 and Figure 6.10 compare cardiomyocytes, derived from human embryonic stem cells, deposited on PDMS and glass substrate respectively. PDMS substrate comes

from a device manufactured at Philips Research with an approach similar to the one we adopted, but with interconnects (see the wave meanders in the picture) in place of stiff islands. The glass substrate comes from the Petri-dish, traditionally used by biologists to culture cells. Fluorescence images have been collected from both substrates seven days after the cell cultures have been deposited. This kind of images allow us to study the biological environment: different cell structures show different colors under UV light. In the pictures here reported, we can identify two main elements: the DNA, in blue, and the α -Actinin, in green. DNA helps us to identify the nucleus; on the other hand α -Actinin provides us evidences about the position and the shape of Myofibrils, base units for muscular contraction. α -Actinin is a functional protein, necessary for the attachment of the actin filaments to the Z-lines in skeletal muscle cells, and to the dense bodies in smooth muscle cells (in our case). Cardiomyocytes grown on top of PDMS layer show characteristics more similar to in-vivo cardiomyocytes than cells grown on top of a glass plate. In fact PDMS-grown myofibrils show a more bordered and defined structure, closer to the one of mature cardiomyocytes.

Hence, these analysis proved not only the biocompatibility of the PDMS-based device, showing that cells survives and do not detach from the substrate, as we can still observe 7 days after they have been positioned. In fact, these experiments also show that a stretchable structure can create a better condition for cell growth, achieving a more mature state than stiff substrates. These observations confirm the intuition that cells “prefer” a substrate characterized by mechanical properties, such as Young modulus, similar to cells’ physiological environment. Of course cardiomyocytes cannot freely contract on a stiff substrate; conversely PDMS allow them to behave in a more physiological condition. The results collected from these analyses represent an important starting point for future development of this device for drug screening application. Notwithstanding the aforementioned limits and the questions still to be answered, this kind of device can strongly offer a cheap and meaningful integration to current technologies involved in drug screening application. In the next paragraph we present traditional applications of stretchable electronics that lie in the field of implantable devices. The state of art of these approaches provides further demonstration of the importance stretchable electronics is achieving in the biomedical sphere.

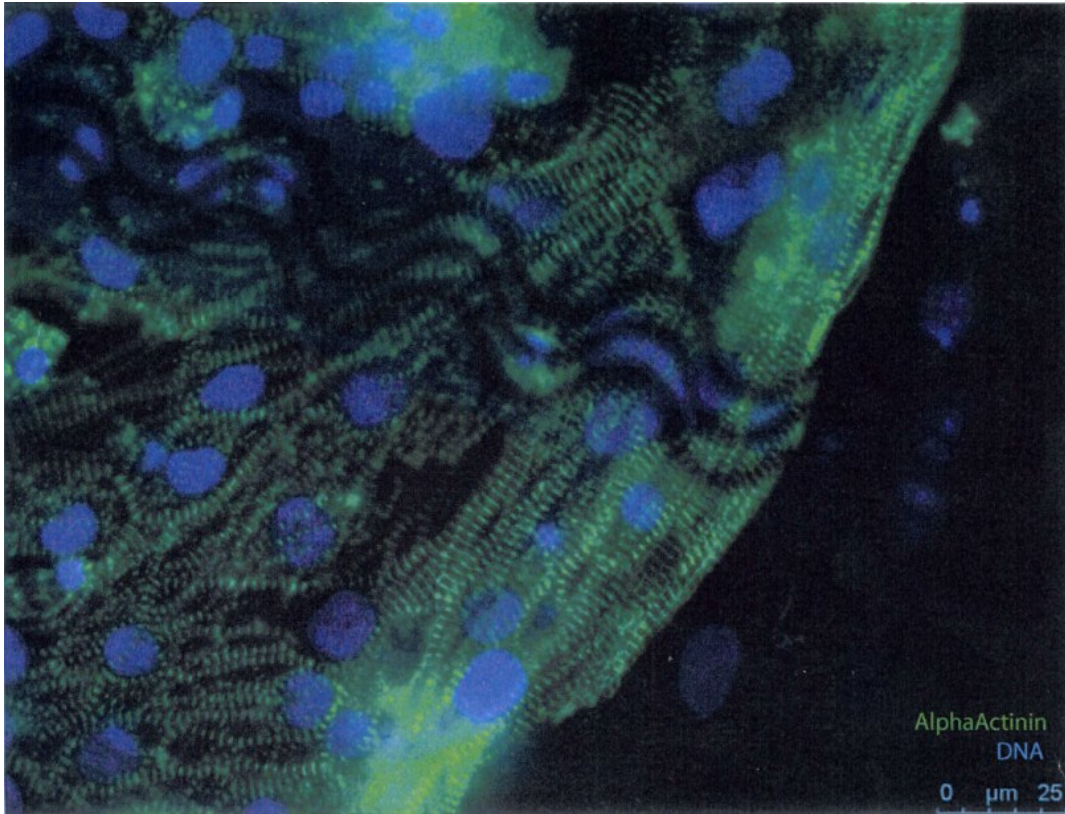


Figure 6.9 -Fluorescence image of hESC-derived cardiomyocytes grown on PDMS substrate. Courtesy of Leiden University Medical Centre

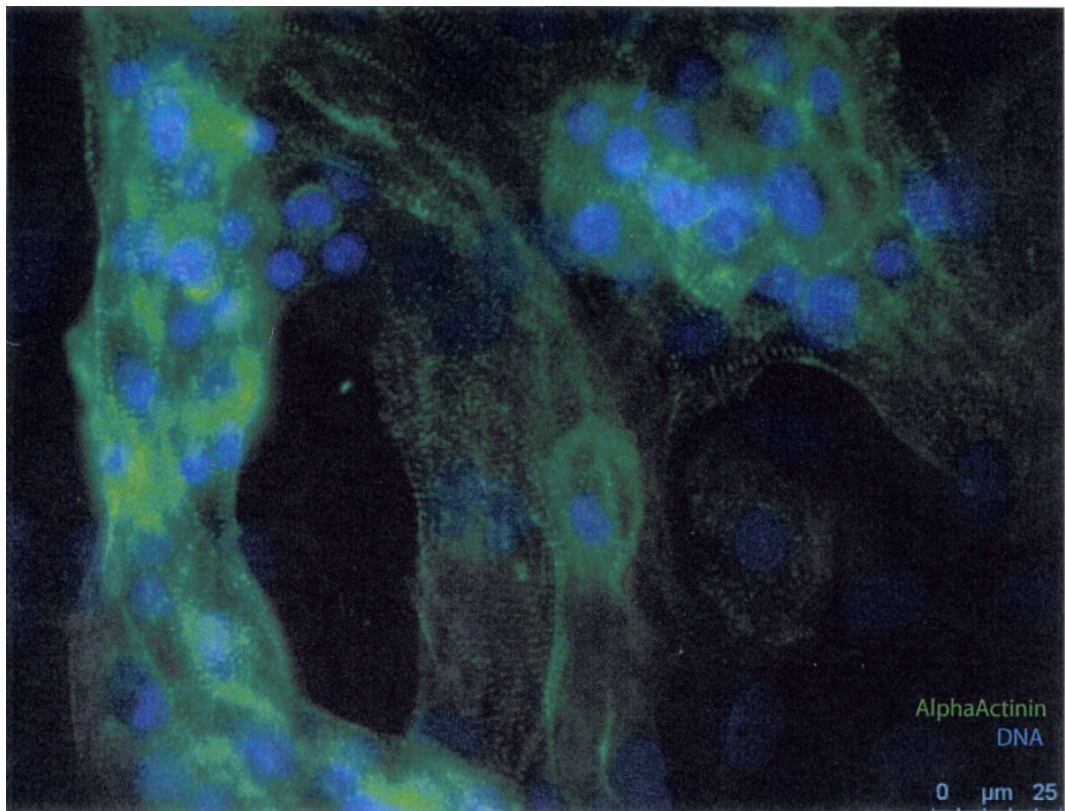


Figure 6.10 - Fluorescence image of hESC-derived cardiomyocytes grown on petri-dish (GLASS substrate). Courtesy of Leiden University Medical Centre

6.2 IMPLANTABLE DEVICES

Of the many potential areas of application in biomedical field, implantable neuroprosthesis can be considered one of the most representative [19]. Neural prostheses are a series of device that can substitute or integrate a motor, sensory or cognitive modality that might have been damaged as a result of an injury or disease. We can look at neuroprosthesis by a double point of view. Functional neuroprosthesis are about allowing an impaired subject to again perform a function. Rehabilitative neuroprosthesis are literally about a device that re-habilitates a function, mostly a motor one, that is artificially substituted; this last approach can be performed when the lesion has not completely compromised the target neural pathways.

A common component of all these systems is the need to interact directly with the nerves. The system must either collect signals from nerves or generate signals on nerves, or both [19]. Important requirements these devices need to match are biocompatibility, durability, reliability and low power dissipation in order to protect the surrounding biological tissues. Stretchable electronics can provide further improvements to these techniques; PDMS, a core technology inside this sphere, shows proven biocompatibility, furthermore mechanical properties of this elastomer are closer to biological tissue compared to traditional stiff material, still largely used for these purposes. In the next paragraphs we discuss the main neuroprosthesis devices highlighting the contribution stretchable electronics can provide them.

Cochlear implants

The principal cause of hearing loss is damage to or complete destruction of the sensory hair cells. Unfortunately, the hair cells are vulnerable structures and are subject to a wide variety of insults, including but not limited to genetic defects, infectious diseases (e.g., rubella and meningitis), overexposure to loud sounds, certain drugs (e.g., kanamycin, streptomycin, and cisplatin), and aging. In the deaf or deafened cochlea, the hair cells are largely or completely absent, severing the connections (both afferent and efferent) between the peripheral and central auditory systems. The function of a cochlear prosthesis is to bypass the missing or damaged hair cells by stimulating directly the surviving neurons in the auditory nerve, in order to reinstate afferent input to the central system [78].

The essential components in a cochlear prosthesis system are illustrated in Figure 6.11 and include: a microphone for sensing sound in the environment; a speech processor to transform the microphone output into a set of stimuli for an implanted array of

electrodes; a transcutaneous link for the transmission of power and stimulus information across the skin; an implanted receiver/stimulator both to decode the information received from the radio-frequency signal produced by an external transmitting coil and to generate stimuli using the instructions obtained from the decoded information; a multi-wire cable to connect the outputs of the receiver/stimulator to the individual electrodes; and finally the electrode array.

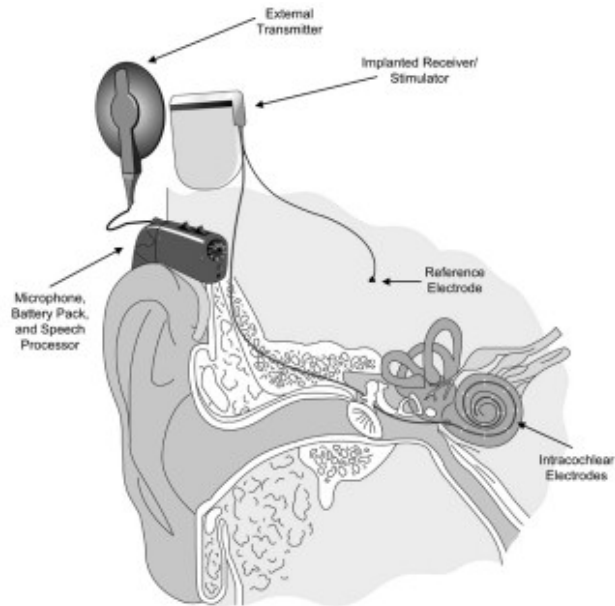


Figure 6.11 - Components of a cochlear implant system. Courtesy of MED-EL Medical Electronics GmbH, Innsbruck, Austria [78]

These components must work together as a system and a weakness in a component can degrade performance significantly. Stretchable electronics can provide important improvements in this instrumentation, especially to the electrode array component. Realizing this device with stretchable material can allow this electrode to follow the changes in the cochlea due to the child's growth. Therefore this device can be introduced during the first phases of the growth, with no need of other surgeries in future. Furthermore, intervening in earlier phases of growth can help, avoiding to compromise the development of sensory abilities of the subject involved.

Retinal prosthesis

Retinal prostheses represent the best near-term hope for individuals with incurable, blinding diseases of the outer retina. On the basis of the electrical activation of nerves, prototype retinal prosthesis have been tested in blind humans and have demonstrated the capability to elicit the sensation of light and to give test subjects the ability to detect motion [79]. A retinal prosthesis will restore the sense of vision through electrical activation of nerve cells by a device implanted on the retinal surface (Figure 6.12). A retinal prosthesis must perform several basis functions to replace the sense of vision. First, it must detect light emanated from sources or reflected from sources in the physical environment of the implant patient. The light must be transduced to an artificial stimulus.

Implementation of a stable electrode-retina interface will have a number of challenges. Many of these challenges stem from the fact that the retina is spherical and

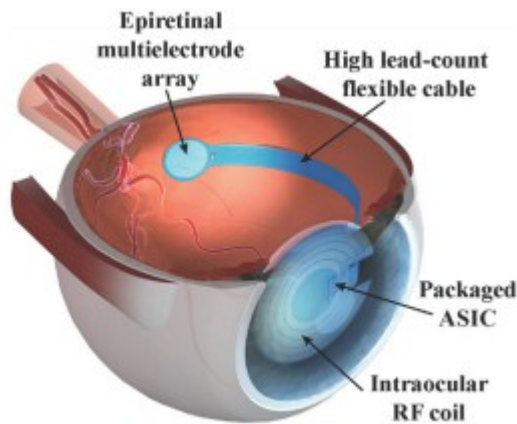


Figure 6.12 - Placements and components of envisioned next-generation intraocular retinal prosthesis [80]

microelectrode technology typically produces planar structures. Even if a spherical structure can be produced, the eye curvature is not consistent, and even a discrepancy of 200 μm can be significant. If the curvature mismatch causes a device to mechanically pressure the retina, then the retina can be damaged. Therefore, the ideal retinal stimulating electrode would have the flexibility to match the curvature of the retina without placing significant mechanical pressure on the retina [79].

The substrate material for a retinal stimulating electrode array must be both mechanically compliant, to take the shape of the retina, and resistant to water penetration. As we previously discussed, a common approach to flexible electrodes is to use a polymers substrate with a conductor patterned between two layers of insulating polymer. Polyamide has been plagued by problems related to water penetration and delaminating at the metal Polyamide surface. More recently PDMS has been proposed as a substrate and insulator for flex electrodes, but is not as good of a water barrier as Polyamide. This technological limit can be successfully overcome with Parylene. This material has been the one chosen by [80] for his artificial retinal study, also because Parylene's transparency, low water permeability and high flexibility. Chronically implantable retinal electrode arrays comprising 1024, 75 μm diameter electrodes arranged in a complex biomimetic pattern that closely mimics the density of ganglion cells in the human retina were fabricated by [80] according to a dual-layer process, with 60 electrodes connected via two traces each to facilitate electrical conductivity verification (Figure 6.14 and Figure 6.13). This research

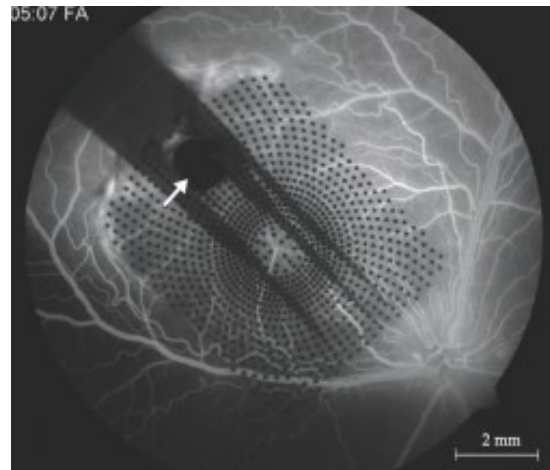


Figure 6.13 - Parylene MEAs tacked to the right canine retina showing normal vessel perfusion under the arrays. Arrows point to the retinal tack [80]

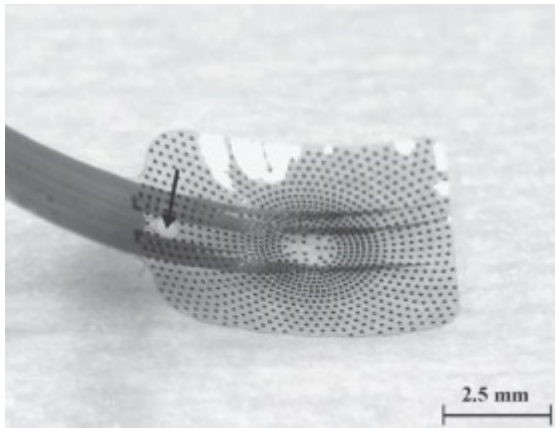


Figure 6.14 - Heat molded and annealed retinal electrode array with retained spherical curvature (arrow denotes retinal tack hole) [80]

represents an important step in order to achieve a complete functional device. Several problems still need to be addressed, such as the increase in the dimension of the device and the possibility to get higher resolution. Moreover, the involvement of private companies in parallel with academic research, a phenomenon that is gradually taking place, is a necessary step to producing a rigorously

manufactured and tested medical device.

Deep brain stimulation probes

Deep brain stimulation (DBS) has provided dramatic clinical benefit for people with essential tremor and Parkinson disease. Placement of high frequency stimulating electrodes in the region of the ventral intermediate nucleus of the thalamus can markedly reduce tremor in these conditions, and stimulation of either the subthalamic nucleus or the internal segment of the globus pallidus may not only reduce tremor, but also decrease bradykinesia, rigidity, and gait impairment, which plague people with Parkinson disease [81]. Furthermore, many have touted the potential benefit of DBS of selected brain regions for other movement disorders such as dystonia or Tourette syndrome, as well as a variety of disorders such as pain, depression, and obsessive compulsive disorder. Despite these realized and potential advances in treatment, controversy swirls around a number of clinically relevant and basic mechanistic issues, i.e. a better understanding of the mechanisms of action of DBS and the effects of DBS on the function of brain circuits. The subthalamic nucleus has become the most commonly used target for DBS in the treatment of PD (Figure 6.15). The STN is an important node in basal ganglia circuits, serving as a major target for cortical afferents and also receiving multiple inputs from other basal ganglia components. The output from the STN is glutamatergic and excitatory to both segments of the globus, to the substantia nigra pars reticulata and to the pedunculopontine area. It appears that there are at least two types of neuron in the STN as defined by baseline firing pattern and morphology. Thus, the DBS in the STN has the potential to influence a variety of afferent and efferent targets and may have different effects on different neurons.

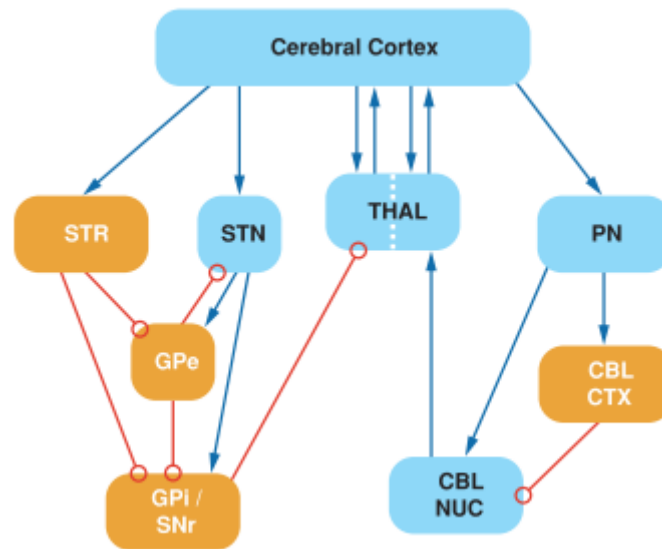


Figure 6.15 - Simplified schematic of subcortical motor system circuitry. Blue arrows represent excitatory synapses, and open red circles represent inhibitory synapses. Dotted line across the thalamus indicates the segregation between striatal and cerebellar connections. CBL CTX, cerebellar cortex; CBL NUC, cerebellar nuclei; GPe, globus pallidus external segment; GPI, globus pallidus internal segment; PN, pontine nuclei; STN, subthalamic nucleus; STR, striatum; THAL, thalamus [81]

Notwithstanding many questions still need to be addressed, live improvements of the involved patients are important evidences to be considered. Stretchable electrodes respectful of the brain soft nature can represent a step forward, making this technology more compliant to human needs.

7. CONCLUSIONS

Several observations about the project outcome are made and the principal ways further developments can follow are listed to let this work give the foundations for a future complete working device.

The aim of this thesis was to develop a fabrication process able to integrate stiff islands inside an elastomeric substrate and test the behavior of the overall structure once stressed. This can represent a starting point to achieve a stretchable multi-electrode array that can serve many biomedical applications, such as drug testing on cardiomyocytes or implantable devices, as previously discussed.

Two materials have been investigated with the aim of representing the stiff component embedded in the elastomeric layer: Silicon Nitride and Poly-silicon. No substantial difference between the two materials, used to make stiff islands, has been observed. Further analysis can better address which of the two materials is more suitable to represent the stiff component. Studying the properties of both the materials, we noticed Silicon Nitride is stiffer than Poly-silicon. Performing a similar study, Lacour targeted stiffer materials as the ones more reliable representing mechanical behavior of future electronic components [3]. Whenever, during future experiments, a discrepancy in the results will take place between Silicon Nitride and Poly-silicon, we should be oriented to consider the behavior of the first material more reliable than the second one in describing the circuitry properties.

Referring to the fabrication process, we started adjusting a strategy developed by [1] to integrate metal interconnects in a stretchable substrate. This approach was adapted in order to let us integrate stiff islands in PDMS. Results were encouraging, however they required some improvements. The most critical point was represented by wrinkles and cracks generated by Thermal Oxide etch stop layer, able to affect and compromise the islands themselves. Several investigations showed the principal reason of this phenomenon lied in the high compressive stress taking place in Thermal Oxide once grown upon Silicon. Once Silicon is removed, the oxide is no more prevented to release this stress, and it starts to bend and crack, according to its thickness. We replaced it with PECVD Oxide, re-arranging our fabrication process. This material is supposed to reduce the compressive stress inside the etch stop layer. Results showed an important step forward has been made; almost no more wrinkles and cracks took place in the final device we realized. The solution we adopted was not the only one to be possible. Another approach can involve Aluminum as etch stop layer in place of Oxide. Aluminum is supposed to have a tensile stress, opposite to the compressive one of Thermal Oxide. This will probably lead to an extremely flat etch stop layer after Silicon removal. Fabrication sequence can be reshaped accordingly and future works can address which etch stop layer behaves better between Aluminum and PECVD Oxide. Finally, we shaped the fabrication process in order to introduce the anti-delamination channels around the

islands. These techniques provided important improvements in the under-stress behavior of our devices.

In order to perform inflation test on the devices we developed and fabricated an instrumentation set up that let us achieve important evidence about the behavior of our structure. The results previously reported showed the behavior of a PDMS membrane with stiff islands embedded inside the elastomer. These results analyzed the thickness of the substrate and the shape of the islands. The thickness affects the strain in the PDMS during the inflation; lower strains in PDMS are obtained when thicker layer is stressed. Also the mechanical behavior of PDMS is influenced by its thickness, as observed by Liu in his strain/stress relation previously reported. The shape of the islands revealed interesting outcomes. Notwithstanding the higher peak strain in the membrane, square islands offer a strain distribution that implies a lower delamination from the surrounding substrate, as confirmed by FEM simulations from [19]. However the anti-delamination structure we developed, creating empty channels around the islands revealed useful in reducing this phenomenon. Two aspects about this technological improvement need to be considered. In order to obtain these empty spaces in the membrane we patterned the resist before spin-coating PDMS. When the device was ready we finally dissolved the resist in Acetone. Because of its organic nature, PDMS swells in Acetone, increasing its volume. This feature didn't compromise the islands, as observed. However, when also interconnections are going to be placed in the device, they risk to be affected by this volume increase of the substrate, resulting in a strain that can represent a possible source of rupture, even though no pressure is applied yet. Photo-patternable PDMS can help avoiding this problem; this kind of polymer can be patterned directly without requiring Acetone treatment. These indentations around the islands can become a problem also when interconnects need to cross these regions in order to reach the islands. In these zones they will remain no more embedded in PDMS; once inflated, the resulting stress can generate higher strain, able to lead these interconnections to collapse. The channels around the islands can then be interrupted in the regions where interconnects have to come through, letting these interconnections pass still embedded in PDMS. FEM simulations can be performed giving us suggestions about how to adapt this technology, optimizing the solution in case interconnects need to be placed. No fatigue test was carried out by applying prolonged cyclic inflation and deflation. The fatigue test can be done when also interconnections are fabricated to enable automatic monitoring of the platform resistance during the test and can provide further evidence about the durability of the device.

Important steps towards a finite and complete-working device have been made. Integration of the current appliance with interconnections and fabrication of simple circuitry on top of the islands can lead to breakthrough technology in the field of stretchable electronics as well as for its applications, including the biomedical ones.

REFERENCES

1. S. Khoshfetrat Pakazad, A.M.S., A. van de Stolpe, S. Braam, B. van Meer, R. Dekker, *A stretchable Micro-Electrode Array for In Vitro Electrophysiology*, in *IEEE 24th International Conference*. 2011. p. 829-832.
2. John A. Rogers, T.S., Yonggana Huang, *Materials and Mechanics for Stretchable Electronics*. Science, 2010. **327**.
3. Stephanie P. Lacour, S.W., Roger J. Narayan, Teng Li, Zhigang Suo, *Stiff subcircuit islands of diamond like carbon for stretchable electronics*. Journal of applied physics, 2006. **100**.
4. Dae-Hyeong Kim, J.-H.A., Won Mook Choi, Hoon-sk Kim, Tae-ho Kim, Jizhou Song, Yonggana Y. Huang, Zhuangjian Liu, Chun Lu, John A. Rogers, *Stretchable and Foldable Silicon Integrated Circuits*. Science, 2008. **320**.
5. D.-H. Kim, J.X., J. Song, Y. Huang and J. A. Rogers, *Stretchable, Curvilinear Electronics Based On Inorganic Materials*. Advanced Materials, 2010. **22**: p. 2108-2124.
6. Sekitani T, Z.U., Klauk H, Someya T., *Flexible organic transistors and circuits with extreme bending stability*. Nat. Mater., 2010. **12**: p. 1015-22.
7. Dahl-Young Khang, H.J., Young Huang, John A. Rogers, *A stretchable Form of Single-Crystal Silicon for High-Performance Electronics on Rubber Substrates*. Science, 2006. **311**.
8. Tsuyoshi Sekitani, Y.N., Kenji Hata, Takanori Fukushima, Takuzo Aida and Takao Someya, *A Rubberlike Stretchable Active Matrix Using Elastic Conductors*. Science, 2008. **321**: p. 1468-1472.
9. Stephanie P. Lacour, Z.H., Zhigang Suo, Sigurd Wagner, *Deformable interconnects for conformal integrated circuits*. Material Research Society, 2003. **736**.
10. Stephanie P. Lacour, D.C., Sigurd Wagner, Teng Li, Zhigang Suo, *Mechanisms of reversible stretchability of thin metal films on elastomeric substrates*. Applied Physics Letters, 2006. **88**.
11. Samuel Rosset, M.N., Philippe Dubois, Herber R. Sea, *Metal Ion Implantation for the Fabrication of Stretchable Electrodes on Elastomers*. Adv. Funct. Mater., 2009. **19**: p. 470-478.
12. Stephanie P. Lacour, J.J., Sigurd Wagner, Teng Li, Zhigang Suo, *Stretchable Interconnects for Elastic Electronic Surfaces*. Proceeding of the IEEE, 2005. **93**.

13. Ke Wang, M.v.D., Nico Kooyman, Michel M. J. Decre', *Toward Circuit Integration on Fully Flexible Parylene Substrates*, in *31st Annual International Conference of the IEEE EMBS*. 2009: Minneapolis, Minnesota, Usa. p. 5866-5869.
14. Yong Xu, Y.-C.T., Huang, A, Chih-Ming Ho, *IC-integrated flexible shear-stress sensor skin*. *Microelectromechanical Systems, Journal of applied physics*, 2003. **12**: p. 740-747.
15. Mario Gonzalez, F.A., Mathieu Vanden Bulcke, Dominique Brosteaux, Bart Vandeveldel, Jan Vanfleteren, *Design of Metal Interconnects for Stretchable Electronic Circuits using Finite Element Analysis*. *Microelectronics Reliability*, 2008. **48**.
16. Hans Verstraete, S.P., Ronald Dekker, *Design of stress-deflecting objects and shapes for metal interconnects in stretchable electronic circuits using finite element analysis*. 2010, Technische Universiteit Delft: Delft, The Netherlands.
17. Ingrid M. Graz, S.P.L., *Complementary organic thin film transistor circuits fabricated directly on silicone substrates*. *Organic Electronics*, 2010. **11**: p. 1815-1820.
18. Fischer, T., *Material Science for Engineering Students*. Elsevier, 2009.
19. Romeo, A., *Substrate transfer technology for stretchable electronics: a feasibility study*. 2011, Politecnico di Milano.
20. Maghrib, M., *Microfabrication of an Implantable silicone Microelectrode array for an epiretinal prosthesis*. Lawrence Livermore National Lab., 2003.
21. *Parylene -product information sheet*. Specialty Coating Systems, 2009.
22. T. Stieglitz, H.B., M. Schuettler, and J.U. Meyer, *Micromachined, polyimide/based devices for flexible neural interfaces*. *Biomedical Microdevices*, 2000. **2**: p. 283-294.
23. Dhara, K.C.G.a.D., *Polymers for Biomedical Applications*. American Chemical Society, 2008.
24. K.W. Meacham, R.J.G., L. Guo, S. Hochman, and S.P. DeWeerth, *A lithographically-patterned, elastic multi-electrode array for surface stimulation of the spinal cord*. *Biomedical microdevices*, 2008. **10**: p. 256-269.
25. Dew-Hugues, O.W.a., *Metals, ceramics and polymers*. Cambridge university press, 1974.
26. M.A. Unger, H.-P.C., T. Thorsen, A. Scherer, and S.R. Quake, *Science*, 2000. **288**: p. 113-116.
27. Whitesides, J.C.M.a.G.M., *Accounts of Chemical Research*, 2002. **35**: p. 491-499.

28. Whitesides, Y.X.a.G.M., *Angewandte Chemie International Edition*, 1998. **37**: p. 550-575.
29. S.A. Visser, R.W.H., and S.L. Cooper, *Polymers. Biomaterials Science*. Academic Press, 1996: p. 50-60.
30. Alvaro Mata, A.J.F., Shuvo Roy, *Characterization of Polydimethylsiloxane (PDMS) Properties for Biomedical Micro/Nanosystem*. *Biomedical Microdevices*, 2005. **7**: p. 281-293.
31. Florian Schneider, J.D., Robert Kamberger, Ulrike Wallrabe, *Process and material properties of polydimethylsiloxane (PDMS) for Optical MEMS*. *Sensors and Actuators A*, 2009. **151**: p. 95-99.
32. Miao Liu, J.S., Ying Sun, Christopher Bock, Quanfang Chen, *Thickness-dependent mechanical properties of polydimethylsiloxane membranes*. *J. Micromech. Microeng.*, 2009. **19**.
33. *Information about Dow Corning brand Silicone Encapsulants*, D. CORNING, Editor. p. Data Sheet.
34. David T. Eddington, W.C.C., David J. Beebe, *Development of process protocols to fine tune Polydimethylsiloxane material properties*, in *7th international conference on miniaturized chemical and biochemical analysis systems*. 2003: Squaw Valley, California USA. p. 1089-1092.
35. F Schneider, T.F., J Wilde, U Wallrabe, *Mechanical properties of silicones for MEMS*. *J. Micromech. Microeng.*, 2008. **18**.
36. J C Lotters, W.O., P H Veltink, P Bergveld, *The mechanical properties of the rubber elastic polymer polydimethylsiloxane for sensor application*. *J. Micromech. Microeng.*, 1997. **7**: p. 145-147.
37. C, G., *Gerthsen Physik*. Springer, 2003. **22**.
38. Tabata, O., et al., *Mechanical property measurements of thin films using load-deflection of composite rectangular membranes*. *Sensors and Actuators*, 1989. **20**(1-2): p. 135-141.
39. Nanshu Lu, X.W., Zhigang Suo and Joost Vlassak, *Failure by simultaneous grain growth, strain localization, and interface debonding in metal films on polymer substrates*. *Journal of Materials Research*, 2009. **24**: p. 379-385.
40. Li, T., et al., *Delocalizing strain in a thin metal film on a polymer substrate*. *Mechanics of Materials*, 2005. **37**(2-3): p. 261-273.

41. Nanshu Lu, X.W., Zhigang Suo, and Joost Vlassak, *Metal films on polymer substrates stretched beyond 50%*. Applied Physics Letters, 2007. **91**(221909).
42. EerNisse, E.P., *Stress in thermal SiO₂ during growth*. Applied Physics Letters, 1979. **35**(1): p. 8-10.
43. Xin Zhang, K.-S.C., S. Mark Spearing, *Thermo-mechanical behavior of thick PECVD oxide films for power MEMS applications*. Sensors and Actuators A, 2003. **103**: p. 263-270.
44. P. J. French, P.M.S., R. Mallee, E. J. M. Fakkeldij, R. F. Wolffenbuttel, *Optimization of a low-stress silicon nitride process for surface-micromachining applications*. Sensors and Actuators A, 1997. **58**: p. 149-157.
45. *Silicon Nitride, Material Properties*. Available from: <http://accuratus.com/silinit.html>.
46. Deniz Armani, C.L., Narayan Aluru, *Re-configurable fluid circuits by PDMS elastomer micromachining*, in *IEEE international MEMS 1999 conference. Twelfth IEEE International Conference on Micro Electro Mechanical Systems*. 1999. p. 222-227.
47. William N. Sharpe, B.Y., Ranji Vaidyanathan, *Measurements of Young's modulus, poisson's ratio, and tensile strenght of polysilicon*, in *Micro Electro Mechanical Systems, 1997. MEMS '97, Proceedings, IEEE., Tenth Annual International Workshop*. 1997: Nagoya, Japan. p. 424-429.
48. Danielle M. Tanner, J.A.W., Karen Helgesen, Lloyd W. Irwin, Frederick Brown, Norman F. Smith, Natan Masters, *MEMS reliability in shock environments*, in *IEEE International Reliability Physics Symposium*. 2000: San Jose', CA. p. 129-138.
49. W. Menz, J.M., O. Paul, *Microsystem Technology*. 2001: WILEY-VCH.
50. O. Geschke, H.K., P. Tellerman, *Microsystem Engineering of Lab-on-a-chip Devices*. 2008: WILEY-VCH.
51. Madou, M.J., *Fudamentals of Microfabrication - The science of Miniaturization*. Second Edition ed. 2002: CRC PRESS.
52. Nguyen, N.-T., *Fundamentals and Application of Microfluidics*. 2nd ed. 2006: Artech House.
53. Shaikh, S., *Reactive Ion Etching Process Development and Characterization*. 2004: NNIN REU Research Accomplishments.
54. O. C. Zienkiewicz, R.L.T., J. Z. Zhu, *The Finite Element Method. Its basis & fundamentals*. 6th ed. 2005: Elsevier.
55. Ned Bowden, A.T., Jeff Carbeck, George M. Whitesides, *Self-Assembly of Mesoscale Objects into Ordered Two-Dimensional Arrays*. Science, 1997. **276**.

56. *HPR 500 - Safer Solvent, Positive Resist Series*, OCG Microelectronic Materials.
57. *Triton X-100 Product Information*. Sigma-Aldrich.
58. Braam, S.R. and C.L. Mummery, *Human stem cell models for predictive cardiac safety pharmacology*. Stem Cell Research, 2010. **4**(3): p. 155-156.
59. Tolstosheeva, E., *Development of stretchable metallic interconnects for a drug screening device powered by cardiomyocytes*. 2009, Technical University of Hamburg: Hamburg.
60. Smith, D.H., *Commentary: concerns with the suspension of Adderall XR*. The Canadian child and adolescent psychiatry review, 2005. **14**.
61. Davis, R.P., et al., *Pluripotent stem cell models of cardiac disease and their implication for drug discovery and development*. Trends in Molecular Medicine, 2011. **17**(9): p. 475-484.
62. Icilio Cavero, G.-X.Y., Robert Lux, Uwe Steinhoff, *Safety pharmacology and prolongation of the QT interval*. Journal of Electrocardiology, 2007. **40**: p. 58-61.
63. Braam, S.R., *Human embryonic stem cells: Advancing biology and cardiogenesis toward functional approach*. PHD Report, LUMC, The Netherlands, 2010.
64. Oren Caspi, I.I., Izhak Kehat, Amire Gepstein, Gil Arbel, Irit Huber, Jonathan Satin, Lior Gepstein, *In Vitro Electrophysiological Drug Testing Using Human Embryonic Stem Cell Derived Cardiomyocytes*. Stem cells and development, 2009. **18**.
65. Viskin, S., *Torsades de Pointes*. Current treatment options in cardiovascular medicine, 1999: p. 187-195.
66. Moore, J.C., et al., *Human embryonic stem cells: Genetic manipulation on the way to cardiac cell therapies*. Reproductive Toxicology, 2005. **20**(3): p. 377-391.
67. Braam, S.R., et al., *Prediction of drug-induced cardiotoxicity using human embryonic stem cell-derived cardiomyocytes*. Stem Cell Research, 2010. **4**(2): p. 107-116.
68. Michael Reppel, P.I., Ulrich Egert, Frieder Juchelka, Jurgen Hescheler, Irina Drobinskaya, *Effect of cardioactive drugs on action potential generation and propagation in embryonic stem cell-derived cardiomyocytes*. Cell Physiol Biochem, 2006. **19**: p. 213-224.
69. Kujala, V.J., et al., *Averaging in vitro cardiac field potential recordings obtained with microelectrode arrays*. Computer methods and programs in biomedicine, 2011. **104**(2): p. 199-205.

70. Bo-Yi Yu, P.-H.C., Yi-Ming Sun, Yu-Tsang Lee, *Topological micropatterned membrane and its effect on the morphology and growth of human mesenchymal stem cells*. Journal of membrane science, 2006. **271**: p. 31-37.
71. Desai, T.A., *Micro and nano scale structures for tissue engineering constructs*. Medical engineering & physics, 2000. **22**: p. 595-606.
72. G. M. Whitesides, O., S. Takayama, X. Jiang, D.E. Ingberg, *Soft lithography in biology and biochemistry*. Annual review of biomedical engineering, 2001. **3**: p. 335-373.
73. George K. Toworfe, R.J.C., C. S. Adams, I. M. Shapiro, *Fibronectin absorption on surface-activated polydimethylsiloxane and its effect on cellular function*. Journal of biomechanical materials part A, 2004. **71**(3): p. 449-461.
74. Marina Flaibani, L.B., Elisa Cimetta, Martina Piccoli, Paolo De Coppi, Nicola Elvassore, *Muscle differentiation and myotubes alignment is influenced by micropatterned surfaces and exogenous electrical stimulation*. Tissue engineering part A, 2009. **15**(9): p. 2447-2457.
75. Meer, B.v., *Aligning cardiomyocytes using batch processable techniques*. Internship report, TU Delft, 2010.
76. Boker, N.T., *Prototyping of a stretchable microelectrode array for cardiotoxicity drug screening*. 2009, TU Delft: Delft, The Netherlands.
77. Tan, J.L., *Simple approach to micropattern cells on common culture substrate by tuning substrate wettability*. Tissue engineering part A, 2004. **10**(5/6): p. 865-872.
78. Blake S. Wilson, M.F.D., *Cochlear implants: a remarkable past and a brilliant future*. Hearing Research, 2008. **242**: p. 3-21.
79. James D. Weiland, W.L., Mark S. Humayun, *Retinal Prostheses*. Annu. Rev. Biomed. Eng., 2005. **7**: p. 361-401.
80. Damien C. Rodger, A.J.F., Wen Li, Hossein Ameri, Ashish K. Ahuja, Christian Gutierrez, Igor Lavrov, Hui Zhong, Parvathy R. Menon, Ellis Meng, Joel W. Burdick, Roland R. Roy, V. Reggie Edgerton, James D. Weiland, Mark S. Humayun, Yu-Chong Tai, *Flexible parylene-based multielectrode array technology for high density neural stimulation and recording*. Sensors and Actuators B, 2008. **132**: p. 449-460.
81. Joel S. Perlmuter, J.W.M., *Deep Brain Stimulation*. Annu. Rev. Neurosci., 2006. **29**: p. 229-257.

APPENDIX A – DETAILED FABRICATION SEQUENCE

A) PATTERNING THE WAFER TOPSIDE

1. Cintillio cleaning (HZplus30min and FZplusHCLrecipes)
2. Deposition of 2 μm of zero-stress PECVD Oxide on the wafer topside at 400°C in Novellus
3. Deposition of 200 nm of Poly-Silicon or LPCVD Silicon Nitride (low-stress)
4. Cintillio cleaning (HZplus30min and FZplusHCLrecipes)
5. Rinse in DI water to restore the OH- group on wafer surface before priming
6. Spin coat HPR504 photo resist: 4000 rpm with TMSDEA primer on the ACS track
7. Expose Giuliano_NIT2 mask hard contact, 50 μm gap, 7 seconds
8. Develop HPR504 on ACS track
9. Rinse in DI water to remove the remnants of developer from the backside
10. 200 nm Nitride/Poly-Silicon etch from the topside using PECVD Oxide as etch stop layer
11. Resist strip in oxygen plasma barrel 1000 W, 130°C, 60'

B) PATTERNING THE OXIDE MASK ON THE BACK SIDE FOR THROUGH WAFER ETCHING

12. Cintillio cleaning (HZplus30min and FZplusHCLrecipes)
13. Deposit 3 μm of PECVD Oxide on the wafer topside at 300°C-400°C in Novellus
14. Spin coat HPR504 photo resist: 1000 rpm with TMSDEA primer on the ACS track
15. Expose Giuliano_BCC mask hard contact, 50 μm gap, 18 seconds
16. Develop HPR504 on ACS track
17. Rinse in DI water to remove the remnants of developer from the topside

18. For Nitride wafer: dry etch Oxide and Nitride from the backside stopping at the Silicon layer
For Poly-Silicon wafer: dry etch Oxide from the backside stopping at the Poly-Silicon layer
19. Resist strip in oxygen plasma barrel 1000 W, 130°C, 60'

C) FABRICATING THE RESIST MOLD

20. Cintillio cleaning (HZplus30min and FZplusHCL recipes)
21. Rinse in DI water to restore the OH- group on wafer surface
22. Spin coat AZ4533 photo resist: 1000 rpm with TMSDEA primer on the ACS track
23. Expose Giuliano_Shield mask hard contact, 50 μm gap, 16 seconds
24. Develop AZ4533 on ACS track (thick-recipe)

D) SPIN-COATING PDMS ON THE FRONT SIDE

25. Descum in the oxygen plasma barrel: 25°C, 600W, 2', to improve PDMS adhesion
26. Prepare PDMS mixture (10:1 base:curing-agent)
Spin coat PDMS on front side ($\sim 20 \mu\text{m}$)
500 rpm, 15", close-lid
3000 rpm, 60", close-lid
27. Oven bake at 90°C, 30'

E) ANTI-STICTION ALUMINUM DEPOSITION AND THROUGH WAFER ETCHING

28. Sputter deposit 50nm of Al on front side: 125 W, 122"
29. Through-wafer etch from the backside stopping at the PECVD Oxide on STS-ASE: 190'

F) RELEASING THE PDMS MEMBRANE

30. Strip the anti-stiction Al in PES at 30°C, 2'
31. Dip in Isopropanol and then in water to wet through wafer holes
32. Remove etch-stop oxide in BOE with surfactant (to wet the through wafer holes): 20'
33. Dissolve the resist mold in acetone bath, 3'